5-2013

Computational Fluid Dynamics Validation of Buoyant Turbulent Flow Heat Transfer

Jared M. Iverson
Utah State University

COMPUTATIONAL FLUID DYNAMICS VALIDATION OF BUOYANT TURBULENT FLOW HEAT TRANSFER

by

Jared M. Iverson

A thesis submitted in partial fulfillment
of the requirements for the degree

of

MASTER OF SCIENCE

in

Mechanical Engineering

Approved:

Dr. Robert E. Spall Major Professor	Dr. Aaron Katz Committee Member
Dr. Warren F. Phillips Committee Member	Dr. Mark R. McLellan Vice President for Research and Dean of the School of Graduate Studies

UTAH STATE UNIVERSITY
Logan, Utah

2013

Abstract

Computational Fluid Dynamics Validation of Buoyant Turbulent Flow Heat Transfer

by

Jared M. Iverson, Master of Science

Utah State University, 2013

Major Professor: Dr. Robert E. Spall
Department: Mechanical and Aerospace Engineering

Computational fluid dynamics (CFD) is commonly implemented in industry to perform fluid-flow and heat-transfer analysis and design. Turbulence model studies in literature show that fluid flows influenced by buoyancy still pose a significant challenge to modeling. The Experimental Fluid Dynamics Laboratory at Utah State University constructed a rotatable buoyancy wind tunnel to perform particle image velocimetry experiments for the validation of CFD turbulence models pertaining to buoyant heat-transfer flows. This study validated RANS turbulence models implemented within the general purpose CFD software STAR-CCM+, including the $k-\varepsilon$ models: realizable two-layer, standard two-layer, standard low-Re, v^2-f, the $k-\omega$ models from Wilcox and Menter, and the Reynolds stress transport and Spalart–Allmaras models. The turbulence models were validated against experimental heat flux and velocity data in mixed and forced convection flows at mixed convection ratios in the range of $0.1 \leq Gr/Re^2 \leq 0.8$. The $k-\varepsilon$ standard low-Re turbulence model was found most capable overall of predicting the fluid velocity and heat flux of the mixed convection flows, while mixed results were obtained for forced convection.

(172 pages)

Public Abstract

Computational Fluid Dynamics Validation of Buoyant Turbulent Flow Heat Transfer

by

Jared M. Iverson, Master of Science

Utah State University, 2013

Major Professor: Dr. Robert E. Spall
Department: Mechanical and Aerospace Engineering

Computational fluid dynamics (CFD) is commonly used to visualize and understand complicated fluid flow and heat transfer in many industries. It is imperative to validate the CFD computer models in order to avoid costly design choices where experimentation cannot be used to ratify the predictions of computer models. Assessments of CFD computer models in the literature conclude that significant errors occur in computer model predictions of fluid flow influenced by buoyancy forces.

The Experimental Fluid Dynamics Laboratory at Utah State University constructed a wind tunnel with which to perform experiments on buoyancy induced fluid flow. The experiments measured the heat transfer and fluid velocity occurring in the buoyant flows to be used to validate computer models. Additional experimental measurements at the inlet and around the walls from each experiment allowed the computer models to simulate the fluid flow with realistic boundary conditions.

For this study, four experiments were performed, including two cases where the buoyancy influence was significant, and two where it was not. For each set of two cases, one experiment was performed where the heat transfer occurred from a wall of the wind tunnel held at constant temperature and in the other experiment the wall temperature fluctuated axially.

This study used the experimental data to validate computer models available in the general purpose CFD software STAR-CCM+, including the $k-\varepsilon$ models: realizable two-layer, standard two-layer, standard low-Re, v^2-f, the $k-\omega$ models from Wilcox and Menter, and the Reynolds stress transport and Spalart–Allmaras models. The $k-\varepsilon$ standard low-Re model was found most capable overall of predicting the fluid flow and heat transfer that occurred in the flows where the buoyancy influence was significant. For the experimental cases where the buoyancy influence was less significant, the validation results were inconsistent.

To my wife, Kim, for her enduring support and love...

Acknowledgments

My wife, Kim, first and foremost, deserves my thanks for continually supporting me and pushing me accross the finish line. Though she did not always understand what I was talking about, she was an unwavering support to me. Her patience and understanding have made this possible.

I would like to thank Dr. Spall for opening the door of opportunity for me to be a part of this research. I have drawn much from his wisdom and experience, particularly concerning computational fluid dynamics. He deserves my respect and gratitude for being an exceptional professor and mentor to me throughout my studies here at Utah State University.

I would also like to thank my other committee members, Dr. Katz and Dr. Phillips. I'm grateful for the help they gave me when I was stuck at crossroads and didn't know which way to turn.

This research is being performed using funding received from the DOE Office of Nuclear Energy's Nuclear Energy University Programs.

Jared M. Iverson

Contents

List of Tables

List of Figures

Notation

General

B	bias uncertainty
$\left\lvert\frac{CI}{\bar{y}_e}\right\rvert_{avg}$	average relative confidence indicator
$\left\lvert\frac{CI}{\bar{y}_e}\right\rvert_{max}$	maximum relative confidence indicator
C_μ	parameter in constitutive equation of eddy viscosity models
e_a	approximate relative error of the finest mesh
e_{ext}	extrapolated relative error of ϕ^p_{ext}
E	true CFD model error
$\tilde{E}$	estimated CFD model error
$\frac{\tilde{E}}{\bar{y}_e}$	relative error
$\left\lvert\frac{\tilde{E}}{\bar{y}_e}\right\rvert_{avg}$	average relative error
$\left\lvert\frac{\tilde{E}}{\bar{y}_e}\right\rvert_{max}$	maximum relative error
f	elliptic relation parameter
$f(x_i)$	interpolated function value at x_i for spline computations
$f"(x_i)$	interpolated second derivative value at x_i for spline computations
g	acceleration due to gravity
GCI_{fine}	fine-grid convergence index, estimated discretization error
Gr	Grashof number, $Gr = g\beta(T_s - T_\infty)x^3/\nu^2$
Gr/Re^2	mixed convection ratio
h_k	representative cell or grid size of the k^{th} grid refinement
H	distance between two points for hyperbolic clustering equations
k	turbulent kinetic energy
k^*	thermal conductivity
m	order of interpolating polynomial
n	number of experiments
N	total number of cells used to calculate h
p	apparent order of accuracy for the numerical method
p^*	pressure
Pr	Prandtl number, $Pr = \mu c_p/\lambda$
Pr_t	turbulent Prandtl number
r_{ij}	grid size ratio, $r_{ij} = h_i/h_j$
Re	Reynolds number, $Re = ux/\nu$

General Continued

s	standard deviation
S	strain rate tensor
t	thickness of the first wall boundary cell layer
t^*	students t-distribution probability
T_s	wall surface temperature
T_∞	freestream temperature
$u'v'$	turbulent shear stress
u, v, w	velocity components in x, y and z directions
U	total uncertainty
U_b	bulk velocity at the inlet
U_τ	wall friction velocity, $U_\tau = \sqrt{\tau_s/\rho}$
v^2	variance of the normal component of turbulent velocity
x	axial distance from the test section inlet
y	normal distance from the test section heated wall
y_e	experimentally measured validation parameter
y_m	CFD solution of y_e
$\bar{y}_e$	experiment sample mean
y^+	non-dimensional distance from heated wall, $y^+ = yu_\tau/\nu$
z	transverse distance from the heated wall centerline

Greek Symbols

α	level of confidence for confidence intervals, given by $100 \cdot (1 - \alpha)\%$
β	thermal expansion coefficient
ε	turbulent dissipation rate
ε_{ij}	difference in ϕ between the i and j grid refinement levels
ζ	hyperbolic clustering parameter
η	non-dimensional location between 0 and H for hyperbolic clustering
θ	cell skewness angle
μ	dynamic viscosity
μ_t	turbulent viscosity
μ^*	true experimental mean
ν	kinematic viscosity, $\nu = \mu/\rho$
ν^*	degrees of freedom for student's t-distribution
$\tilde{\nu}$	modified turbulent diffusivity
ρ	density
σ	hyperbolic clustering placement parameter
τ_s	wall shear stress
ϕ_k	CFD solution of a specific variable from the k^{th} grid refinement level
ϕ^p_{ext}	ϕ value extrapolated to $h = 0$
ω	specific dissipation rate

Acronyms

ASME	American Society of Mechanical Engineers
CFD	Computational Fluid Dynamics
DES	Detached Eddy Simulation
EFDL	Experimental Fluid Dynamics Laboratory
GCI	Grid Convergence Index
HFS	Heat Flux Sensor
LES	Large Eddy Simulation
MCS	Maximum Cell Size
PIV	Particle Image Velocimetry
R2L	Realizable Two-Layer
RANS	Reynolds-Averaged Navier–Stokes
RST	Reynolds Stress Transport
RoBuT	Rotatable Buoyancy Wind Tunnel
S2L	Standard Two-Layer
SA	Spalart–Allmaras
SGR	Surface Growth Rate
SLR	Standard Low-Re
SRQ	System Response Quantity
SST	Shear Stress Transport

Chapter 1

Introduction

Computational fluid dynamics or CFD is a numerical method to analyze and predict fluid flow. The mathematical equations used in CFD are based on scientific results throughout the history. Foremost among all the scientific contributions to the CFD numerical method are the Navier–Stokes equations, formulated by Claude Louis Marie Henry Navier and George Gabriel Stokes. The Navier–Stokes equations provide a basis for all CFD calculations by giving expressions for the conservation of mass, momentum and species [1,2]. The mathematical expressions are non-linear with regard to many fluid properties and flows; therefore, solutions to the Navier-Stokes equations are predominantly obtained via numerical solver, exceptions being flow situations in which many critical simplifications may be applied. At the advent of the Navier–Stokes equations, solutions were obtained analytically by making assumptions about the fluid flow in order to simplify the equations. Later, empirical models obtained from theory or experimental data were solved on discrete meshes in order to approximate the Navier–Stokes equations [2]. Many of the models are still in use today and continue to be improved through further experimental validation. This study seeks to validate CFD turbulence models by comparing simulated and experimentally measured heat flux and fluid velocity in order to assess the feasibility of using CFD as a method of analysis in buoyant heat transfer flows.

Chapter 1 contains a literature review of research completed with regard to CFD modeling, including its current state-of-art and its connection to this study. Chapter 2 describes the experimental setup and the experiments carried out by the Experimental Fluid Dynamics Laboratory for this study, including instrumentation and uncertainty. Chapter 3 provides details of the discretized meshes generated for the study and the simulation setup, including physics models used, boundary conditions, initial conditions and convergence cri-

teria. Chapter 4 describes the mean-comparison-validation method implemented in this study. Chapter 5 contains results from the completed CFD simulations and validation assessment, including local profiles of the heat flux and boundary layer velocity, calculated modeling error and demonstrated grid convergence. Chapter 6 provides concluding remarks drawn from the validation and simulation results.

1.1 Literature Background

Turbulent fluid flow modeling, irrespective of heat transfer complexities, is a daunting task. In turbulent flow, as the Reynolds number (Re) increases eddies of varying size and strength begin to form, particularly in flow regions adjacent to boundary walls or opposing fluid. And to computationally capture the effect of every eddy in a flow using the Reynolds-averaged Navier–Stokes equations would require a prohibitively large amount of information [2]. Therefore, models of turbulent flow are either based on a time average, which calculates a solution from the mean flow neglecting the instantaneous fluctuations, or empirical relations obtained from experimentation. The turbulence models that have been produced have been validated against many experimental data sets and continue to be revised and improved.

So *et al.* [3] added a damping function to the $k-\varepsilon$ model in order to accurately predict free and wall bounded shear flows. It was found that the added damping function gave solutions with good correlation to experimental and direct numerical simulation data for all of the cases observed. Furthermore, Sarkar and So [4] performed a critical evaluation of near-wall two-equation models in which ten different models, including $k-\tau$, $k-\omega$ and $k-\varepsilon$, were assessed against experimental and direct numerical simulation data for plane Couette, channel, and flat-plate boundary-layer flows. The flows observed were chosen because the spatial distribution of the turbulent kinetic energy predicted by two-equation models has been incorrect. The study showed that models that are asymptotically consistent can predict the distribution of the turbulent kinetic energy.

The significance of predicting turbulent fluid flow accurately is compounded by the addition of heat transfer because it causes an interdependence of the temperature and ve-

locity fields through buoyancy. Therefore, it is recommended that the energy solver order of accuracy be less than or equal to that of the momentum solver [5] because the temperature solution can only be as accurate as that of the velocity. However, if the buoyancy terms in the governing momentum equations are neglected then the velocity field can be calculated without regard to the temperature and the two can be solved independently. This modeling simplification was utilized by many of the early turbulence models to avoid the interdependence of the governing equations.

In addition to the interdependence created by buoyancy, the heat transfer in the flow occurs primarily in the boundary layer, depending on Re and Prandtl (Pr) numbers [6]. This restriction focuses heat transfer modeling on the near-wall fluid flow. Many methods are available to solve the near-wall flow, but the most prevalent are wall functions and low-Reynolds number methods. Wall functions are empirically derived relations for the flow adjacent to the wall, consisting of the viscous sub-layer and fully turbulent regions. Conversely, low-Reynolds number methods integrate the k and ε equations to the wall [7]. Both methods have been shown to be reliable approaches to solving wall bounded flows.

Kader and Yaglom [8] explored the wall function method by obtaining function parameters from experimental data and then comparing the model against the data. Good correlation of the Nusselt number (Nu)was observed for turbulent heat-transfer flows in pipes, channels, and boundary layers. Kader performed another study on "Temperature and Concentration Profiles in Fully Turbulent Boundary Layers" [9]. This additional study bolstered the findings of the first, in that good correlation was again observed between predicted and experimental temperature distributions. However, despite the positive results of these wall function studies, the function parameters obtained may only be compatible for the specific cases studied. This concern seems ratified by "The Numerical Computation of Turbulent Flow" study of Launder and Spalding [10] whose intent was to find a universal solver capable of providing credible solutions to a large variety of flow types. The wall function method was merited for its ability to economize computer time and storage as well as to introduce empirical information to the solution in specific cases. Nevertheless, turbu-

lent flow studies peformed by Launder and Spalding showed that the two-equation $k-\varepsilon$ model coupled with the low-Re near-wall method provided a better universal applicability and realism than the wall-function method. Additional studies show that good heat-transfer correlations can also be found using Spalart–Allmaras, $k-\omega$, and Reynolds-stress-transport models [11, 12].

The discrepancies in the above mentioned heat-transfer correlation studies may be due to neglecting the effects of buoyancy. Buoyancy affects fluid flow in several critical ways, including: modification of the shear distribution, interaction with the turbulence generating mechanisms, anisotropic effects on the velocity fluctuations, laminarization, counter-gradient fluxes, and the formation of gravity waves [5, 13–18]. Petukhov and Polyakov [19] summarize the effects of buoyancy as the structural and external effects, referring to the direct influence of buoyancy on the turbulence field and on the mean field, respectively. For horizontal flows only the structural effect is present, evidenced by the vertical stratification of the flow. In contrast, both the structural and external effects are present in a vertical flow. Because the two effects commonly act in opposing directions, turbulent buoyancy flows are governed by a complicated interaction of the effects.

An early buoyant heat-transfer study by Malhotra and Hauptmann [13] recognized impaired heat-transfer predictions because of the complicated buoyancy effects. The impairment was attributed to the modified shear distribution and turbulence generating mechanisms. Later, recognizing the known buoyant flow effects, Sommer and So [20] modified a Reynolds-stress model to be asymptotically consistent in the near-wall region, to relax the constant turbulent Prandtl number (Pr_t) assumption, and to account for counter-gradient transport. In heated horizontal and vertical flows, the modified model presented solutions in agreement with experimental data. This promising result for buoyant heat transfer flow modeling is distorted however by findings of recent turbulence model studies. Spall *et al.* [21] studied variable property flows in strongly heated vertical pipes and found the v^2-f model capable of predicting wall temperatures within engineering accuracy. Also, contrary to expectations from the findings of Thomas *et al.* [12], the $k-\omega$ model significantly over pre-

dicted heat transfer rates for the range of Re tested. He *et al.* [22] assessed the performance of a diverse group of turbulence models in predicting supercritical pressure heat transfer in vertical flows. Consistent with the findings of Spall *et al.*, the assessment found that the $v^2 - f$ model gave the best results. Conversely, an earlier turbulence model assessment for mixed convection flows by Kim *et al.* [23] found that early $k - \varepsilon$ models predict the effects of buoyancy best; although, the canceling of inaccurate expressions in the models was the reason for their superior performance. The disagreement between the results of these studies implies that the complicated interaction of the structural and external buoyancy effects remains a serious challenge to buoyant turbulent flow modeling.

Petukhov [24] concluded that in order to make progress in modeling buoyant turbulent flow heat transfer further experimentation of stratified flows was required. Areas of concern consisting of velocity and temperature fields, turbulent stresses, turbulent heat fluxes, and correlation functions. Launder [15] further concluded that development of accurate stress models must precede those for buoyant heat transfer; on the basis that turbulent stresses are an important input to the heat flux equations, both directly and through their influence on the mean velocity field. The turbulence models currently available have accounted for many of these concerns; however, study results show that turbulence recovery is lacking [23], viscous corrections are required in order to be accurate [25], and that no models reproduce the buoyancy turbulence production of kinetic energy accurately [22].

Recognizing the turbulence model limitations regarding buoyant flows, this validation study seeks to contribute insight into the use of CFD to predict heat transfer in turbulent fluid flow where buoyancy is significant. Special interest will be given to specifying which turbulence model provides the most accurate predictions of heat transfer, because studies in the literature give conflicting conclusions [22, 23].

Chapter 2

Experimental Setup

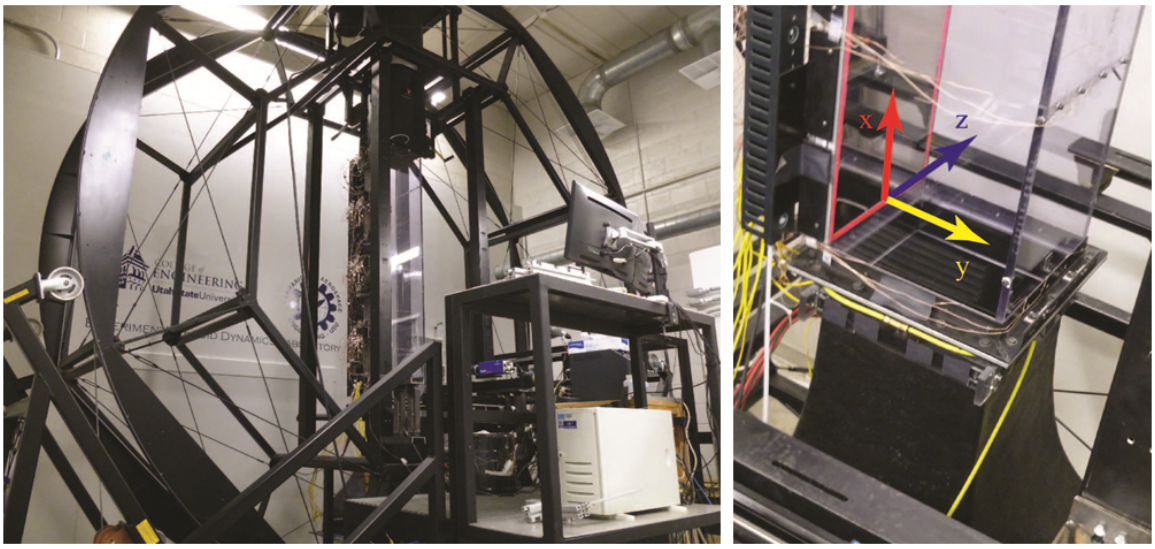

Fig. 2.1: Rotatable Buoyancy Wind Tunnel (RoBuT)

Utah State Universitys Experimental Fluid Dynamics Laboratory (EFDL) contracted Engineering Laboratory Design, Inc. to construct the Rotatable Buoyancy Wind Tunnel (RoBuT) to perform benchmark CFD validation experiments of buoyant flows. The wind tunnel is built into a rotational frame to enable both buoyancy-aided and buoyancy-opposed mixed/forced convection experiments using the same inlet in all cases. The RoBuT is shown in Fig. 2.1 and includes a sub-figure of the tunnel inlet showing the global coordinate system used in this study. A schematic of the RoBuT layout is shown in Fig. 2.2 with the air flow indicated in green.

The test section of the RpBuT is a square 30.5×30.5 *cm* cross-section that is 192.3 *cm* long. The test section includes three clear polycarbonate (Lexan) walls and a composite nickel-coated aluminum plate embedded with heaters, hereafter referred to as the heated

plate or wall; all four of the walls are embedded with instrumentation.

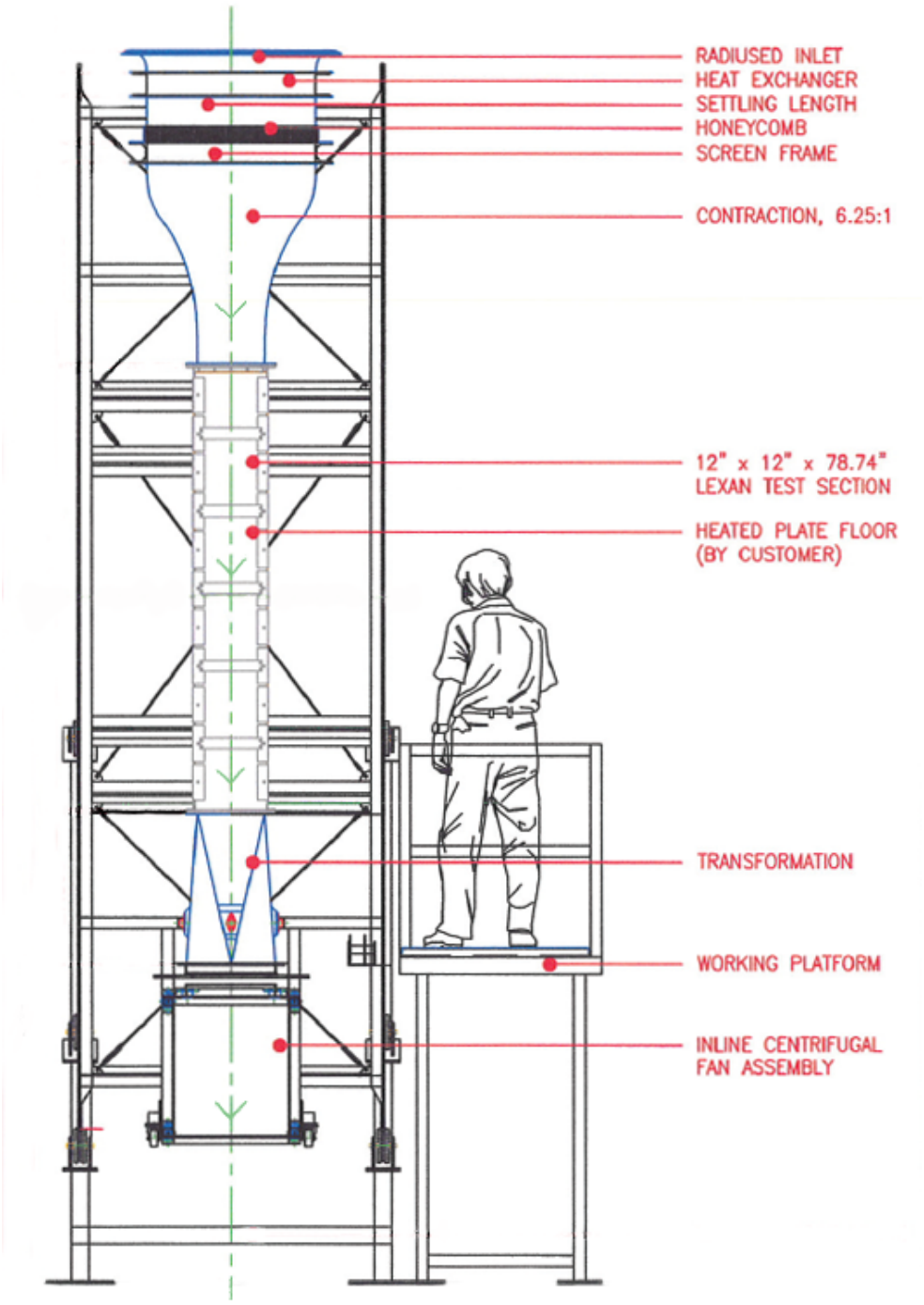

Fig. 2.2: Schematic of the RoBuT. The dashed green line indicates the direction of air flow through the wind tunnel. Used with permission from Engineering Laboratory Design, Inc.

The embedded instrumentation includes that required for temperature measurements of the inlet flow and the test section walls as well as heat flux measurements at three locations along the centerline of the heated wall: $x = 16, 77$ and $139\ cm$ hereafter referred to as the first, second and third HFS respectively. The RoBuT is also instrumented to enable PIV evaluation of the flow velocity at the inlet plane and across the near-wall flow region. Collectively, the data obtained from the instrumentation fully defines the CFD simulation boundary conditions, specifying the energy and momentum introduced into the system, and the system response quantities (SRQ) of interest at the three HFS locations for the turbulence model validations.

In addition to the RoBuT instrumentation, the EFDL researchers obtained six cross-sectional measurements of the RoBuT test section at seven axial locations in order to reconstruct the test section geometry for the CFD simulations. As shown in Fig. 2.3, the measurements include the height at the center, left and right walls and the width at the middle, bottom and top walls as viewed from the test section inlet were the heated wall is the bottom. For further details concerning the RoBuT experimental setup and instrumentation the reader is directed to reference [26] and [27].

2.1 Instrumentation Uncertainty

The following subsections give a brief description of the sensor and PIV instrumentation used in the RoBuT experiments and their respective uncertainties.

2.1.1 Thermocouples

The thermocouples used for the temperature measurements described above are type K and made by Omega Engineering. They were calibrated using an IsoTech Fast-Cal series temperature calibrator with an accuracy of 0.3 °C within a temperature range of $20-200$°C. The overall uncertainty of the temperature measurements is 1 °C, mainly due to the data acquisition system.

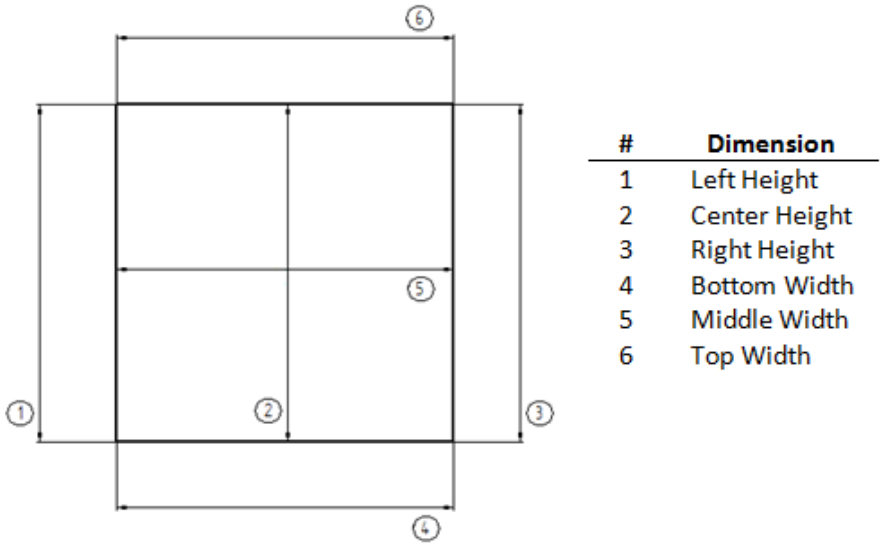

Fig. 2.3: Placement of cross-sectional as-built dimension measurements.

2.1.2 Heat Flux Sensors

The three thin film heat flux sensors are Model 20457-3 made by RDF Corporation. They were calibrated by the manufacturer and have an uncertainty of 2% of the reading (EFDL assumes this uncertainty to be at 95% confidence).

2.1.3 Particle Image Velocimetry System

The PIV system from LaVision, Inc. includes an Nd-YAG double pulse laser producing 532 nm wavelength light and a 12-bit CCD camera with 1376 X 1040 resolution and frame rate of 4 Hz. In conjunction with the system hardware, DaVis version 8.1.6 was used to process the images acquired with a multi-pass cross-correlation algorithm. The uncertainty of the PIV velocity measurements was assessed with respect to particle image diameter, particle shift, particle density, and fluid shear using an automatic uncertainty estimator for PIV developed at the EFDL [28]. Because the uncertainty calculation is dependent on the PIV algorithm used, a wide range of user inputs, flow characteristics and the experimental setup which vary in time and space, they lead to non-uniform uncertainty throughout the flow field. Recognizing this limitation the 95% uncertainty for the flows in this study varied

between 45% in the boundary layer and 0.5% in the freestream; in general, the uncertainty was less than 1%.

2.2 Validation Cases

This turbulence model validation study consists of four quasi-steady cases, including two cases from both the mixed and forced convection heat-transfer regimes. The RoBuT was designed exclusively for experiments with an isothermal temperature condition at the heated plate boundary. As will be illustrated later, an ideal isothermal boundary condition was not achieved across the heated plate of the RoBuT test section due to the limitations of the design and instrumentation; cases M1 and F1 represent mixed and forced convection flows over the non-ideal isothermal plate. During experimentation one of the heaters embedded in the heated plate failed, which lead to the thermal boundary conditions of the heated plate in the mixed and forced convection flows of cases M2 and F2.

The four validation cases included in this study were included for two reasons: first, validation of both mixed and forced convection cases enables the validation study to investigate whether a turbulence model gives consistent results in differing heat transfer regimes; and second, while maintaining flow speeds between the mixed and forced cases, the differing thermal state of the heated plate enables the turbulence models to be validated under thermal conditions of varying difficulty.

Mixed convection is a flow regime where both natural and forced convection contribute to the physics of the fluid flow and occurs when the mixed convection ratio, Gr/Re^2, satisfies $0.3 \leq Gr/Re^2 \leq 10$ [29]. The Grashof number is defined as $Gr = g\beta(T_s - T_\infty)x^3/\nu^2$, where g is the acceleration of gravity, β is the fluid thermal coefficient of expansion, T_s and T_∞ are the surface and freestream fluid temperatures respectively, and x is the axial distance from the leading edge of the RoBuT test section. The Reynolds number is defined as $Re = ux/\nu$, where u is the freestream fluid velocity.

For all four cases, the plate was stabilized at 150°C and the flow velocity was chosen to obtain desirable mixed convection ratios. For forced convection, the ratio was set to obtain $Gr/Re^2 = 0.03$ at the first HFS in order to facilitate negligible natural convection/buoyancy

influence from the heated wall, resulting in a nominal bulk velocity of $\sim 4.65\ m/s$. As shown in Table 2.1, the desired conditions were closely duplicated in the F1 and F2 experiments, resulting in ratios near 0.3 and the onset of mixed convection at the third HFS. For mixed convection, the flow speed was reduced to $\sim 2.5\ m/s$, while maintaining turbulence in the boundary layer this speed enabled mixed convection to occur at the second and third HFS locations. The Reynolds, Grashof, and mixed convection ratios achieved in each experiment at the three HFS locations are tabulated in Table 2.1.

Table 2.1: Reynolds, Grashof and mixed convection ratio for each validation case and HFS location. Note that Gr is not a function of the freestream velocity.

Case	Location	Re	Gr	Gr/Re^2
M1	HFS 1	21600	$3.67E{+}7$	0.079
	HFS 2	109000	$5.13E{+}9$	0.433
	HFS 3	201000	$2.99E{+}10$	0.736
M2	HFS 1	24600	$4.93E{+}7$	0.082
	HFS 2	112000	$5.61E{+}9$	0.448
	HFS 3	217000	$3.22E{+}10$	0.686
F1	HFS 1	36900	$3.32E{+}7$	0.024
	HFS 2	174000	$5.10E{+}9$	0.168
	HFS 3	314000	$2.99E{+}10$	0.302
F2	HFS 1	42300	$4.82E{+}7$	0.027
	HFS 2	183000	$4.11E{+}9$	0.123
	HFS 3	338000	$3.16E{+}10$	0.276

The SRQs used for validation of the CFD turbulence models in the described experiments are the heat flux and the streamwise fluid velocity across the near region at each of the three HFS locations. In each validation case, the CFD solution variables corresponding to the SRQ data are compared to evaluate the modeling error. Note that for the M2 and F2 cases the heat flux at the second HFS is not used for validation, because the failed heater allows conduction of heat in the plate across that region and therefore, measurements of

the heat flux are inaccurate.

All of the boundary conditions, SRQs, and experimental error data for the described validation cases were obtained from the EFDL researchers on the RoBuT project. The data are available to the public at http://efdl.neng.usu.edu/EFDL/EFDL_Home.html.

Chapter 3

CFD Setup

Using the general purpose CFD software STAR-CCM+[1], the previously described experiments were modeled in order to validate and assess the different turbulence models' ability to predict heat transfer in buoyant, turbulent flow. The approach to simulating the experiments consisted of: reconstruction of the RoBuT using as-built measurements into a discretized mesh domain, applying physics models to the simulation, placing appropriate boundary and initial conditions to reproduce the experimental environment, and ensuring iterative and grid convergence. Each validation case was simulated with eleven different turbulence models and solved over three consecutively coarser meshes to investigate grid convergence; the turbulence models included in the study represent a diverse variety of turbulence solver methods, including those indicated by the literature that may give the best results.

3.1 Meshing

In order to numerically solve the governing momentum, energy and turbulence equations for CFD simulations, it is necessary to discretized or partition a normally continuous region into distinct volumetric cells. All of the volumetric cells collectively make up the simulation's computational domain. In this study the computational domain represents the experimental flow field inside the experimental RoBuT test section. By solving the governing equations, the simulation will attempt to predict the fluid variables existent at each distinct volumetric cell in the domain, such as velocity, pressure, temperature, turbulent kinetic energy, etc., which will then be used to validate the turbulence models against the corresponding fluid properties measured experimentally. Because the fluid variables computed by each model simulation are directly dependent on the discretized mesh, the

[1]STAR-CCM+ version 8.04 is a widely verified CFD software package distributed by CD-ADAPCO

distribution and refinement of the discretized cells is fundamental to a simulation's ability to accurately predict the physics and fluid flow occurring within the computational domain.

Given the turbulent flow heat transfer physics occurring in the validation cases, specific attributes were imposed on the discretized cell distribution and refinement in order to promote accurate calculation of the physics. The following points outline the attributes imposed on the mesh cell distribution and detail the reason for their application:

Duplication of the as-built experimental RoBuT test section in the computational domain

A validation study seeks to determine the degree to which a given physics model accurately duplicates reality [30]. In order for a computer physics model to duplicate an experiment, the computational domain of the model must also duplicate the experimental boundaries. Therefore, to enable the duplication of the experimental RoBuT test section in the computational domain the RoBuT research group obtained measurements of the RpBuT test section after it was constructed. The measurements were obtained on seven cross-sectional planes along the test section with six dimension measurements per plane, see Fig. 2.3. The following figure shows the location of the seven measurement planes.

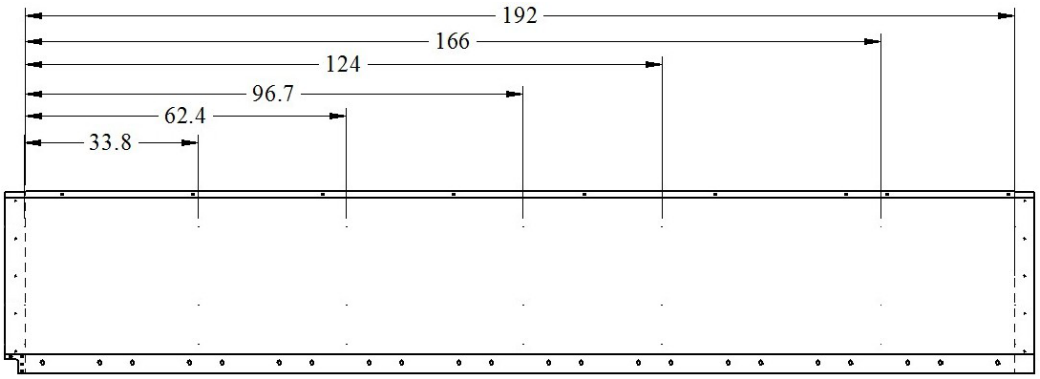

Fig. 3.1: As-built dimension measurement planes relative to the leading edge of the test section (dashed vertical line on left side). All of the measurements are in cm.

Refinement of the near-wall mesh to obtain $y^+ \approxeq 1$ in the cell layer adjacent to the wall boundaries

In the validation cases, the heat transfer between the heated plate and the turbulent air flow results in a complex interaction of the fluid flow, wall shear stress and variable fluid properties due to temperature dependencies. To capture the effects of heat transfer, the simulation discretized cell distribution in the near-wall region must be refined.

$$y^+ = \frac{yU_\tau}{\nu} = \frac{y\sqrt{\tau_s/\rho}}{\nu} \tag{3.1}$$

Because wall y^+ is dependent on the fluid viscosity (ν), density (ρ) and the wall shear stress (τ_s), fluid properties that indirectly account for the heat transfer through their temperature dependence, refining the mesh so that the first cell layer adjacent to the wall gives $y^+ \approxeq 1$ provides a cell distribution capable of capturing the heat transfer effects in the viscous sub-layer and fully turbulent region of the turbulent boundary layer. Additionally, this cell distribution is required by STAR-CCM+ in order for the governing turbulence model equations to be integrated to the wall rather than resorting to empirically derived wall functions.

Minimal cell skewness

The cell skewness angle is a measure designed to assess a specific cell's ability to permit diffusion without becoming unbounded [31]. Consider the two cells with a shared face shown in Fig. 3.2. The skewness angle (θ) is the angle between the face normal vector ($\mathbf{a}$) and the vector connecting the two cell centroids ($\mathbf{ds}$). An angle of zero indicates that the two cells are orthogonal to each other and thus calculations will not be impaired. Solver convergence is impaired if the cell skewness angle is greater than 90°; STAR-CCM+ recommends limiting the angle to $< 85°$.

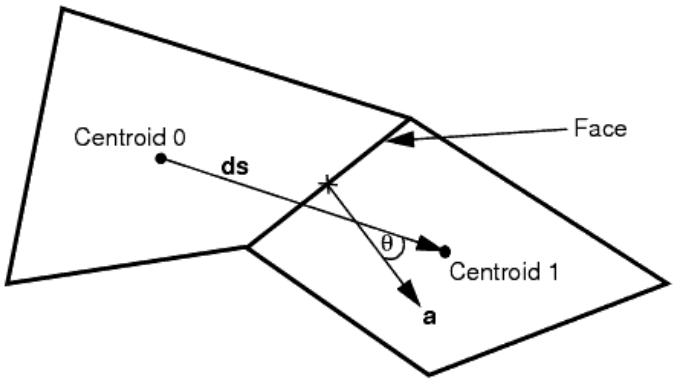

Fig. 3.2: Depiction of the cell skewness angle, θ

A FORTRAN code was written to generate a hyperbolically clustered hexahedral cell mesh from the as-built measurements. The hyperbolic clustering equations, discussed in Section 3.1.2, enabled the near-wall cell distribution refinement discussed above and the hexahedral cell type created inherently minimized the cell skewness angle as it partitioned the computational domain of the RoBuT test section. Furthermore, the hexahedral cell type lent itself to enhancing the numerical calculation of the flow throughout the test section, because the resulting flow generally aligned with the mesh discretization.

The following sections describe the assumptions made to utilize the as-built measurements in the creation of the computational domain and the methods implemented in the mesh generation code. The resulting discretized meshes used in the validation study are also visualized and the grid convergence index (GCI) method is explained.

3.1.1 As-Built Geometry

In order to validate the turbulence models against the experimental data from the RoBuT the simulation boundary conditions and geometry must duplicate those present in the wind tunnel. The boundary conditions are readily available from the RoBuT instrumentation. The simulation geometry however requires modeling of the RoBuT test section from the cross-sectional dimensions.

The cross-sectional, as-built dimensions were obtained at room temperature by meticulous placement of a micrometer into the test section and measuring the dimensions desired at the locations of interest. Despite the precise measurements obtained from the micrometer however, the measurements obtained do not have a point of reference, meaning that each measurement is independent and without any means to correlate its position and orientation with the other measurements taken. The lack of a reference point prohibits precise reconstruction or modeling of the test section. Therefore, in order to model the RoBuT test section geometry, assumptions were made about the geometry itself to allow its modeling from the as-built dimensions. Collaboration with the EFDL researchers led to the following seven assumptions which were used to model the simulation geometry:

1. The heated wall is perfectly flat, void of curvature
2. The centerline of the heated wall is straight
3. The center height dimension is measured along the centerline of the heated wall and is orthogonal to the wall
4. The midpoint of the middle and top width dimensions are aligned with the center height dimension
5. The midpoint of the middle width dimension coincides with the midpoint of the center height dimension
6. The middle width and center height dimensions are orthogonal
7. The left, right and top dimensions are from vertex to vertex

It is recognized that the simulation geometry will not exactly duplicate that of the experimental setup as desired because the cross-sectional dimensions lack a reference point and the heated wall cannot be perfectly flat, as assumed above. Furthermore, due to thermal expansion of the heated plate during while at operating temperature, $\sim 150°C$, it must also be recognized that the as-built measurements may not conform with the dimensions of

the RoBuT test section during operation. It is reasonable that unrealized thermal expansion effects, curvature or flaws in the simulation geometry will have an effect on pressure gradient calculations, convective accelerations or other flow properties in the CFD solution; however, the influence of these defects is assumed to be negligible relative to truncation and turbulence modeling errors.

3.1.2 Mesh Generation Code

Hyperbolic clustering is a grid generation method that distributes a specified number of points on a linear line between two predetermined points in space, as shown in Fig. 3.3. The point distribution is governed by a hyperbolic equation dependent on the predetermined extremum, containing parameters to control how clustered the points on the line are, ζ, and where they are clustered, σ. Two clustering distributions, one-sided and two-sided, were implemented in the mesh generation code written to read in the as-built dimensions and create the computational domain, defined as

$$x_i = H\frac{(\zeta+1)-(\zeta-1)[(\zeta+1)/(\zeta-1)]^{1-\eta_i}}{[(\zeta+1)/(\zeta-1)]^{1-\eta_i}+1} \tag{3.2}$$

$$x_i = H\frac{(2\sigma+\zeta)[(\zeta+1)/(\zeta-1)]^{(\eta_i-\sigma)/(1-\sigma)}+2\sigma-\zeta}{(2\sigma+1)\{1+[(\zeta+1)/(\zeta-1)]^{(\eta_i-\sigma)/(1-\sigma)}\}} \tag{3.3}$$

where H is the distance between the two extremum. η_i is a value between 0 and 1 corresponding to the location of x_i between 0 and H, recognizing that there is a uniform dη between 0 and 1 and dx is not uniform but varies hyperbolically.

Fig. 3.3: Hyperbolic clustering of points between two predetermined points

Eq. 3.2 provides the one-sided distributions shown in Fig. 3.4, it is specifically formulated to cluster the interior points near $y = 0$, thus the absence of σ in the equation. For the two-sided distributions shown in Fig. 3.5, σ in Eq. 3.3 is set to $1/2$ so that the interior points are equally clustered at the extremum. The clustering parameter, ζ, ranges from 1 to ∞ in both equations; as illustrated in Figs. 3.4 and 3.5, as ζ approaches 1 the point distribution becomes more finely clustered.

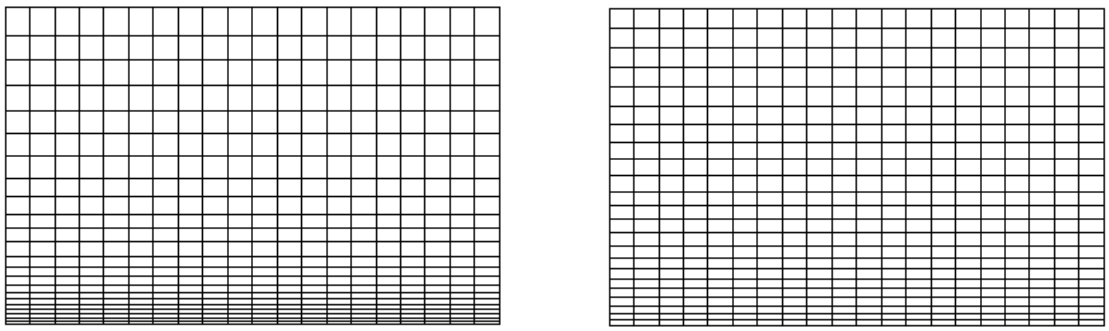

(a) $\zeta = 1.05$ (b) $\zeta = 1.2$

Fig. 3.4: Grid generated by the one-sided transformation function in Eq. 3.2.

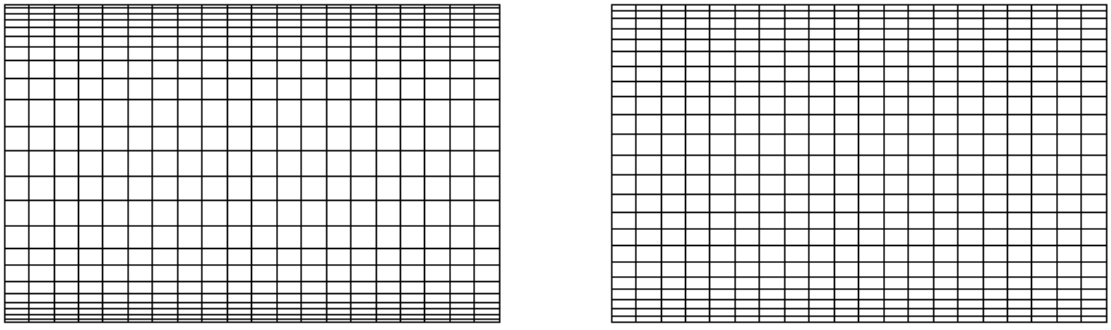

(a) $\zeta = 1.05$ (b) $\zeta = 1.2$

Fig. 3.5: Grid generated by the two-sided transformation function in Eq. 3.3.

One-sided clustering was implemented axially down the test section computational domain, along the X axis, to aid in resolving the fluid flow as it develops along the test section and two sided clustering was implemented along each of the test section walls, in

the Y and Z axis, in order to resolve the turbulent boundary layer flow. As shown in Fig. 2.1, the coordinate axis are defined with the Y-Z axes plane coincident with the test section inlet plane with the Y axis normal to the heated wall and the X axis is directed axially down the centerline of the heated wall; thus, the coordinate axes origin is located on the heated wall centerline at the intersection of the inlet and heated wall planes.

The extremum for the hyperbolic clustering equations were obtained from the test section boundaries, which were modeled using the assumptions discussed previously in conjunction with polynomial splines dependent on the as-built dimensions. The implemented spline methods were the cubic and Lagrange interpolating polynomial methods defined in *Numerical Methods for Engineers* [32]. Cubic splines were used to capture the axial variations in a given dimension at nine locations around the unheated walls of the test section and Lagrange polynomials were used to capture the variation between dimensions on a given as-built measurement plane.

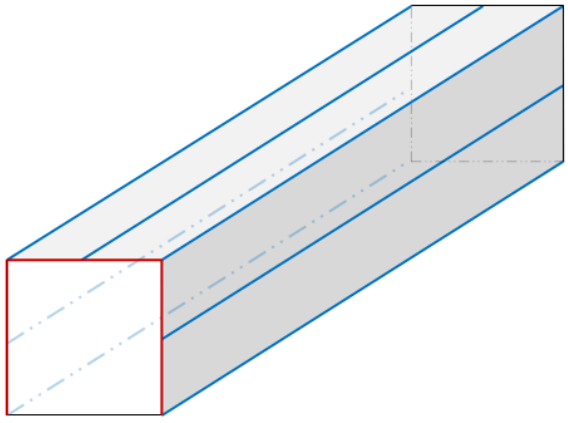

Fig. 3.6: Curves defined by spline methods. Cubic splines are shown in blue and Lagrange polynomials in red.

Fig. 3.6 illustrates the location of the nine cubic splines in the computational domain. Each of the splines is a piecewise continuous function consisting of six two-dimensional cubic polynomials, one for each interval of the test section outlined by the as-built measurement

planes. The cubic equation for each interval is of the form

$$\begin{aligned} f_i(x) = & \frac{f_i^{"}(x_{i-1})}{6(x_i - x_{i-1})}(x_i - x)^3 + \frac{f_i^{"}(x_i)}{6(x_i - x_{i-1})}(x - x_{i-1})^3 \\ & + [\frac{f(x_{i-1})}{x_i - x_{i-1}} - \frac{f^{"}(x_{i-1})(x_i - x_{i-1})}{6}](x_i - x) \\ & + [\frac{f(x_i)}{x_i - x_{i-1}} - \frac{f^{"}(x_i)(x_i - x_{i-1})}{6}](x - x_{i-1}) \end{aligned} \tag{3.4}$$

were the unknown second derivatives are solved with

$$\begin{aligned} & (x_i - x_{i-1})f^{"}(x_{i-1}) + 2(x_{i+1} - x_{i-1})f^{"}(x_i) + (x_{i+1} - x_i)f^{"}(x_{i+1}) \\ & = \frac{6}{(x_{i+1} - x_i)}[f(x_{i+1}) - f(x_i)] + \frac{6}{(x_i - x_{i-1})}[f(x_{i-1}) - f(x_i)]. \end{aligned} \tag{3.5}$$

Using the axial location of each measurement plane as the dependent variable and the as-built dimension value as the independent variable, Eq. 3.4 and 3.5 were evaluated to obtain the six polynomials for each cubic spline.

The above equations for this method were derived under the following constraints:

1. The function values are equal at the interior piecewise function transitions or knots
2. The first and last functions pass through the end points
3. The first derivatives at the interior knots are equal
4. The second derivatives at the interior knots are equal
5. The second derivatives at the end knots are zero

These constraints enable the resulting splines to include all of the as-built dimension data and have smooth second order continuous interval transitions, attributes desired in the duplication of the experimental RoBuT test section to the simulations computational domain.

Fig. 3.6 also illustrates the general curves in the computational domain computed with the Lagrange interpolating polynomial method; this method was chosen to compute

these curves because it produced a smooth arc from the 3 known points on each curve, see Fig. 2.3, rather than the cubic spline method which produced unrealistic sinusoidal curves. In addition to producing a smooth arc, the Lagrange method exhibits the same beneficial attributes noted for the cubic spline method.

The Lagrange interpolating polynomial is defined by

$$f_n(x) = \sum_{i=0}^{m} L_i(x) f(x_i) \tag{3.6}$$

where

$$L_i(x) = \prod_{\substack{j=0 \\ j \neq i}}^{m} \frac{x - x_j}{x_i - x_j} \tag{3.7}$$

where m is the order of the polynomial passing exactly through the $m + 1$ known data points and $\prod$ means the product of. Thus, the polynomial for each red curve in Fig. 3.6 is of the form

$$\begin{aligned} f(x) = {} & \frac{(x - x_1)(x - x_2)}{(x_0 - x_1)(x_0 - x_2)} f(x_0) + \frac{(x - x_0)(x - x_2)}{(x_1 - x_0)(x_1 - x_2)} f(x_1) \\ & + \frac{(x - x_0)(x - x_1)}{(x_2 - x_0)(x_2 - x_1)} f(x_2). \end{aligned} \tag{3.8}$$

The resulting discretized mesh created by the mesh generation code from the modeled test section boundaries consists of hexahedral cells clustered in the near-wall region and aligned axially with the test section and thus the fluid flow. To provide further control over the near-wall mesh clustering with respect to wall y^+ and to facilitate ease of implementing grid refinement ratios for the grid convergence study, the ability to specify constraints on the first cell layer thickness, surface growth rate, and maximum cell size was added to the code.

The mesh generation code accepts each of the additional constraints for the mesh from the user at runtime. The first cell layer thicknesses specified for the walls are then subtracted from H in Eqs. 3.2 and 3.3. The code then iterates on the number of points, dη, and the ζ parameter of the hyperbolic equations with the reduced H until the maximum cell size and

surface growth rate constraints are satisfied. Each of the additional parameter constraints is described below and the FORTRAN code with the as-built measurement files may be viewed in Appendix G.

3.1.2.1 Maximum Cell Size

The maximum cell size parameter, MCS, sets the maximum length that a hexahedral cell may be in any coordinate axis, see Fig. 3.7. This ability enables simple specification of grid refinement ratios for the grid convergence study and it also defines how coarse the mesh is in the freestream region of the flow.

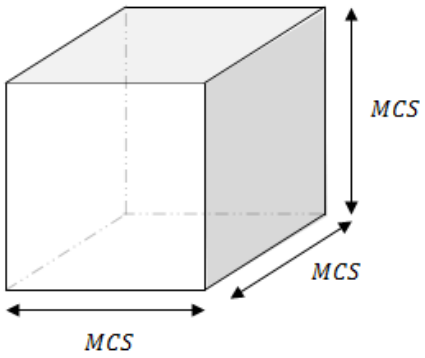

Fig. 3.7: Discretized cell exhibiting the maximum cell size (MCS) permitted.

3.1.2.2 First Cell Layer Thickness

The first wall cell layer thickness parameter, t, sets the thickness of the layer of cells that is immediately next to a wall boundary, as shown in Fig. 3.8. This ability streamlines the mesh generation process because the mesh can be more easily and directly refined to provide a mesh that gives $y^+ \approx 1$ in the first cell layer. The mesh generation code allows specification of this parameter for the heated wall, side walls, top wall and the inlet of the test section geometry. The inlet specification is not specified for y^+ reasons, but rather to aid the simulation in resolving the inlet flow as it develops from the contraction preceding the test section.

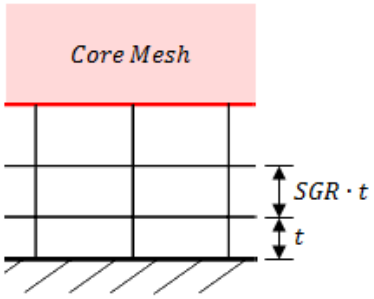

Fig. 3.8: Illustration of the first wall cell layer thickness (t) and surface growth rate (SGR) parameters.

3.1.2.3 Surface Growth Rate

The surface growth rate parameter, SGR, specifies the ratio of the second to the first wall cell layer thickness, shown in Fig. 3.8. This parameter was required in the mesh generation code to enable a smooth transition from the specified first cell layer thickness to the hyperbolic distribution of interior points.

3.1.3 Discretized Mesh

A set of three consecutively refined discretized meshes were created for each validation case. Tables 3.1 and 3.2, contain the meshing parameters and hyperbolic clustering/placement parameters used to generate the discretized meshes as well as parameters characteristic of generated mesh: cell count and maximum skewness angle. The columns 1, 2 and 3 shown in the tables correspond to the first, second and third level of mesh refinement in the set of meshes for each validation case, 3 representing the coarsest mesh and 1 the most refined.

Because the MCS parameters used to generate each set of discretized meshes were the same, the set of meshes for each validation case are generally similar. The difference between each set lies in the near-wall cell distribution, which was tailored to give $y^+ \approxeq 1$ in the first cell adjacent to the wall. The tailoring of each set of meshes was achieved by iteratively creating a mesh and running a CFD simulation to check the wall y^+. Due to the similarity between the sets of meshes, only an exemplary mesh is illustrated here.

Table 3.1: Parameters used in generating the discretized meshes for the M1 and F1 validation cases and characteristic parameters of the resulting meshes. Note: A, HP, TW, and SW, respectively, denote axial, heated plate, top wall, and side walls.

	M1			F1		
Parameter	1	2	3	1	2	3
SGR		1.05			1.05	
t_A (m)		0.0025			0.0025	
t_{HP} (m)		0.0003			0.0002	
t_{TW} (m)		0.000235			0.00015	
t_{SW} (m)		0.000235			0.00015	
MCS (m)	0.0035	0.005	0.007	0.0035	0.005	0.007
ζ_A	2.00068	1.45109	1.26534	2.00068	1.45109	1.26534
ζ_{HP}	1.05141	1.03469	1.02374	1.03349	1.02282	1.01582
ζ_{TW}	1.03661	1.02500	1.01725	1.02284	1.01572	1.01098
ζ_{SW}	1.03656	1.02496	1.01745	1.02281	1.01570	1.01096
σ		1/2			1/2	
# Cells	20482880	9290400	4333500	24686420	11095866	5133375
Max Skewness Angle	4.023°	5.277°	6.853°	5.741°	7.563°	9.862°

Table 3.2: Parameters used in generating the discretized meshes for the M2 and F2 validation cases and characteristic parameters of the resulting meshes. Note: A, HP, TW, and SW, respectively denote axial, heated plate, top wall, and side walls.

	M2			F2		
Parameter	1	2	3	1	2	3
SGR		1.05			1.05	
t_A (m)		0.0025			0.0025	
t_{HP} (m)		0.0003			0.0002	
t_{TW} (m)		0.000225			0.000125	
t_{SW} (m)		0.000225			0.000125	
MCS (m)	0.0035	0.005	0.007	0.0035	0.005	0.007
ζ_A	2.00362	1.45186	1.26426	2.00362	1.45186	1.26426
ζ_{HP}	1.05197	1.03488	1.02425	1.03518	1.02394	1.01649
ζ_{TW}	1.03487	1.02373	1.01665	1.01889	1.01306	1.00910
ζ_{SW}	1.03489	1.02374	1.01666	1.01890	1.01295	1.00910
σ		1/2			1/2	
# Cells	20930580	9423594	4443494	26680500	11907828	5475734
Max Skewness Angle	9.007°	11.794°	15.112°	14.241°	18.688°	24.047°

Figs. 3.9–3.11 show the cross-sectional cell distribution for each level of mesh refinement with a close up view of the near-wall refinement.

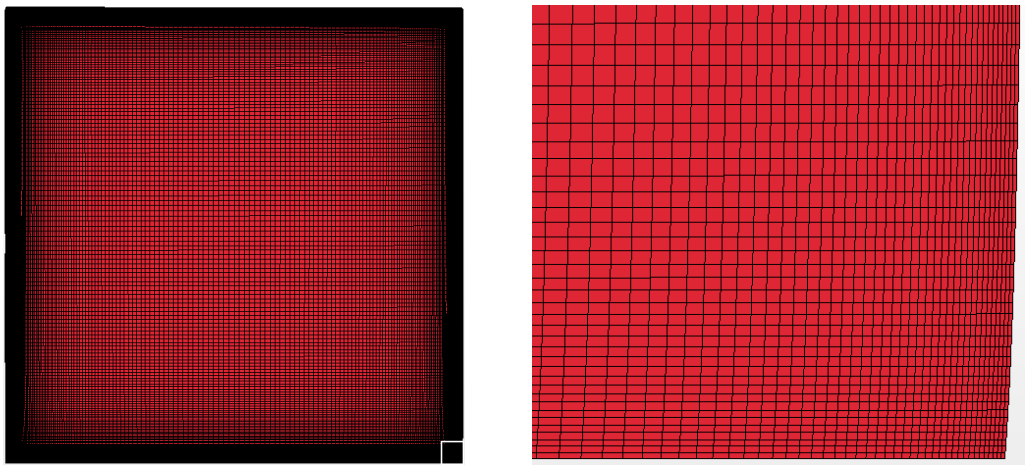

Fig. 3.9: Cross-section of the discretized mesh with first level refinement. The near-wall corner refinement inside the designated white area is shown on the right.

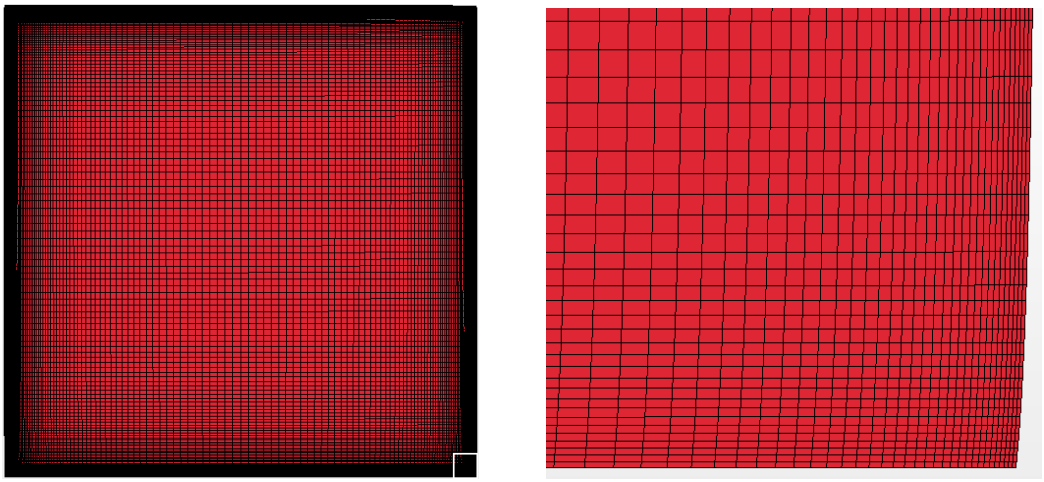

Fig. 3.10: Cross-section of the discretized mesh with second level refinement. The near-wall corner refinement inside the designated white area is shown on the right.

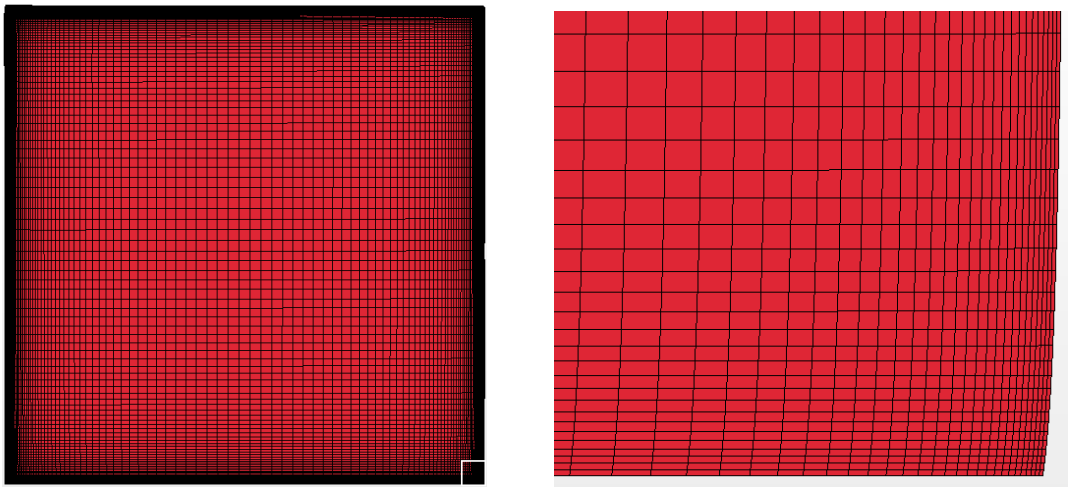

Fig. 3.11: Cross-section of the discretized mesh with third level refinement. The near-wall corner refinement inside the designated white area is shown on the right.

Fig. 3.12 illustrates the characteristics attributed to every mesh used in this study: a uniform cross-sectional cell distribution throughout the computational domain and a gradual coarsening of the mesh in the axial direction from the inlet to the outlet.

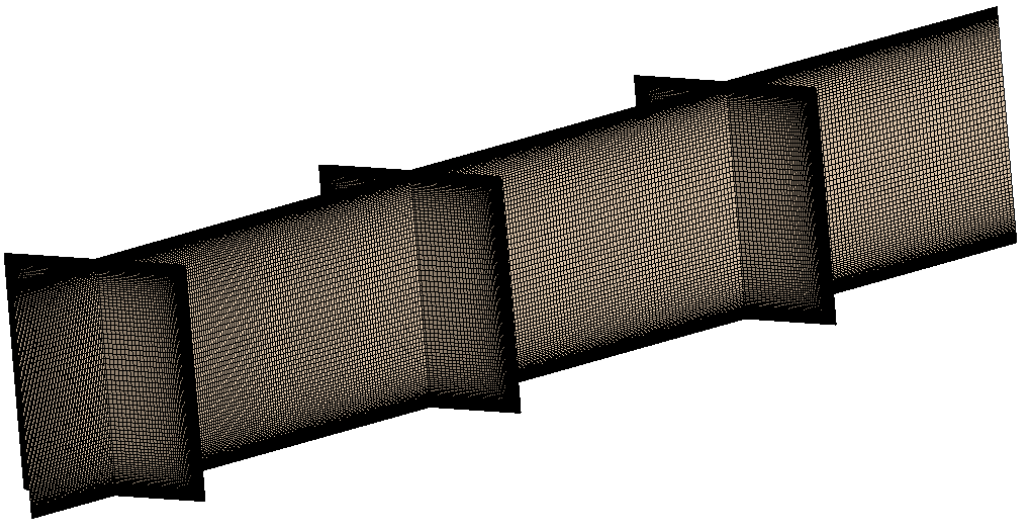

Fig. 3.12: Illustration of the coarsest discretized mesh, showing the mesh distribution on cross-sectional planes at each heat flux sensor location as well as the vertical centerline plane.

Table 3.3: Average y^+ value from the three heat flux sensor locations for each validation case.

	Average First Cell y^+ Value			
Turbulence Model[1]	M1	F1	M2	F2
R2L	0.93	0.95	0.98	1.00
S2L	0.92	0.91	0.99	1.00
SLR	0.82	0.82	0.87	0.88
V2F	0.89	0.95	0.93	1.00
$k-\omega$	0.90	0.94	0.96	1.00
SST	0.87	0.89	0.91	0.99
RST	0.95	0.98	0.98	1.03
SA	0.85	0.93	0.92	1.03
R2LB	1.34	1.37	1.41	1.43
S2LB	1.22	1.18	1.31	1.30
RSTB	1.47	1.51	1.53	1.58

[1] The turbulence model acronyms are defined in Section 3.2.7.

This distribution of cells in the computational domain met all of the cell refinement and cell skewness attributes desired for this validation study, discussed in section 3.1. As depicted in the above figures, the computational domain is partitioned smoothly, with refinement on the walls to resolve the viscous sub-layer and regular cells in the freestream region, which minimized cell skewness. Tables 3.1 and 3.2 show that the maximum cell skewness angle for all of the meshes used is well below the STAR-CCM+ recommended 85°. Also, Table 3.3 shows that the near-wall refinement for each validation case met the desired $y^+ \approxeq 1$ by each turbulence model validated.

3.1.4 Grid Refinement

A vital part of CFD as a numerical method is estimating the discretization error or numerical uncertainty in the solution. As explained previous, a discretized mesh allows for numerical simulations to predict physics in reality by discretizing or partitioning a normally continuous region into volumetric cells. A single cell however cannot account for all the physics occurring in the corresponding continuous region in reality; thus, a discretized mesh

inherently contains errors. To investigate this error, a grid refinement and/or coarsening of the discretized computational domain is carried out in order to analyze the solution behavior as the mesh resolution changes. Each turbulence model in this validation study was solved over three consecutively refined meshes, see Figs. 3.9–3.11, and the resulting solutions were compared using the grid convergence index (GCI) method to evaluate the discretization error.

The GCI method is the recommended method by the American Society of Mechanical Engineers (ASME) for estimation of discretization error, which is based on the Richardson Extrapolation method. The GCI method is outlined in the following section, with the results presented in Chapter 5.

GCI Method

The GCI method consists of five steps, resulting in an extrapolated value for a given variable (ϕ) to an infinitely fine mesh as well as an estimation of the numerical uncertainty [33]. The five steps are:

Step 1

A representative cell or grid size, h, is defined for each mesh, which for three-dimensional space is defined as

$$h = \frac{1}{N}\sum_{i=1}^{N}(\Delta V_i), \tag{3.9}$$

where ΔV_i is the volume the i^{th} cell, and N is the total number of cells. For this study, given that the validation variables are only dependent on the local fluid flow, h is specified locally using only the cells in the first cell layer adjacent to the heated wall boundary.

The representative cell sizes for the three different meshes used are h_1, h_2 and h_3, where h_1 represents the finest mesh and h_3 represents the coarsest, such that $h_1 < h_2 < h_3$.

Step 2

The key variables of interest, ϕ, important to the simulation study objective are obtained from completed simulations. For this study, the key variables are the wall heat flux (q") and the u and v velocity vector components.

Step 3

The apparent order, p, of the numerical method is calculated using the expression

$$p = \frac{1}{ln(r_{21})}|ln|\varepsilon_{32}/\varepsilon_{21}| + q(p)|, \tag{3.10a}$$

$$q(p) = ln\left(\frac{r_{21}^{p} - s}{r_{32}^{p} - s}\right), \tag{3.10b}$$

$$s = 1 \cdot sign(\varepsilon_{32}/\varepsilon_{21}), \tag{3.10c}$$

where $r_{21} = h_2/h_1$, $r_{32} = h_3/h_2$, $\varepsilon_{21} = \phi_2 - \phi_1$, $\varepsilon_{32} = \phi_3 - \phi_2$ and ϕ_k denoting the k^{th} grid. Agreement of the observed apparent order and the formal order are a good indication that the meshes used are in the asymptotic convergence range; however, poor agreement does not necessarily indicate poor calculations [33].

It is noted that if either ε_{21} or ε_{32} is very close to zero, then the above procedure is invalid. Zero values may indicate that the exact solution has been reached or may be a result of oscillatory convergence, which is denoted by values of $\varepsilon_{32}/\varepsilon_{32} < 0$.

Step 4

The value of ϕ extrapolated to $h = 0$ is calculated from

$$\phi_{ext}^{21} = (r_{21}^{p}\phi_1 - \phi_2)/(r_{21}^{p} - 1). \tag{3.11}$$

Step 5

The apparent numerical order is reported along with the approximate relative error (e_a^{21}), extrapolated relative error (e_{ext}^{21}), and the fine-grid convergence index (GCI_{fine}^{21}) obtained respectively from

$$e_a^{21} = \left| \frac{\phi_1 - \phi_2}{\phi_1} \right|, \tag{3.12}$$

$$e_{ext}^{21} = \left| \frac{\phi_{ext}^{21} - \phi_1}{\phi_{ext}^{21}} \right|, \tag{3.13}$$

$$GCI_{fine}^{21} = \frac{1.25 e_a^{21}}{r_{21}^p - 1}; \tag{3.14}$$

where GCI_{fine}^{21} is the numerical uncertainty of ϕ_1 as a decimal percentage.

For profiles of key variables, it is recommended that the numerical uncertainty be indicated with error bars. The error bar magnitudes are computed by using Eq. 3.14 above in conjunction with an average value of $p = p_{avg}$, calculated by averaging p from GCI studies at every point in the variable profile, as a measure of the global order of accuracy.

3.2 Physics

The physics models make up the governing momentum, energy and turbulence equations to be solved over the computational domain. The STAR-CCM+ CFD package contains many physics models, from which specific models are brought together to simulate a given physical phenomena. The physics models used in the CFD simulations for this validation study include: three dimensional, gradients, gravity, gas, ideal gas, steady, coupled flow, coupled energy, turbulent, Reynolds-averaged Navier–Stokes and select turbulence models and wall treatments. The three dimensional and gradients models are base building blocks for the solver in STAR-CCM+ needed to allow three dimensional computations and calculate parameter diffusion and convection. The remaining physics models were specifically chosen to model the buoyant, turbulent flow heat transfer in the validation cases of this study.

An explanation for each model selected, along with any changed default parameters or options, is given in the following sections. For further details and explanations of the

STAR-CCM+ physics models the reader is referred to the STAR-CCM+ user manual [31].

3.2.1 Gravity

The gravity model accounts for gravitational acceleration in the simulations. For the fluid in this study, the model allows use of the piezometric pressure as the working pressure and also enables the use of the gravity body force in the momentum equations. Thus, without this model the effects of buoyancy could not be properly calculated.

3.2.2 Gas

The gas model specifies the simulation working fluid as a pure gas. Numerous types of gases may be assigned as the working fluid each with specified default values for dynamic viscosity (μ), molecular weight (M), specific heat (c_p), thermal conductivity (k^*) and turbulent Prandtl number (Pr_t).

Air is the working fluid in the experiments validated by this study, in order to account for changes to its properties due to the heat transfer in the boundary layer the dynamic viscosity was enabled to vary according to Sutherlands Law,

$$\frac{\mu}{\mu_0} = \left(\frac{T}{T_0}\right)^{3/2} \left(\frac{T_0 + S}{T + S}\right), \tag{3.15}$$

with $\mu_0 = 1.827E\text{-}5$ Pa-s, $S = 120.0$ K and $T_0 = 291.15$ K. The default values for the remaining fluid properties were used, specified as:

$$M = 28.9664 \text{ kg/kmol}$$

$$c_p = 1003.62 \text{ J/kg-K}$$

$$k^* = 0.0260305 \text{ W/m-K}$$

$$Pr_t = 0.9$$

3.2.3 Ideal Gas

The ideal gas model was chosen as the fluid equation of state because air is considered

to be an ideal gas. Furthermore, the ideal gas model enables the fluid density to be a function of temperature and pressure, as defined below in the ideal gas law

$$\rho = \frac{p^*_{abs}}{RT} \tag{3.16}$$

with

$$p^*_{abs} = p^*_{static} + p^*_{ref} \tag{3.17}$$

$$R = R_u/M \tag{3.18}$$

where ρ is the density, p^*_{abs} is the absolute pressure, R is the specific gas constant dependent on the universal gas constant R_u and T is the temperature.

The pressure dependency of the model may be restricted to depend only on the reference pressure (p_{ref}) by assuming that the flow is incompressible. Though incompressible flow may reasonably be assumed in the validation cases of this study, the fluid was solved as a compressible flow in order to facilitate the accounting of all effects of the heat transfer. Allowing this enabled the static pressure (p^*_{static}) in the equation above to account for buoyancy effects enabled by the gravity model as

$$p^*_{static} = \tilde{p} + \rho_{ref} \cdot g(x - x_0), \tag{3.19}$$

where the working pressure ($\tilde{p}$) is the piezometric pressure.

3.2.4 Steady

The steady temporal discretization model removes any time varying values and calculations from the CFD simulation and attempts to converge on a steady-state solution, which can be difficult in a turbulent flow simulation due to the inherent complex instabilities. The instabilities of turbulent flow often requires obtaining a solution through an unsteady time model, which steps the solution out in time, converging the solution at each time step, until the solution reaches an unchanging state. However, unsteady models exchange enhanced

solver stability for longer solution convergence times.

The steady model was chosen for this study despite possible convergence complications because, first, the uniformity of the experimental flow which occurred the test section alleviated concerns that the turbulent instabilities would inhibit solution convergence, and second, due to the number of turbulence models selected for validation, and thus the number of simulations to be completed, extensive convergence times were impractical.

3.2.5 Coupled Flow and Coupled Energy

The coupled flow and coupled energy models solve the governing equations for mass, momentum and energy simultaneously. The complex internal and external buoyancy effects between the fluid flow and energy balance require the governing equations to be solved simultaneously.

3.2.6 Turbulent and Reynolds-Averaged Navier–Stokes

The viscous regime in STAR-CCM+ contains three distinct approaches to modeling a flow that is in a state of continuous instability, exhibiting irregular, small-scale, high-frequency fluctuations in both space and time [31]. The three approaches include: Reynolds-Averaged Navier–Stokes, Large Eddy Simulation (LES) and Detached Eddy Simulation (DES).

This study is focused on validation of turbulence models that use the Reynolds-Averaged Navier–Stokes (RANS) approach. The RANS approach to solving turbulent flow involves the decomposition of the Navier–Stokes equations into mean and fluctuating components. The resulting equations for the mean quantities are similar to the original Navier–Stokes equations, except for an additional stress term in the momentum transport equation, T_t, termed the Reynolds stress tensor. Two general approaches are available in STAR-CCM+ to solve the Reynolds stress tensor and thereby provide closure to the governing equations: Reynolds stress transport and eddy viscosity.

The Reynolds stress transport approach, also known as second-moment closure, directly solves a transport equation for each component of the Reynolds stress tensor. Conversely,

the eddy viscosity approach uses the concept of a turbulent viscosity (μ_t) to model the Reynolds stress tensor as a function of the mean flow quantities; the function used in STAR-CCM+ is the Boussinesq approximation

$$T_t = 2\mu_t \mathbf{S} - \frac{2}{3}(\mu_t \nabla \cdot \mathbf{v} + \rho k)\mathbf{I} \tag{3.20}$$

where S is the strain rate tensor and k is the turbulent kinetic energy:

$$\mathbf{S} = \frac{1}{2}(\nabla \mathbf{v} + \nabla \mathbf{v}^T) \tag{3.21}$$

$$k = \frac{1}{2}(\overline{u'u'} + \overline{v'v'} + \overline{w'w'}) \tag{3.22}$$

The $k - \varepsilon$, $k - \omega$ and Spalart–Allmaras eddy viscosity methods in STAR-CCM+ solve additional transport equations in order to obtain μ_t.

3.2.7 Turbulence Models

Eleven turbulence models from the Reynolds stress, $k-\varepsilon$, $k-\omega$ and Spalart–Allmaras RANS turbulence methods were validated using the SRQ data provided by the EFDL RoBuT research group. All of the models utilized 2nd order upwind convection schemes and all of the default solver parameters set by STAR-CCM+ were accepted unless otherwise stated in the following brief descriptions of each model:

3.2.7.1 Reynolds Stress Transport

The Reynolds stress transport (RST) model solves seven transport equations in addition to the mass, momentum and energy equations, including six for each unique stress in the Reynolds stress tensor and a model equation for the isotropic turbulent dissipation rate (ε). The solution of the additional transport equations allows the RST to naturally account for the anisotropic effects of turbulent fluid flow due to strong swirling motions, streamline curvature, rapid changes in strain rate and secondary flows.

In this study, two RST models implementing the linear pressure strain two-layer formulation were validated; one applying the shear driven two-layer formulation recommended for flows not dominated by buoyancy, and the second applying the buoyancy driven two-layer formulation (denoted RSTB).

3.2.7.2 $k-\varepsilon$: Standard Two-Layer

The standard $k-\varepsilon$ two-layer (S2L) model combines the standard $k-\varepsilon$ model with the two-layer approach to solving the viscous sub-layer flow. The standard $k-\varepsilon$ model solves transport equations for the turbulent kinetic energy (k) and the turbulent dissipation rate (ε) in order to compute μ_t. The equations are of the form suggested by Jones and Launder [34], with coefficients suggested by Launder and Sharma [10].

The S2L model was included in the validation study because the literature review showed it to be among the turbulence models most suited to computing buoyant flow [23]. As with the RST models, two S2L models were validated with the shear and buoyancy driven (denoted S2LB) two-layer formulations as well as with the Yap correction for ε, non-linear quadratic constitutive relations and Durbin realizability solver options in STAR-CCM+.

3.2.7.3 $k-\varepsilon$: Standard Low-*Re*

The governing transport equations of the $k-\varepsilon$ low-Re (SLR) model by Lien *et al.* [35] are identical to those of the standard $k-\varepsilon$ model, but the damping function enabled equation coefficients permit the viscous-affected near-wall flow to be resolved. The damping functions modulate the coefficients as functions of the turbulent Reynolds number, often also incorporating the wall distance. STAR-CCM+ recommends this model for natural convection problems, particularly if the Yap correction is enabled [31].

The SLR model validated included the Yap correction for ε, non-linear-quadratic constitutive relations and Durbin realizability constraints.

3.2.7.4 $k-\varepsilon$: Realizable Two-Layer

The realizable $k-\varepsilon$ two-layer (R2L) model is a fairly recent $k-\varepsilon$ turbulence model

by Shih *et al.* containing a new transport equation for the turbulent dissipation rate (ε) and also allows the critical C_μ coefficient to be a function of mean flow and turbulence properties rather than an assumed constant [36], as in the Standard $k-\varepsilon$ model [31]. The variable C_μ concept is consistent with experimental findings.

Two R2L models were validated employing the shear driven and buoyancy driven (denoted R2LB) two-layer formulations.

3.2.7.5 $k-\varepsilon$: v^2-f

The v^2-f $k-\varepsilon$ (V2F) model solves transport equations for the normal stress and elliptic turbulence quantities in addition to k and ε. Thus, the V2F model has more computational overhead than the other $k-\varepsilon$ models, but it is able to more accurately capture the near-wall turbulence effects critical to predicting heat transfer, skin friction and flow separation [37–39]. The turbulence model assessments in the literature found the V2F model to give the best results in heat transfer flow calculations [22, 23].

3.2.7.6 $k-\omega$: Standard

The $k-\omega$ model is an alternative two-equation turbulence model to the $k-\varepsilon$ model. The turbulence transport equations solve for the turbulent kinetic energy (k) and the specific dissipation rate (ω), the turbulent dissipation rate per unit turbulent kinetic energy ($\omega \sim \epsilon/k$). This formulation of the governing equations may be applied throughout the boundary layer without requiring a two-layer or low-Re modification to resolve the viscous sub-layer. Furthermore, the application of the model transport equations is achieved without computing the wall distance. STAR-CCM+ reports that the $k-\omega$ model provides improved performance in modeling boundary layers under adverse pressure conditions [40].

3.2.7.7 $k-\omega$: Shear Stress Transport with Gamma ReTheta Transition

The shear-stress transport or SST $k-\omega$ (SST) model was derived by Menter to address the original $k-\omega$ models sensitivity to freestream and inlet conditions [41]. Menter derived a new form of the $k-\omega$ transport equations by introducing a variable substitution into the

standard $k-\varepsilon$ equations; the resulting equations included a non-conservative cross-diffusion term containing the $\nabla k \cdot \nabla \omega$ dot product. This term effectively blends a $k-\varepsilon$ model in the far-field or freestream flow with a $k-\omega$ model in the near-wall region. The resulting model dampens the sensitivity of the model to the inlet conditions.

The gamma Retheta transition model was included in the SST model for this validation study to account for possible laminarization of the turbulent flow due to buoyancy. The gamma Retheta correlation-based model investigates turbulent flow transition by relating the vorticity-based Reynolds number, which can be calculated on an unstructured CFD grid, to the momentum thickness Reynolds number.

3.2.7.8 Spalart–Allmaras

The Spalart–Allmaras (SA) model solves a single transport equation to determine the turbulent viscosity (μ_t). The model was originally developed primarily for aerodynamic flow applications, such as flow past a wing [42]. However, the SA model is a low-Reynolds number model, meaning that it is specifically formulated to accurately resolve the entire turbulent boundary layer, including the viscous sub-layer critical to the calculation of boundary heat transfer. Despite the resolution of the boundary layer however, free-shear spreading rates predicted for jet-like free-shear regions are inaccurate [40]; therefore, the SA model may be ill-suited to flows with complex recirculation or body forces.

3.3 Boundary Conditions

Boundary conditions inform the CFD solver, the governing mass, momentum, energy and turbulence equations, how the substance within the computational domain interacts with its environment. As shown in Fig. 3.13, the six bounding surfaces of the computational domain are assigned distinct boundary types, including: wall, velocity inlet, and pressure outlet. Each boundary has its own properties for physics conditions and physics values. All of the data required to prescribe each physics condition and value was obtained from the EFDL RoBuT experiments. Each boundary type used in the validation study is discussed below.

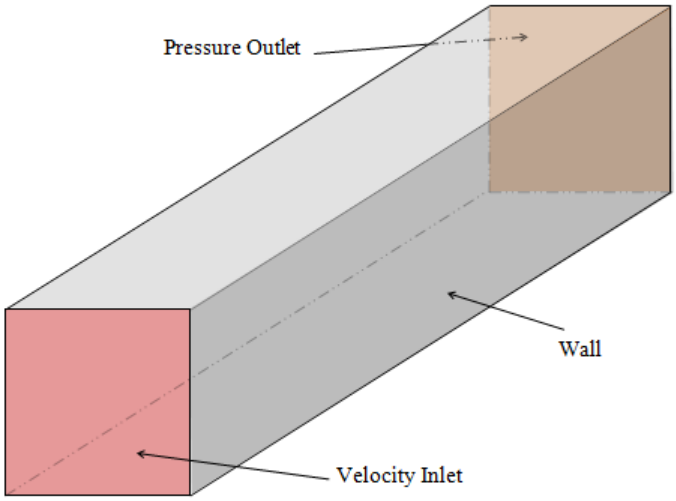

Fig. 3.13: Illustration of the computational domain with the distinct boundary conditions labeled.

3.3.1 Wall

The wall boundary represents an impermeable no-slip surface with a defined thermal state or temperature condition. Figs. 3.14–3.17 below show the thermal boundary conditions mapped onto the test section walls and inlet for each of the four validation cases, where the leading edge of the test section is at the top of the illustrated heated wall on the right of each figure.

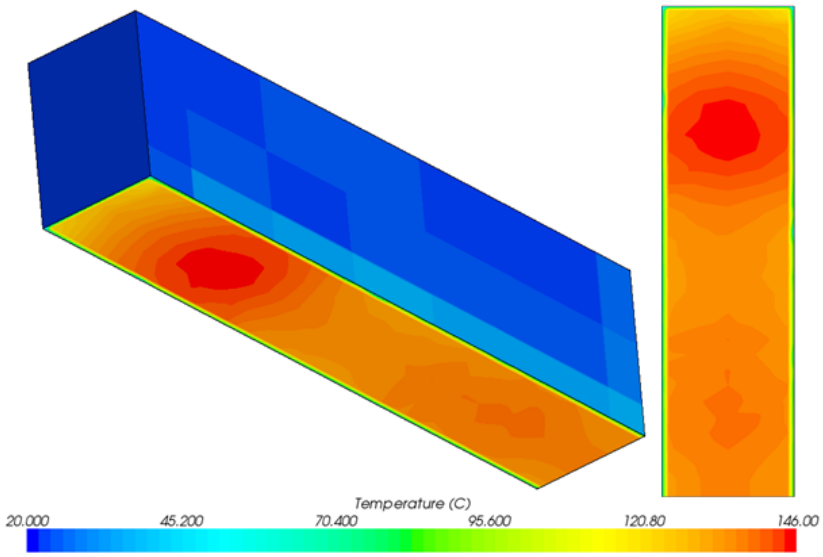

Fig. 3.14: Thermal boundary conditions for the M1 validation case.

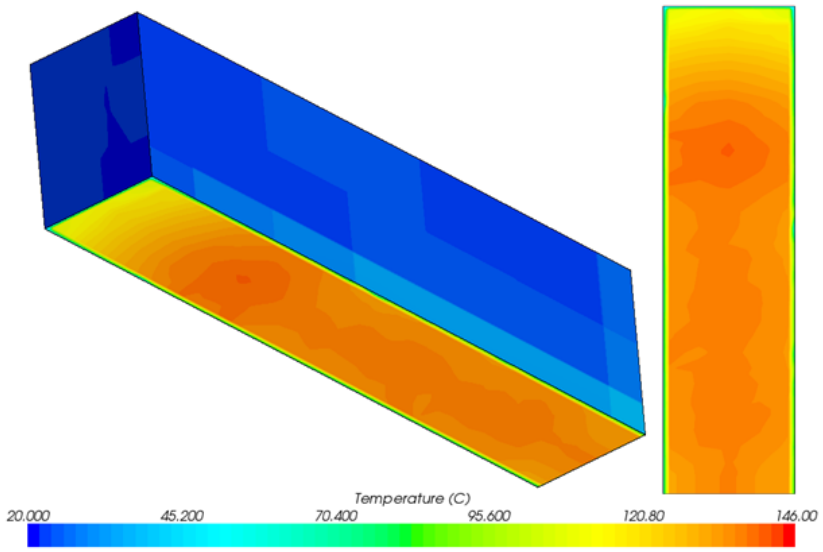

Fig. 3.15: Thermal boundary conditions for the F1 validation case.

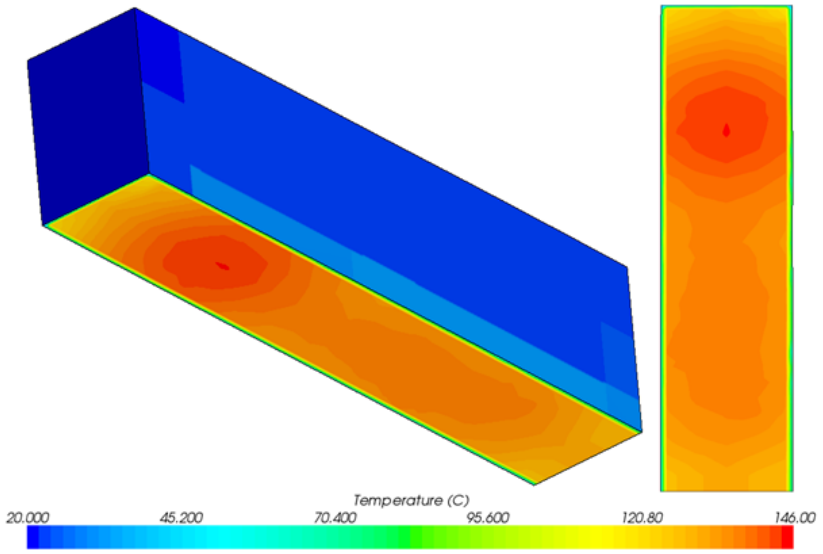

Fig. 3.16: Thermal boundary conditions for the M2 validation case.

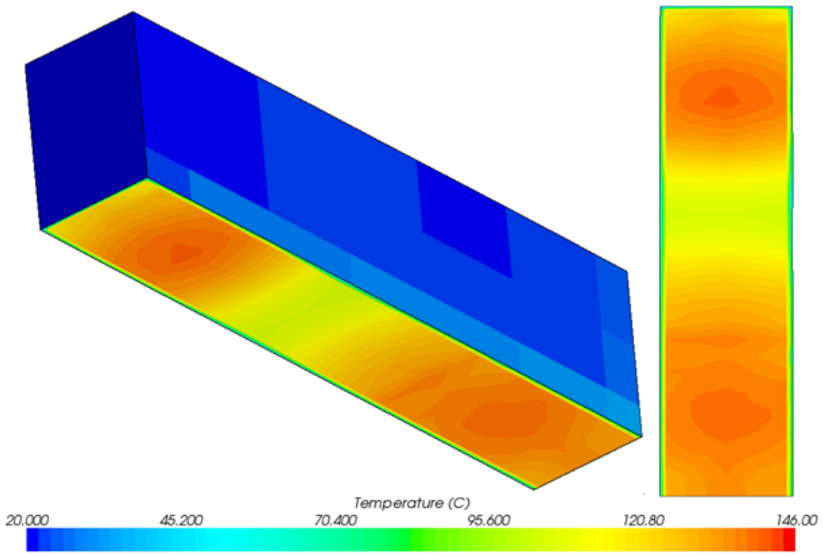

Fig. 3.17: Thermal boundary conditions for the F2 validation case.

The thermal state of the heated wall for each RoBuT experiment was only dependent on the thermocouples located at each of the three heat flux sensor locations. Thus, the

targeted thermal state for each experiment can be more critically viewed as having been obtained along the heated wall centerline.

In each CFD simulation, wall treatments are the set of near-wall modeling assumptions for each turbulence model in STAR-CCM+. Three types of wall treatments are available in STAR-CCM+, dependent on the y^+ value of the cell adjacent to the wall:

- The high y^+ wall treatment, for $y^+ \geq 30$, implements a wall function as described in Chapter 1 to account for boundary layer flow.
- The low y^+ wall treatment, for $y^+ \approxeq 1$, is suited only for low-Reynolds number turbulent models were it is assumed that the near wall mesh is sufficiently refined to resolve the viscous sub-layer flow.
- The all y^+ wall treatment is a hybrid treatment that attempts to emulate the high y^+ treatment in coarse regions of the discretized mesh, and the low y^+ treatment for fine regions. The formulation also allows for a blend of the wall treatments on intermediate mesh resolutions.

As shown in Section 3.1.3, the discretized mesh for this validation study has been refined to resolve the viscous sub-layer of the turbulent flow boundary layer. The all y^+ wall treatment was implemented on all of the turbulence models in the study in order to be uniform and to enable the low y^+ wall treatment calculations on all of the models.

In conjunction with the all y^+ wall treatment, the two-layer models validated (RST, R2L and S2L) prescribe ε and μ_t as functions of wall distance in the flow layer next to the wall. Thereafter the values of ε are blended smoothly with the values computed by the respective models transport equation. The transport equation for k is solved in the entire flow.

3.3.2 Velocity Inlet

The velocity inlet boundary represents a region allowing fluid mass and momentum to enter the computational domain where the fluid velocity is known. For the assigned velocity

inlet boundary of the computational domain, the turbulence and thermal physics properties as well as the inflow velocity vector components are specified. In this study, several turbulence specifications were used to specify the turbulence of the inlet flow, including the following combinations: k and ε, k and ω, and modified turbulent diffusivity. The values used were obtained from the RoBuT experiments for each validation case.

The PIV system described in Chapter 2 was used to acquire nine profiles across the inlet of the RoBuT test section. See reference [26] for details about the specific profiles. Two-component PIV was used at each of the nine profiles, thus only the in-plane velocities were measured. Previous cross examination of two orthogonal plane PIV studies by the EFDL researchers showed that the transverse velocities were symmetric in the freestream of the test section inlet, meaning $w = v$. Thus, the three velocity components u, v, and w are specified by two-component PIV measurements in the X-Y plane at each of the measured PIV points.

In order to create a more continuous profile of the velocity, the EFDL researchers wrote a Matlab code to interpolate the measured PIV velocity components over a fine grid to be used in this validation study. The velocity mapped onto the inlet for the F2 case is in Figs. 3.18 and 3.19, the mapped velocities for the other validation cases are similar to those shown and are contained in Appendix A.

The turbulence quantities at the inlet were obtained in the above mentioned Matlab code by processing the interpolated PIV data. k and ε were obtained directly using the PIV data, see Eqs. 3.22 and 3.23, and the correlations in Eqs. 3.24 and 3.25 were then used to obtain values for the specific dissipation rate and the modified turbulent diffusivity.

It is recognized that the interpolation process implemented in the Matlab code probably induced incorrect gradients in the velocity and turbulence distributions used at the inlet, and is therefore a significant source of error in the results. However, importing the PIV velocity data directly into STAR-CCM+ for the inlet conditions would have created a 'blocky' inlet distribution, which probably would have instilled a larger input error on the CFD simulation due to the discontinuities present than the interpolated distribution.

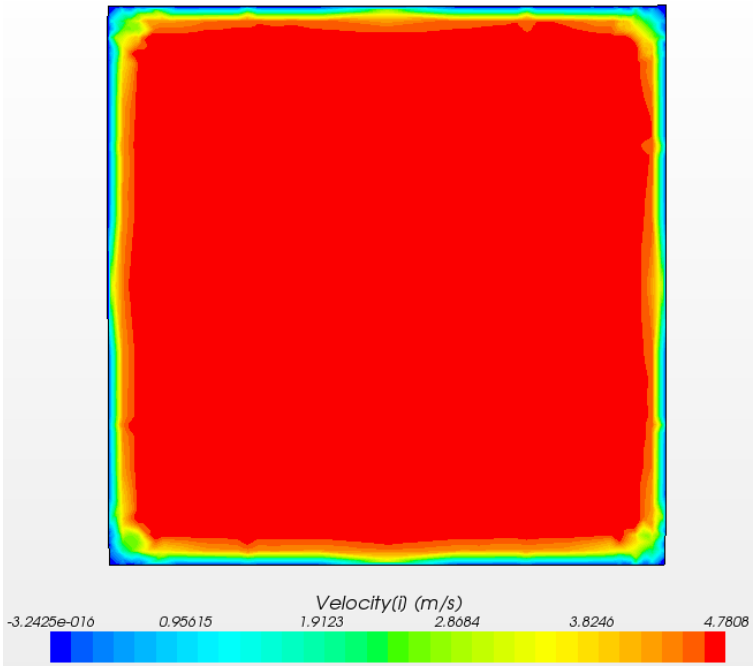

Fig. 3.18: u velocity mapped onto the velocity inlet of the computational domain.

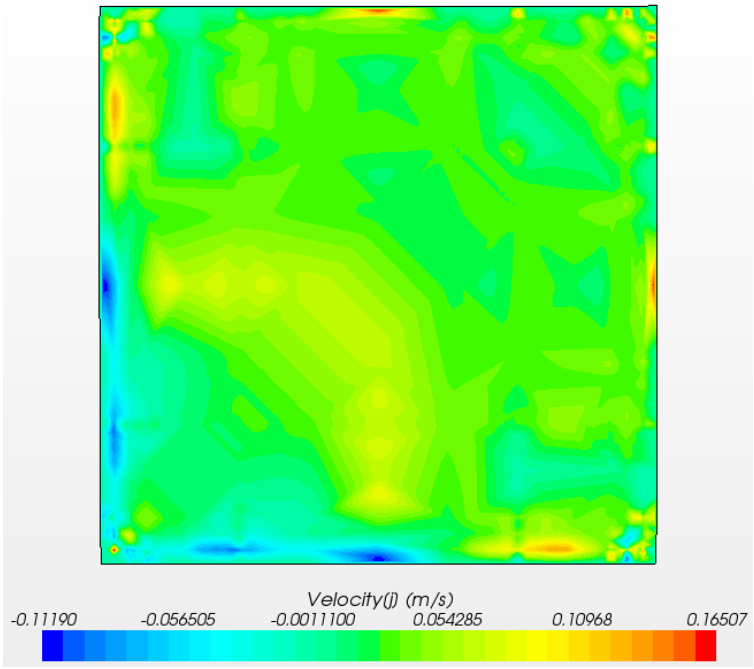

Fig. 3.19: v and w velocity mapped onto the velocity inlet of the computational domain.

Kays, Crawford, and Weigand define the Reynolds decomposition of the instantaneous velocity as the sum of the mean ($\bar{u}$) and fluctuating (u') components, that is $u = \bar{u} + u'$ [6], which enables k to be calculated as from Eq. 3.22 with u, v and w being the fluctuating components in the x, y and z coordinate axis. Each fluctuating component is set equal to the variance (square of the standard deviation) of the time averaged velocity from the two component PIV inlet measurements, with $w = v$ as implied by the symmetric inlet velocity.

The turbulent dissipation rate (ε) was approximated from the two-component PIV data as

$$\varepsilon = 2\nu \left\{ \left(\overline{\frac{\partial u'}{\partial x}} \right)^2 + \left(\overline{\frac{\partial v'}{\partial y}} \right)^2 + \frac{3}{2} \left[\left(\overline{\frac{\partial u'}{\partial y}} \right)^2 + \left(\overline{\frac{\partial v'}{\partial x}} \right)^2 \right] + \overline{\frac{\partial u'}{\partial y} \frac{\partial v'}{\partial x}} \right\}, \tag{3.23}$$

were ν is kinematic viscosity and turbulence is assumed to be isotropic [43].

From the derived values for k and ε, the specific dissipation rate (ω) and modified turbulent diffusivity ($\tilde{\nu}$) were calculated from

$$\omega = \frac{\varepsilon}{C_\mu k}, \tag{3.24}$$

$$\tilde{\nu} = \frac{C_\mu^{3/4} k^2}{\varepsilon}, \tag{3.25}$$

were $C_\mu = 0.09$, the default value used in the validation simulations set by STAR-CCM+.

The following figures depict the various turbulence specifications for the F1 validation case as they were mapped onto the computational domain inlet; the turbulence specification profiles for the other validation cases are similar and are contained in Appendix B.

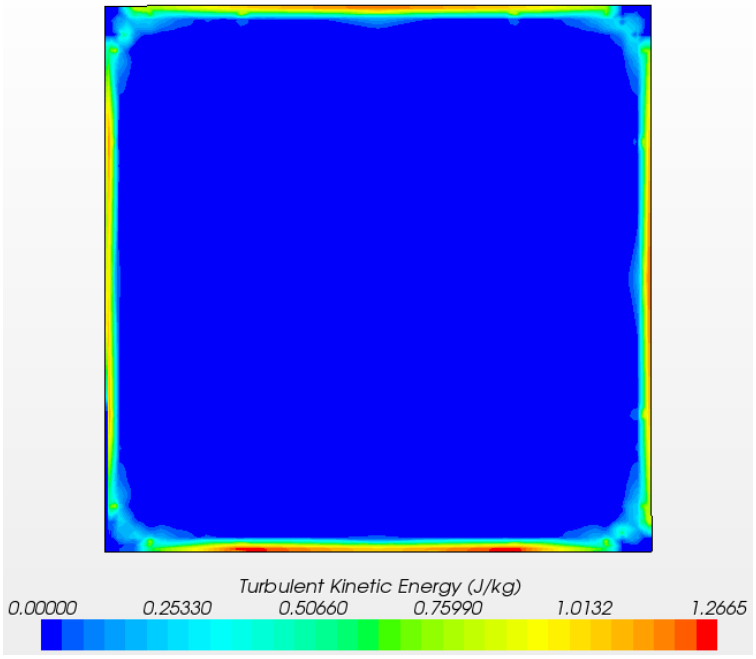

Fig. 3.20: Turbulent kinetic energy (k) mapped onto the velocity inlet of the computational domain.

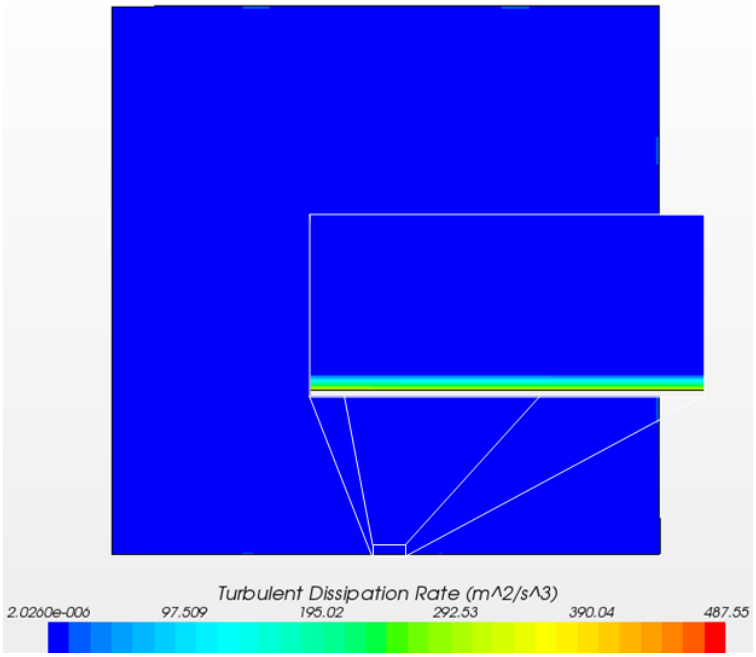

Fig. 3.21: Turbulent dissipation rate (ε) mapped onto the velocity inlet of the computational domain.

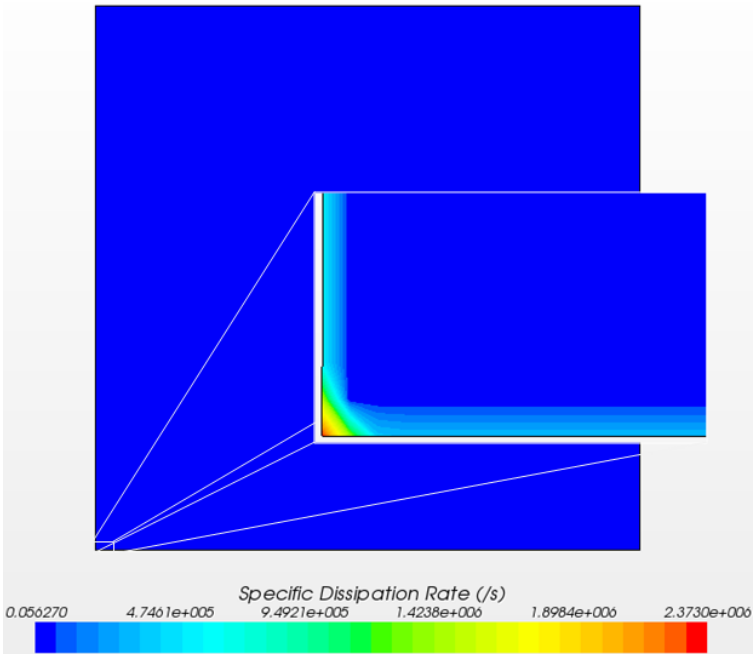

Fig. 3.22: Specific turbulent dissipation rate (ω) mapped onto the velocity inlet of the computational domain.

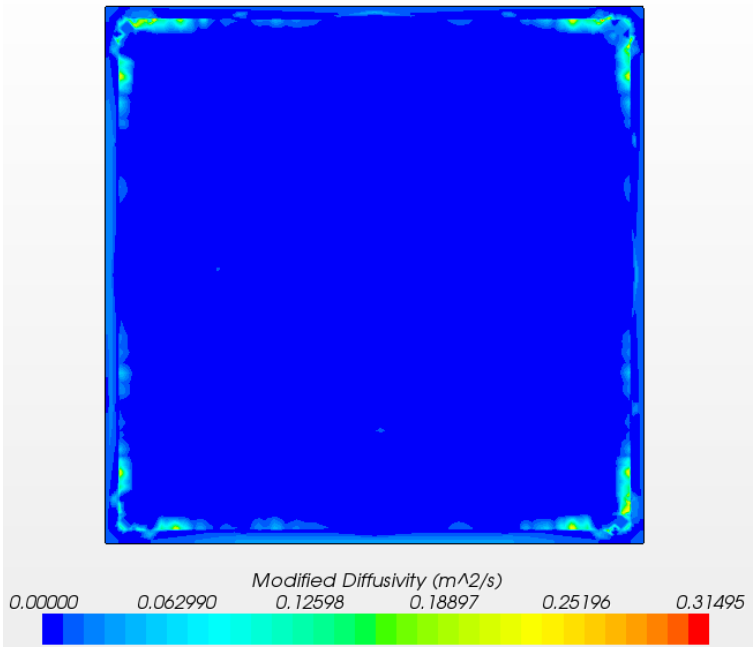

Fig. 3.23: Modified turbulent diffusivity ($\tilde{\nu}$) mapped onto the velocity inlet of the computational domain.

3.3.3 Pressure Outlet

The pressure outlet boundary represents a region allowing fluid to exit the computational domain to an environment with a known pressure. Similar to the velocity inlet boundary, the turbulence and thermal physics properties as well as the gauge pressure of the specified fluid outlet region. In order to simulate the fluid flow exiting to the ambient conditions of the RoBuT lab, the pressure was set to the reference pressure (zero gauge), the static temperature was set to the reference temperature and the turbulence intensity and viscosity ratio were set to $1.0E$-5 and 1.0, respectively. The reference pressure and temperature are listed in Table 3.4.

It is recognized that the specified zero gauge pressure is inaccurate, because the simulation pressure outlet plane coincides with the test section exit and not the wind tunnel exit, see Fig. 2.2. However, due to the incompressible nature of the flow, it is assumed that the pressure drop between the test section and wind tunnel exit planes is negligible.

3.3.4 Physics Reference Values

The physics reference values for each STAR-CCM+ simulation define the ambient environment of the physics being modeled. The values specified for each validation case are shown in Table 3.4.

At the time of each RoBuT experiment, the local absolute pressure, relative percent humidity and temperature of the air in the RoBuT lab were recorded. From the known

Table 3.4: Physics reference values used for each validation case.

Parameter	M1	F1	M2	F2
Air Density (kg/m^3)	1.013	1.015	1.026	1.019
Absolute Pressure (Pa)	86625.0	86765.3	87220.0	86529.0
Temperature (C)	23.4	23.4	22.4	22.1
Gravity	$[-9.81, 0, 0]$ m/s^2			
Altitude	1456.3 m			

altitude of Utah State University, 1456.3 m above sea level, and the recorded lab conditions the air densities shown above were calculated using the BARANIDESIGN air density calculator available at http://www.baranidesign.com/air-density/air-density.htm.

3.4 Initial Conditions

Prior to running each turbulence model simulation, the initial conditions or initial field data for every dependent variable in the governing equations was set across the computational domain. The initial conditions were set as: uniform zero gauge pressure, uniform static temperature as specified in the reference values and the inlet turbulence specification and velocity profiles were extended from the velocity inlet throughout the computational domain.

3.5 Convergence Criteria

Solution convergence for steady state simulations is achieved by iterating on the governing differential equations across the computational domain until the residuals reach an acceptable point determined by the user. Residuals represent the degree to which the discretized governing equations are satisfied collectively by each cell in the discretized mesh. The STAR-CCM+ simulations in this study monitor residuals at every iteration for continuity, energy, X, Y and Z momentum and for the turbulence transport equations, described in section 3.2.7. The American Society of Mechanical Engineers (ASME) set the threshold for iterative convergence as a decrease of the normalized residuals of three (preferably four) orders of magnitude for each equation solved [44].

Convergence criteria for this validation study maintains the convergence threshold set by ASME while requiring each turbulence model simulation to reach iterative convergence, denoted by a 'leveling out' of the normalized residuals. Fig. 3.24 illustrates a converged solution; examples of the converged residuals for each type of turbulence model are contained in Appendix E.

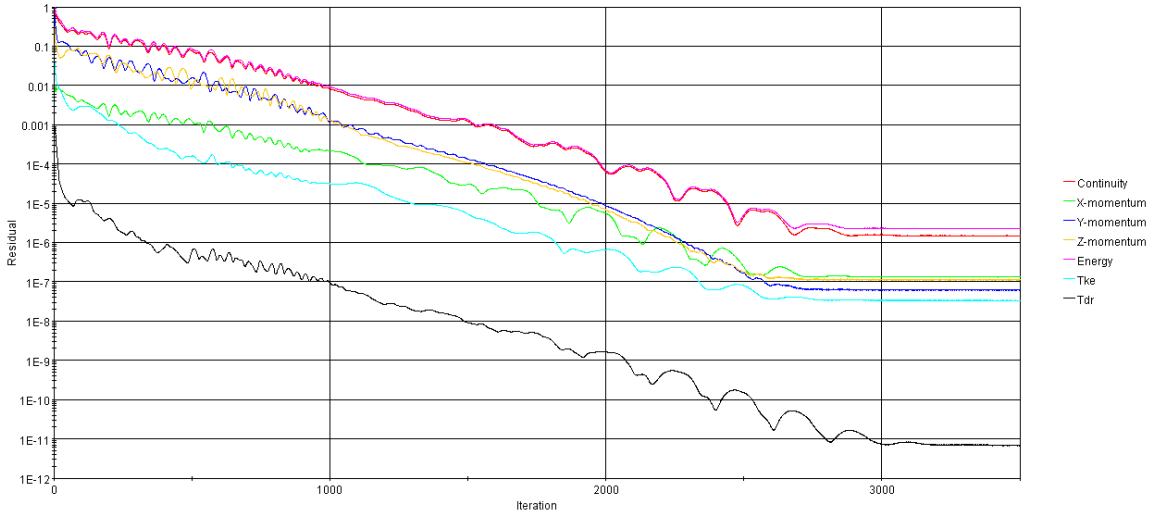

Fig. 3.24: Converged residuals of the F2 R2L simulation.

One exception was made to the convergence criteria for the SST turbulence model. The SST model solves an intermittency transport equation to mimic the behavior of algebraic engineering correlations for the source terms. STAR-CCM+ states that the intermittency equation is naturally noisy due to strong dependence of the source terms on higher powers of the mean flow strain rates, and the fact that the source terms are not differentiable functions [31]. The Fig. 3.25 illustrates a converged solution of the SST turbulence model.

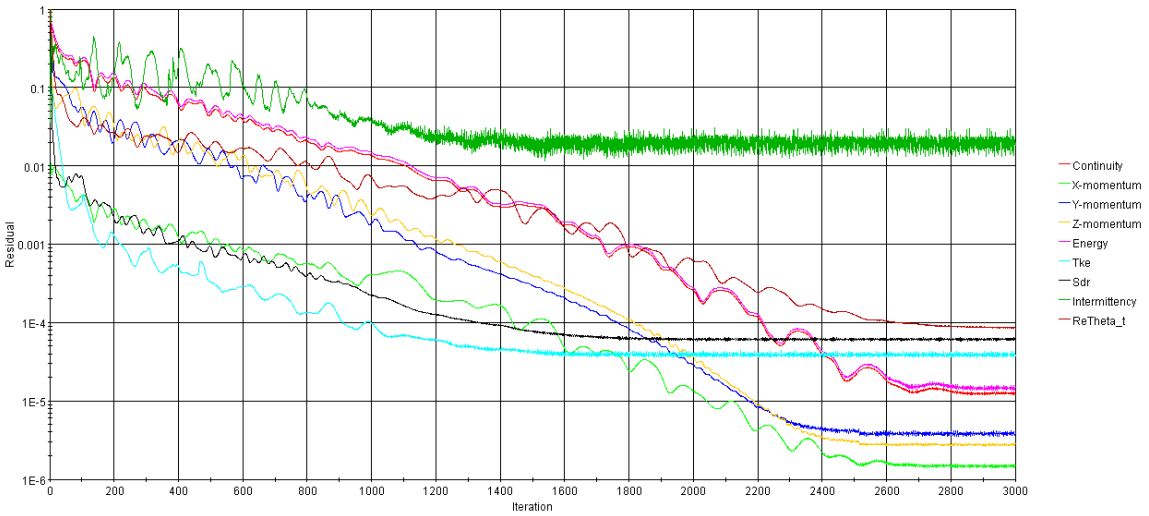

Fig. 3.25: Converged residuals of the M1 SST simulation.

Chapter 4

Validation Methodology

Prior to validation of a computer model, the computational code and solution must be verified [30]. Code verification establishes that the code accurately solves the mathematical models. STAR-CCM+ is recognized as an extensively verified CFD software package; therefore, it is assumed that the models employed in the solution of each simulation accurately solve their respective transport equations. Solution verification comprises the estimation of the simulation discretization error or numerical uncertainty; the GCI method was implemented to satisfy this verification as described in Section 3.1.4 with the results presented in Chapter 5.

Validation, as defined in the published ASME standard for verification and validation, is the process of determining the degree to which a model is an accurate representation of the real world from the perspective of the intended uses of the model [45]. The validation method implemented in this study was the mean comparison method developed by Oberkampf and Roy [30], which computes a statistical confidence interval, dependent on the uncertainty in the experimental data, which presents an estimated range within which the true modeling error lies and reflects the confidence in the estimated model accuracy.

The confidence interval for the true modeling error is derived from the confidence interval expression for the true experimental mean (μ^*) for the SRQ of interest, defined as

$$\bar{y}_e - t^*_{\alpha/2,\nu^*} \cdot \frac{s}{\sqrt{n}} < \mu^* < \bar{y}_e + t^*_{\alpha/2,\nu^*} \cdot \frac{s}{\sqrt{n}} \tag{4.1}$$

where s is sample standard deviation, based on n experiments, given by

$$s = \left[\frac{1}{n-1} \sum_{i=1}^{n} (y_e^i - \bar{y}_e)^2 \right]^{1/2}. \tag{4.2}$$

For the true modeling error, the estimated model error ($\tilde{E}$) and the true model error (E) are defined as

$$\tilde{E} = y_m - \bar{y}_e, \tag{4.3}$$

$$E = y_m - \mu^* \tag{4.4}$$

where y_m is the model SRQ and $\bar{y}_e$ is the estimated experimental SRQ, or sample mean based on n experiments. $\bar{y}_e$ is given by

$$\bar{y}_e = \frac{1}{n}\sum_{i=1}^{n} y_e^i \tag{4.5}$$

where y_e^i are the individually measured values of the SRQ from each each experiment.

By substituting the estimated model error and the true model error into Eq. 4.1 the expression changes from a bounded interval for μ^* to a bounded interval containing the true modeling error E:

$$y_m - \bar{y}_e - t^*_{\alpha/2,\nu^*} \cdot \frac{s}{\sqrt{n}} < E < y_m - \bar{y}_e + t^*_{\alpha/2,\nu^*} \cdot \frac{s}{\sqrt{n}} \tag{4.6}$$

$$\left(\tilde{E} - t^*_{\alpha/2,\nu^*} \cdot \frac{s}{\sqrt{n}},\ \tilde{E} + t^*_{\alpha/2,\nu^*} \cdot \frac{s}{\sqrt{n}}\right) \tag{4.7}$$

where t^* is the two-tail probability value from the student's t-distribution and the level of confidence is given by $100 \cdot (1-\alpha)\%$.

While the above expressions for the true modeling error are ideal for specific validation variables it is often desirable to investigate a global, or overall, statement of the modeling accuracy, which is more beneficial when considering a range of validation data. To obtain a measure for the global true modeling error the *average relative error* is considered, defined as

$$\left|\frac{\tilde{E}}{\bar{y}_e}\right|_{avg} = \frac{1}{x_u - x_l}\int_{x_l}^{x_u} \left|\frac{y_m(x) - \bar{y}_e(x)}{\bar{y}_e(x)}\right| \mathrm{d}x, \tag{4.8}$$

with the *average relative confidence indicator* as the half-width of the confidence interval, defined as

$$\left|\frac{CI}{\bar{y}_e}\right|_{avg} = \frac{t_{\alpha/2,\nu}}{(x_u - x_l)\sqrt{n}} \int_{x_l}^{x_u} \left|\frac{s(x)}{\bar{y}_e(x)}\right| \mathrm{d}x. \tag{4.9}$$

where x_u and x_l are the dependent spacial extrema in the $y_m(x)$ and $\bar{y}_e(x)$ profiles of interest. $\left|\frac{CI}{\bar{y}_e}\right|_{avg}$ is referred to as an indicator, as opposed to an interval, because the uncertainty structure of $s(x)$ is not maintained through the integration operator.

For this validation study, the confidence interval calculations above were modified to account for bias errors in the experiment instrumentation as well as the precision uncertainty. The bias and precision errors for each validation case, obtained from a single experiment, were obtained for the u velcoity and heat flux from the RoBuT experiments and data post processing. For the u velocity, the bias, random and 95% precision uncertainty was calculated during the PIV post processing as discussed in Chapter 2. For the heat flux, the manufacturer prescribed bias uncertainty of 2% of the sensor reading was used along with the heat flux measurements at each HFS location from the RoBuT experiments.

The overall uncertainty, including bias and precision, produced by the PIV uncertainty estimator were used directly in the modified confidence interval calculations to be described below. The overall heat flux uncertainty was calculated as

$$U = \sqrt{B^2 + \left(t^*_{\alpha/2,\nu^*} \cdot \frac{s}{\sqrt{n}}\right)^2}. \tag{4.10}$$

where B is the bias uncertainty.

Replacing $t^*_{\alpha/2,\nu^*} \cdot \frac{s}{\sqrt{n}}$ in Eqs. 4.7 and 4.9 with U defined above, the modified true modeling error confidence interval and indicator used in this study are defined as

$$\left(\frac{\tilde{E} - U}{\bar{y}_e}, \frac{\tilde{E} + U}{\bar{y}_e}\right) \tag{4.11}$$

and

$$\left|\frac{\tilde{E}}{\bar{y}_e}\right|_{avg} = \frac{1}{x_u - x_l} \int_{x_l}^{x_u} \left|\frac{y_m(x) - \bar{y}_e(x)}{\bar{y}_e(x)}\right| \mathrm{d}x \tag{4.12}$$

with

$$\left|\frac{CI}{\bar{y}_e}\right|_{avg} = \frac{1}{(x_u - x_l)} \int_{x_l}^{x_u} \left|\frac{U(x)}{\bar{y}_e(x)}\right| \mathrm{d}x. \tag{4.13}$$

Note that the specific confidence interval, Eq. 4.11, was normalized by $\bar{y}_e$ similar to Eqs. 4.12 and 4.13, which will simplify comparisons between the heat flux and u velocity errors in the turbulence model assessment, because the results of both will be relative to the experimental data.

The amount of experimental data obtained for the validation SRQs varied between between each experiment. The u velocity SRQ profiles were obtained from a time average of 1000 frames of PIV data, thus with $n = 1000$ the normal distribution (z^*) was used instead of the student's t-distribution. For the heat flux SRQs, multiple measurements were obtained for the M1 and F1 cases whereas only one measurement was recorded for the M2 and F2 cases.

Each confidence interval reported in the validation results, except the M2 and F2 heat flux, was calculated at a 95% confidence level. Thus, $z^* = 1.96$ was used for the u velocity, $t^*_{\alpha/2,\nu^*} = 2.201$ ($n = 12, \nu^* = 11$) was used for the M1 heat flux and $t^*_{\alpha/2,\nu^*} = 3.182$ ($n = 4, \nu^* = 3$) was used for the F1 heat flux. The heat flux readings and statistical calculations for the experimental SRQs are shown in Appendix F.

It is recognized that the confidence interval calculations in this validation study do not account for the influence of discretization error. As discussed in Section 3.1.3, all of the turbulence models for a given case study were solved over the same set of discretized meshes, which allowed for some models to retain discretization error that is not negligible. Therefore, the results of the GCI study are included in the concluding assessment of the turbulence model validation results.

Chapter 5

Results

The CFD simulations for the four validation cases and the respective turbulence model validations were carried out as described in Chapters 3 and 4. Prior to presenting the validation assessment results, the effects of buoyancy on fluid flow are reviewed, focusing on the modification to the shear stress distribution as shown in Fig. 5.1, and the flow fields generated by the turbulence model simulations are studied, including visualizations of the general fluid flow and local profiles of the streamwise u velocity, Reynolds turbulent shear stress and heat flux at the three heat flux sensor (HFS) locations. The general fluid flow visualizations, Figs. 5.2 and 5.3, are included to give a general perspective of the flow and heat transfer effects. The local profile visualizations, including the experimental profiles, are shown in Figs. 5.4–5.9 and will be discussed accordingly. An overall ranking of the turbulence models from the validation assessment results is shown in Table 5.1. The specific turbulence model validation results for each case are shown in Tables 5.2–5.5. Additionally, Figs. 5.10–5.11 illustrate the tabulated results. Following the discussion of the validation assessments, the grid convergence study results are presented and discussed. The results of all three HFS locations are included in the following discussions; however, for brevity, only the validation and GCI result tables and figures for the third HFS location are shown in this chapter. The tables and figures for the other HFS locations are contained in Appendix C and D.

5.1 Review of Buoyancy Effects

As discussed in Chapter 1, the structural and external effects of buoyancy consist of the direct influence of buoyancy on the turbulence field, diffusion and advection, and that on the mean field, respectively. The structural and external effects can either enhance the

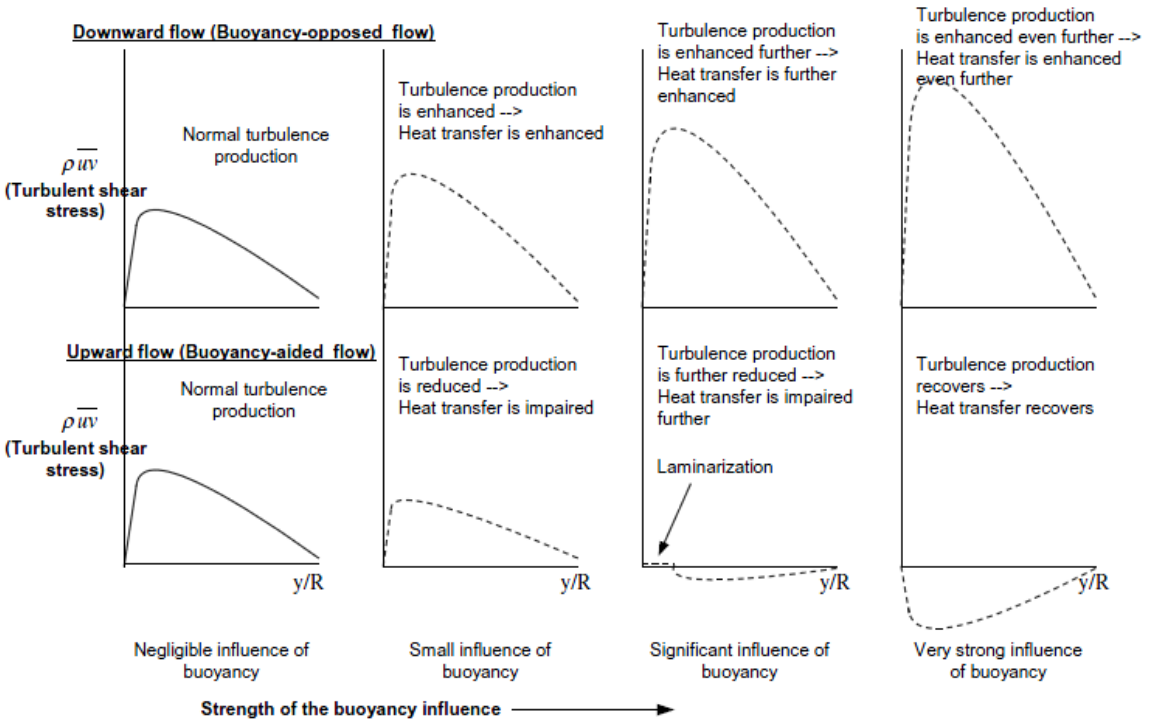

Fig. 5.1: Turbulence shear stress for buoyancy-opposed and buoyancy-aided flow[1].

heat transfer occuring in the flow or impair it depending on the flow rate, thermal loading and the flow direction [23].

For downward flow, buoyancy opposes the flow and the near-wall velocity is reduced, which reduces the energy transport by advection, a further consequence is the increase of shear stress in the region. As a result, the turbulence production is enhanced and the turbulent diffusion of heat transfer is improved [18], see Fig. 5.1. In buoyancy-aided flow, although advection is increased in the near-wall region due to buoyancy, shear stress is reduced as shown in Fig. 5.1. The net result is that the heat transfer process is impaired. As the buoyancy influence increases, due to the deterioration of turbulence production, a stage is reached where the shear stress in the near-wall region falls to a level such that the flow is effectively laminar (see Fig. 5.1). With further increase of buoyancy, the shear stress in the core region becomes negative and turbulence production and heat transfer

[1]Reprinted from The Lancet, 51, Kim, W. S., He, S., and Jackson, J. D., "Assessment by Comparison with DNS Data of Turbulence Models used in Simulations of Mixed Convection," pp. 1293–1312, 2008, with permission from Elsevier.

effectiveness recover [18].

In this study, it was expected that buoyancy effects would be minor in the forced convection flows as their mixed convection ratios are at the lower end of the mixed convection range, see Table 2.1. For the mixed convection flows, significant buoyancy influence was expected.

5.2 Visualization of the Results

Select distributions of the general fluid flow computed by the CFD simulations for each validation case are shown in Figs. 5.2 and 5.3. Fig. 5.2 illustrates the temperature and pressure typical of all of the validation cases and Fig. 5.3 illustrates the fluid velocity predicted down the centerline of the test section for each case. Note that the inlet and heated plate are at the left and bottom of each illustration. These figures are included to give a global reference for the specific HFS profiles to be discussed.

In Fig. 5.3, the normalized velocity distributions (u/U_b) shown from top to bottom

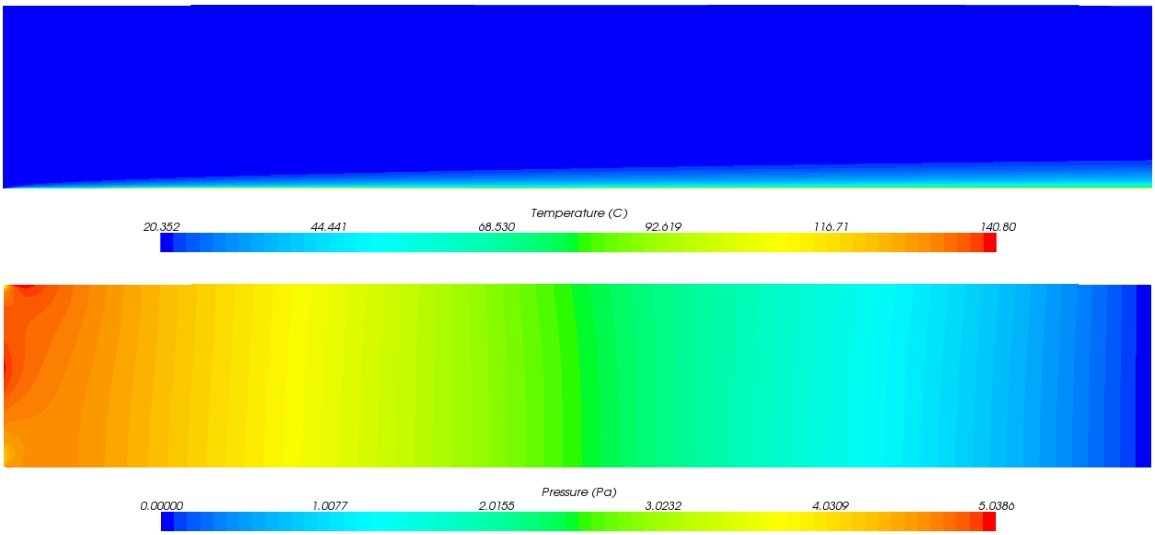

Fig. 5.2: General distributions of the temperature (Top) and pressure (Bottom) down the simulation centerline. Note that the inlet and heated plate are at the left and bottom of each figure.

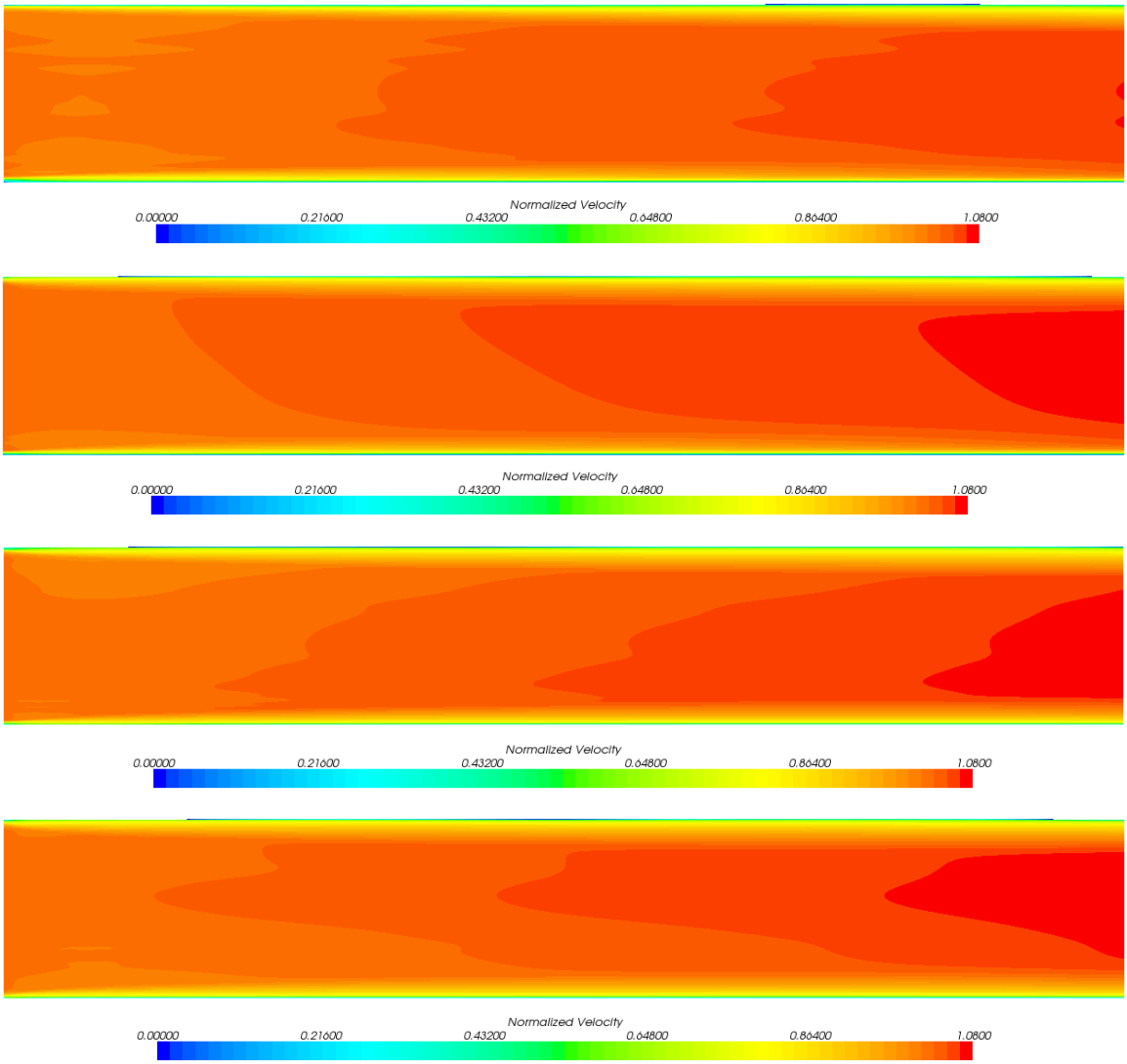

Fig. 5.3: Normalized distributions (u/U_b) of the fluid velocity for the M1 (Top), M2 (Top-Middle), F1 (Bottom-Middle) and F2 (Bottom) validation cases down the simulation centerline. Note that the inlet and heated plate are at the left and bottom of each figure.

are M1, M2, F1 and F2; where U_b is the bulk velocity at the inlet. No significant effects of buoyancy are apparent in the M1 flow, though the flow rate is similar to the M2 case where the flow outside the heated plate boundary layer is significantly lower than that at the top of the test section. In the F1 case, the flow adjacent to the heated plate exhibits an increase in the fluid velocity that is presumed to be due to minor buoyancy influence.

Conversely, the F2 fluid velocity distribution indicates that the boundary layer on the top, unheated wall is developing much faster than that on the heated plate, while buoyancy influence is suspected it is unreasonable that the influence is significant due to the large flow rate present. However, a more complicated buoyancy effect may be occurring in this case due to the thermal condition of the plate. This may also be why the M1 and M2 velocity distributions are different.

The pressure distribution illustrated in Fig. 5.2 shows the pressure drop across the test section, which was predicted in the range of 5 Pa by every turbulence model for all four validation cases. This small pressure drop gives credence to the assumption that the flow is incompressible and use of the compressible ideal gas model was not needed; however, the change in pressure may have enhanced the calculation of the buoyancy influence in the flow. The temperature distribution seems to indicate that the thermal boundary layer is fully developed at the later end of the test section. In conjunction with the velocity distributions in Fig. 5.3, it is reasonable that the flow is nearly fully developed at the later end of the test section for all four validation cases.

Figs. 5.4 and 5.5 illustrate the streamwise u velocity and Reynold's turbulent shear stress $u'v'$ profiles from the SLR, V2F and RST simulations as well as the experimental profile with 95% uncertainty bands for the M1 and F1 validation cases. Similarly, Figs. 5.6 and 5.7 illustrate the same profiles for the M2 and F2 validation cases. The discretization error for the CFD predicted profiles was not included in the figures, because it was generally found to be less than 1.0%. The discretization error and results of the GCI grid refinement study are discussed in the next section.

The illustrated experimental flow profiles for the forced convection cases exhibit a degradation of the fully turbulent velocity along the test section, which is indicated by the smoothing of the sharp transition from the near-wall to freestream flow from the first to third HFS in Figs. 5.4 and 5.6 (dashed lines). This degrading trend is ratified by the apparent increase in buoyancy influence along the test section in Figs. 5.5 and 5.7, denoted by the decrease in the turbulent shear stress peak value near the wall, reference Fig. 5.1.

The CFD predicted u velocity from the turbulence models is in good agreement with the experimental values at each of the three HFS locations for both of the heated plate boundary conditions, with significant divergence generally only occurring away from the wall. The predicted turbulent shear stress agrees fairly well with the experimental values, except for the first HFS location. A possible cause of the more significant discrepancies between the experimental and CFD results at the first HFS may be the developing thermal boundary layer in the flow at that location, as illustrated in the temperature distribution shown above and the heat flux plots in Figs. 5.8 and 5.9.

The experimental flow profiles for the mixed convection cases, solid lines in Figs. 5.4 and 5.6, exhibit a flow profile which is assumed to be in transition, between laminar and turbulent flow, from the first to third HFS locations. This assumption is in agreement with the significant buoyancy influence shown in the corresponding turbulence shear stress profiles (Figs. 5.5 and 5.7), where laminarization of the flow is apparent from the zero gradient near the wall at the second and third HFS locations (reference Fig. 5.1). The CFD predicted velocity is only in good agreement with the experiment in the near-wall region, diverging in the freestream flow. Furthermore, it appears that the CFD models predict the fluid flow to be more turbulent than the experiment, distinguishable by the larger velocity gradient near the wall and the sharper transition into the freestream flow, which is also consistent with the over prediction of the near-wall shear stress peak in Figs. 5.5 and 5.7. This over prediction of turbulence is reasonable, because the boundary layer flow may actually be in transition as mentioned earlier and the CFD turbulence models used are formulated for fully turbulent flow. Despite this fact, the CFD predicted turbulent shear stress at the second and third HFS locations is in good agreement with the experimental values, particularly for the SLR turbulence model. The large discrepancies seen in both the u velocity and turbulent shear stress profiles at the first HFS location are likely due to a combination of the developing thermal boundary layer mentioned previously and the inherent errors of simulating transitional flow with a turbulence model.

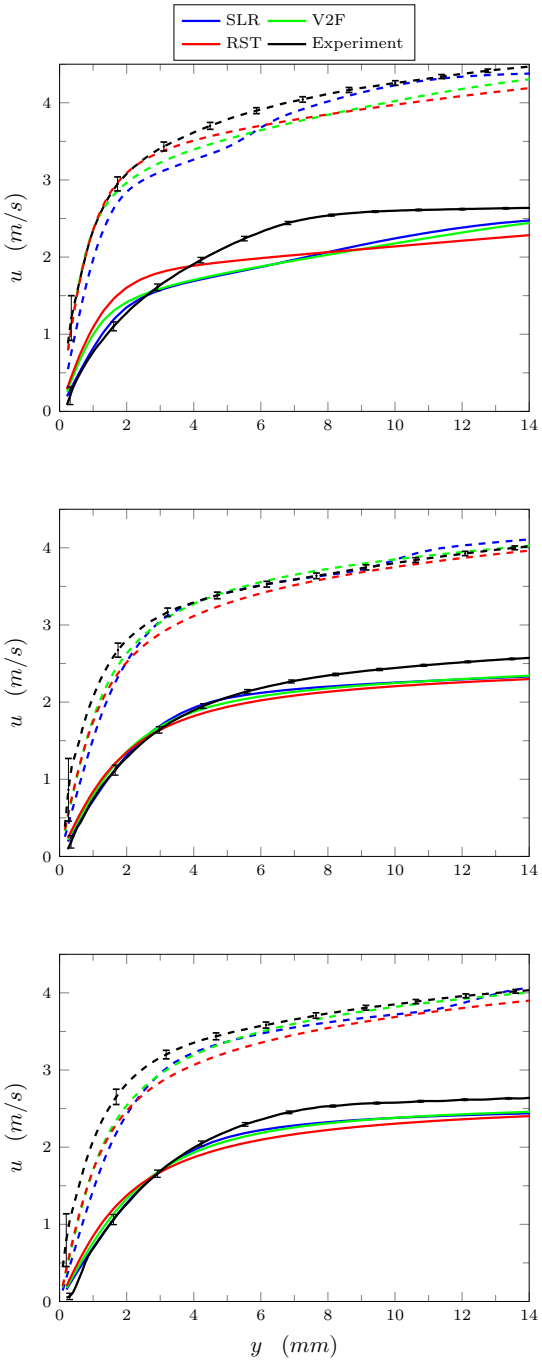

Fig. 5.4: Streamwise velocity u for the F1 (dashed) and M1 (solid) validation cases at the three HFS locations: $x = 16$ cm (top), $x = 77$ cm (middle), $x = 139$ cm (bottom).

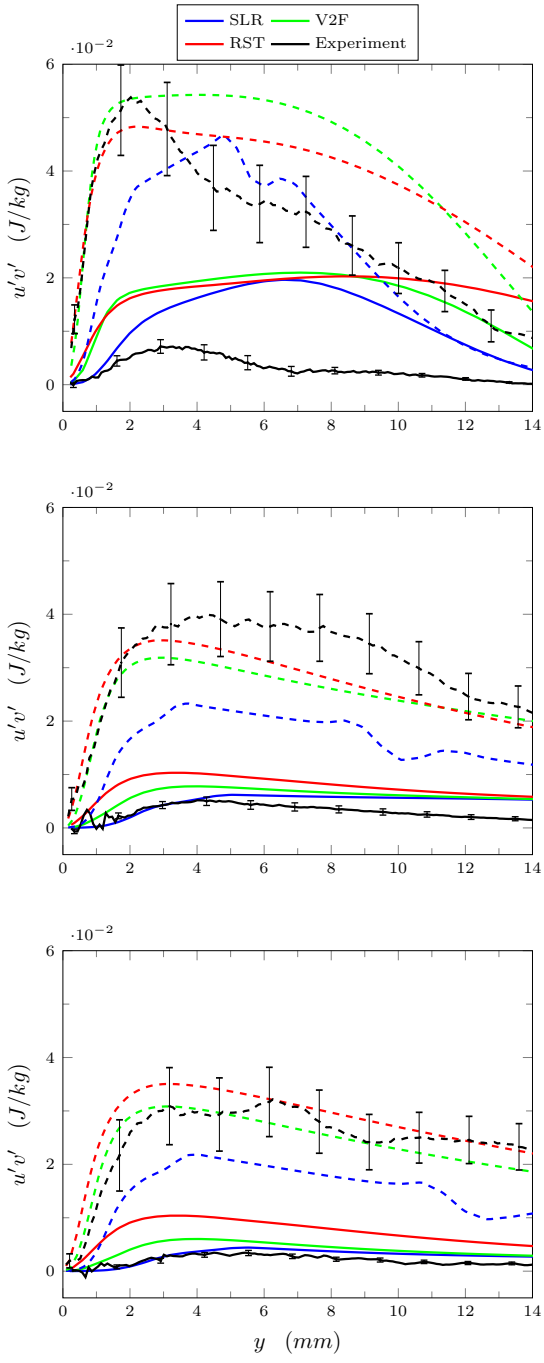

Fig. 5.5: Reynold's stress $u'v'$ for the F1 (dashed) and M1 (solid) validation cases at the three HFS locations: $x = 16$ cm (top), $x = 77$ cm (middle), $x = 139$ cm (bottom).

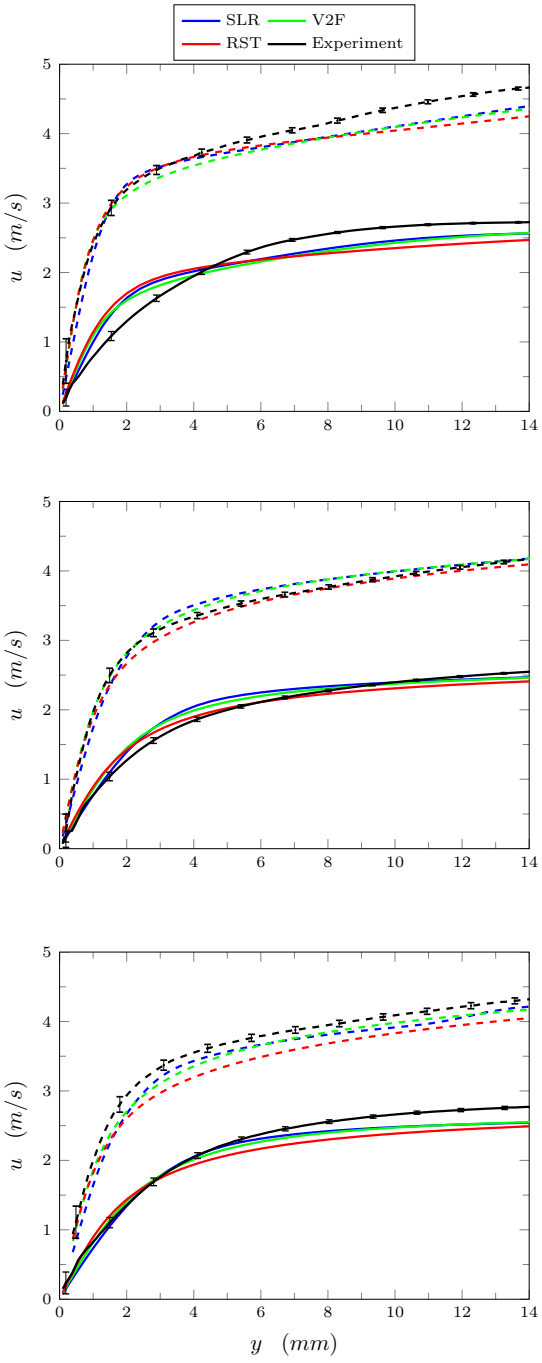

Fig. 5.6: Streamwise velocity u for the F2 (dashed) and M2 (solid) validation cases at the three HFS locations: $x = 16$ cm (top), $x = 77$ cm (middle), $x = 139$ cm (bottom).

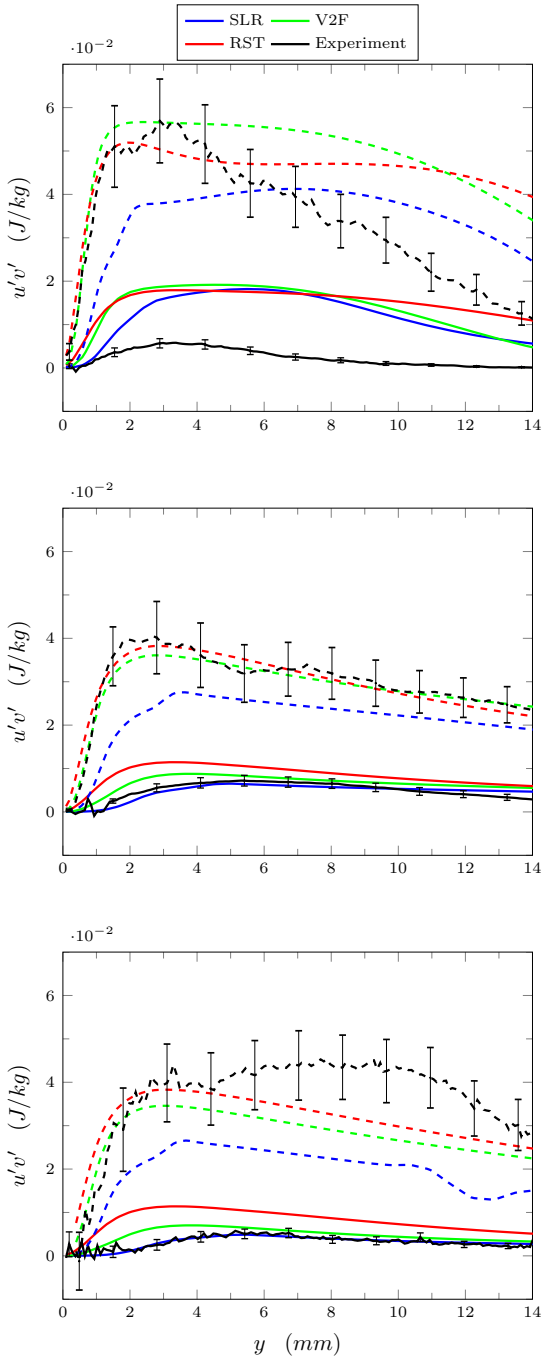

Fig. 5.7: Reynold's stress $u'v'$ for the F2 (dashed) and M2 (solid) validation cases at the three HFS locations: $x = 16$ cm (top), $x = 77$ cm (middle), $x = 139$ cm (bottom).

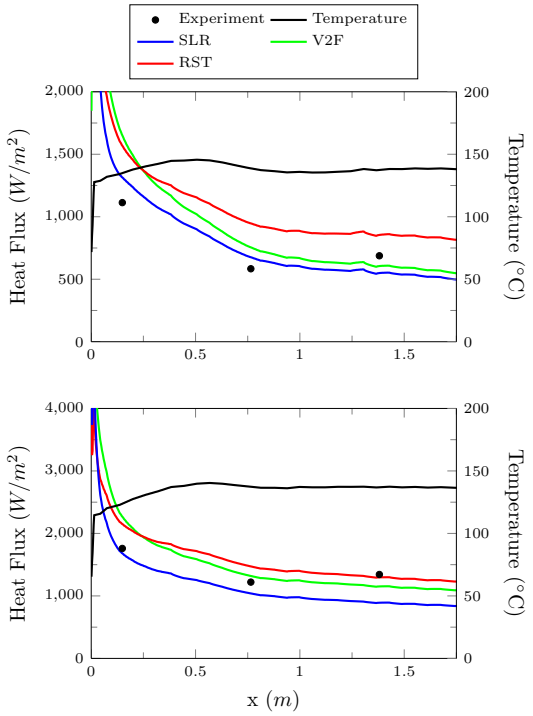

Fig. 5.8: Heat flux along the centerline of the heated plate ($z = 0$) for M1 (top) and F1 (bottom) validation cases.

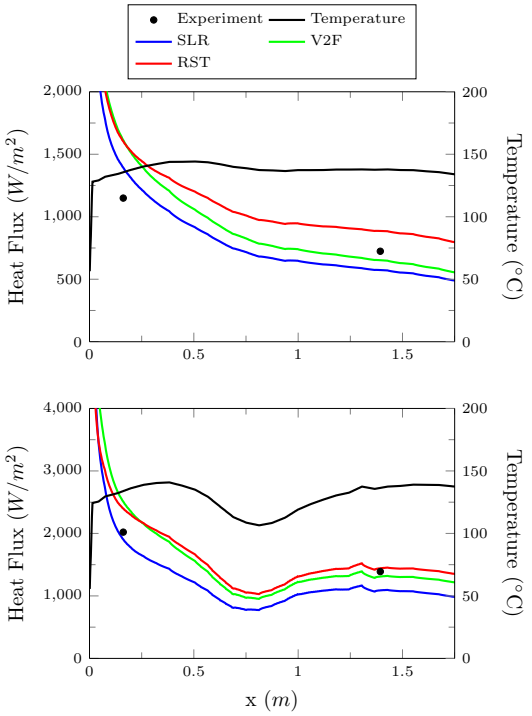

Fig. 5.9: Heat flux along the centerline of the heated plate ($z = 0$) for M2 (top) and F2 (bottom) validation cases.

The CFD simulated wall heat flux down the centerline of the heated plate and the experimental heat flux measured at the three HFS locations for each validation case is illustrated in Figs. 5.8 and 5.9, along with the wall surface temperature following the right-hand y axis. Varying degrees of agreement are present between the CFD and experimental results. In every case, the SLR turbulence model appears to give the best results over the region were the thermal boundary layer is developing, the first and second HFS, but is less accurate as the flow develops. In the thermally developed region of HFS three, the V2F, $k - \omega$ and SST models show better agreement.

A likely cause for the discrepancy between the experiment and the mixed convection cases at the first HFS was mentioned above. It is reasonable that the over prediction of turbulence, resulting from the turbulence model solution of the transitional flow, would

cause the CFD simulation to also over predict the heat flux due to the larger near-wall velocity gradient, see the first HFS velocity profiles in Figs. 5.4 and 5.6.

Also worth noting is the smooth temperature curve shown for the M2 case in Fig. 5.9. The slower fluid velocity allowed the heat in the plate to be conducted axially rather than being convected away, as is evident in the F2 case illustrated in the same figure. Thus, the consistency of the boundary conditions and results for the M1 and M2 cases is reasonable.

5.3 Validation Results

The turbulence model error validation studies for the streamwise u velocity and heat flux SRQs at the three HFS locations were performed as described in Chapter 4. An overall ranking of the CFD turbulence models with respect to mixed and forced convection flow was computed from the validation study results. The model rankings are shown in Table 5.1 and are discussed accordingly.

The global validation of the near-wall u velocity was performed for two selections of the available PIV data; first, all of the available data at each HFS location, referred to as FULL in the tables and figures hereafter, and second, data assumed to be in the viscous sub-layer and buffer regions of the turbulent boundary layer at each location (the 6^{th} to 17^{th} data points), referred to as VSL hereafter. The VSL assessment was included because it was assumed that the turbulence models able to better predict the fluid flow in the viscous sub-layer would be more suited to accurately predicting the wall heat flux. Table 5.2 contains the relative error results, $\frac{\tilde{E}}{\bar{y}_e}$ and $\left|\frac{\tilde{E}}{\bar{y}_e}\right|_{avg}$, from the heat flux and u velocity validation assessments with an overlaid gray-scale for comparison and evaluation of the average turbulence model performance. Tables 5.3 and 5.4 contain the average relative error with 95% confidence indicator for the FULL and VSL assessments specific to the third HFS. Additionally, for further insight into the local character of the u velocity error, the maximum relative error with its respective 95% confidence indicator are listed alongside the average relative error for each model and validation case. The maximum relative error and confidence indicator

are defined as

$$\left|\frac{\tilde{E}}{\bar{y}_e}\right|_{max} = max\left|\frac{y_m(x) - \bar{y}_e(x)}{\bar{y}_e(x)}\right| \tag{5.1}$$

and

$$\left|\frac{CI}{\bar{y}_e}\right|_{max} = \left|\frac{U(\hat{x})}{\bar{y}_e(\hat{x})}\right|, \tag{5.2}$$

where $\hat{x}$ is the x value in the range $x_l \leq x \leq x_u$ at which the maximum value of $\left|\frac{\tilde{E}}{\bar{y}_e}\right|$ occurs.

The heat flux validation was carried out for each specific HFS location using Eq. 4.11 and the results of the assessment, alongside the CFD predicted and experimentally measured heat flux, for the third HFS are shown in Table 5.5.

5.3.1 General Results

The results are discussed in this section with a global perspective, drawn from the average relative error results of the validation assessments contained in Table 5.2. Therefore it must be noted that there are significant differences between the local and global character of the CFD turbulence model and the experimental u velocity profiles, which are indicated by the discrepancies between the average and maximum relative error. Figs. 5.11 and 5.12 show that the largest error in the CFD predicted u velocity is in the viscous sub-layer region; it is also shown that the local divergence in the character of the turbulence models is more pronounced for the mixed convection cases.

From Table 5.2, it is apparent that there is not a single turbulence model that gives superior performance in predicting the heat flux and fluid flow for both the mixed and forced convection cases. For mixed convection however, the SLR model gave the best results in almost every instance. Furthermore, the SLR model predicted the heat flux in the developing thermal boundary layer for both forced and mixed convection much better than any of the other models. Thus, the SLR model can be recommended for CFD simulation of mixed convection and developing thermal boundary layers.

It is difficult to define conclusive results for forced convection flow overall. As shown in Table 5.2, for the more ideal thermal condition in the F1 case, the SA model clearly

predicts the u velocity with much better accuracy than any of the other models throughout the test section; however, it only gives good predictions for the heat flux when the flow is fully developed thermally. In contrast, for the F2 case, many of the turbulence models were in excellent agreement with experimental values for the fluid flow and the third HFS heat flux. The $k-\omega$ model giving the best results for the FULL, VSL and heat flux validation assessments at the third HFS location.

In an attempt to identify the turbulence model most suited to predicting the mixed and forced convection flows, the root mean square of the relative errors for each validation assessment and turbulence model was evaluated. The resulting ranking of the turbulence models is shown in Table 5.1.

The ranking of the turbulence models with respect to mixed convection agrees with the conclusions deduced from the results in Table 5.2. For forced convection, the consistent high ranking of the $k-\omega$ model brings further insight to results discussed. Though the

Table 5.1: Ranking of turbulence models with respect to the the available error data.

	Mixed			Forced		
	Velocity			Velocity		
Rank	FULL[1]	VSL[2]	Heat Flux	FULL[1]	VSL[2]	Heat Flux
1	SLR	SLR	SLR	$k-\omega$	R2L	$k-\omega$
2	SST	SST	$k-\omega$	V2F	$k-\omega$	SST
3	V2F	V2F	SST	SST	R2LB	S2L
4	$k-\omega$	$k-\omega$	SA	SA	V2F	R2L
5	S2L	RST	R2L	SLR	S2L	SLR
6	RST	S2L	V2F	R2L	SA	RST
7	SA	R2L	S2L	RST	RST	SA
8	R2L	SA	RST	S2L	SST	V2F
9	S2LB	S2LB	S2LB	R2LB	RSTB	S2LB
10	R2LB	RSTB	R2LB	RSTB	SLR	R2LB
11	RSTB	R2LB	RSTB	S2LB	S2LB	RSTB

[1] FULL profile ranking was computed using all of the available PIV data at each location.

[2] VSL, viscous sub-layer, ranking was computed using PIV data only in the VSL and buffer regions of the boundary layer at each location.

$k-\omega$ model did not give the best results in every situation, it gave consistent rather than varying results in the heat flux valdiation across the three HFS locations. Therefore, it may be recommended that the $k-\omega$ turbulence model be used in CFD simulations of forced convection flow; recognizing that the results may not be the most accurate at every location, but the modeling error is more consistent.

From Fig. 5.10, it is apparent that as the flow develops the heat flux predicted by the turbulence models tends to be in better agreement with the experimental values. The V2F and $k-\omega$ models giving the best and most consistent results when all four validation cases are considered. This conclusion is in agreement with results found in the literature, where it was concluded that the V2F model gave the best results [21, 22].

In every validation case, the two-layer turbulence models that employed the buoyancy driven solver performed very poorly in predicting both the streamwise u velocity and the wall heat flux, giving the worst results in almost every instance of the three validation assessments. As illustrated by the error plots in Figs. 5.11 and 5.12, the near wall u velocity was greatly over predicted and the freestream velocity followed the trend of the experiment but the magnitude was severely under predicted. Performance was better for the forced convection cases than the mixed, giving values of $\left|\frac{\tilde{E}}{\bar{y}_e}\right|_{avg}$ in the range of $10-25\%$ and $5-25\%$ for the FULL and VSL, respectively; while for the mixed convection cases, values of $\left|\frac{\tilde{E}}{\bar{y}_e}\right|_{avg}$ were in the range of $20-35\%$ and $25-75\%$ for the FULL and VSL. The significant over prediction of the near-wall flow is suspected to have led to the over predicted heat flux illustrated in Fig. 5.10 and denoted by the $\frac{\tilde{E}}{\bar{y}_e}$ values in the range of $20-135\%$ and $110-230\%$ for the forced and mixed convection cases, respectively.

The buoyancy driven two-layer solver seems ill-suited to solving mixed and forced convection flows, though significant buoyancy influence is apparent in the turbulent shear stress profiles in Figs. 5.5 and 5.7. It is reasonable that the buoyancy solver may give better results for natural convection or buoyant plume situations were the fluid flow is purely driven by buoyancy forces. Therefore, the results of the two-layer turbulence models that employed the buoyancy driven solver are neglected in the discussions that follow.

Table 5.2: Comparison table of the relative error results, without uncertainty bands, of the heat flux, VSL and FULL validation assessments. The results contained in the bold border cells are the best results for the given HFS location and validation case.

Heat Flux

	M1			M2			F1			F2		
Model	1	2	3	1	2	3	1	2	3	1	2	3
R2L	30.9	65.6	28.7	35.8		27.5	17.3	19.3	-4.4	14.3		4.1
S2L	26.5	72.3	35.0	35.4		34.8	12.1	11.1	-14.6	16.4		-3.9
SLR	18.1	16.0	-20.0	21.2		-20.7	-4.3	-14.8	-33.6	-5.3		-22.0
V2F	48.5	29.6	-11.8	40.2		-9.8	29.2	8.2	-14.1	24.5		-5.5
$k-\omega$	26.6	42.8	10.7	31.0		14.1	11.4	14.0	-8.3	11.3		1.5
SST	34.1	22.8	-18.4	30.9		-14.4	11.1	0.6	-23.9	13.1		-3.1
RST	40.9	62.4	24.4	39.5		22.6	22.3	20.8	-3.2	18.9		4.3
SA	29.4	59.1	20.6	32.1		33.5	15.5	24.6	3.1	19.4		18.1
R2LB	162.4	229.0	142.5	173.1		138.3	132.4	123.1	76.8	122.6		92.4
S2LB	115.5	166.6	109.0	130.0		108.7	95.0	60.0	21.2	120.0		36.0
RSTB	172.9	234.6	151.1	174.7		145.8	136.7	132.9	86.1	126.9		99.9

VSL

	M1			M2			F1			F2		
Model	1	2	3	1	2	3	1	2	3	1	2	3
R2L	24.1	23.8	40.7	42.9	30.8	23.0	1.7	7.7	10.9	0.7	4.7	3.7
S2L	11.4	27.1	43.9	37.4	34.8	26.3	10.4	12.7	17.3	0.7	5.3	9.3
SLR	8.0	1.7	2.6	28.8	4.2	11.7	13.3	22.5	28.3	6.1	10.9	15.0
V2F	27.5	7.7	12.2	38.6	12.4	4.9	1.8	12.2	17.3	2.0	1.5	8.5
$k-\omega$	21.5	14.5	29.6	43.0	23.5	15.1	2.0	7.1	11.1	2.7	7.4	2.1
SST	23.9	3.5	6.0	36.9	8.7	6.0	6.9	15.7	22.0	0.8	1.8	7.2
RST	41.8	12.1	23.1	45.9	16.4	7.9	0.7	15.1	18.1	2.3	4.6	11.3
SA	30.8	23.5	36.2	44.6	36.9	26.8	1.7	1.6	2.5	10.1	22.0	10.1
R2LB	51.7	53.5	75.8	72.2	64.0	54.5	5.3	7.0	7.4	6.8	12.9	7.9
S2LB	24.4	37.4	61.4	48.4	49.7	43.6	16.8	23.2	25.5	6.8	13.2	24.5
RSTB	58.6	49.7	72.4	70.8	61.7	52.3	9.2	12.2	12.3	9.7	14.4	12.7

FULL

	M1			M2			F1			F2		
Model	1	2	3	1	2	3	1	2	3	1	2	3
R2L	15.8	11.8	19.4	12.6	8.6	11.0	4.9	3.9	7.2	4.6	3.6	7.1
S2L	13.0	11.5	19.2	10.3	9.0	10.6	5.1	5.6	9.0	4.4	3.5	9.4
SLR	12.6	6.1	9.5	9.3	5.0	6.1	5.6	4.3	6.4	5.3	3.7	5.0
V2F	16.4	7.4	11.5	10.5	5.2	6.0	5.1	2.7	4.5	5.2	3.2	4.3
$k-\omega$	15.7	9.5	16.3	12.7	6.7	8.7	5.0	2.0	4.6	5.0	4.1	3.3
SST	15.8	7.3	10.7	11.5	4.7	6.7	5.7	3.0	5.1	4.7	2.4	5.0
RST	18.9	9.6	15.9	13.7	5.4	8.5	4.9	4.3	7.3	5.2	3.4	7.8
SA	15.8	10.5	17.6	13.2	9.3	10.5	4.9	1.4	3.7	4.0	7.2	3.6
R2LB	24.1	21.6	33.5	19.5	17.5	19.7	9.7	11.4	12.8	9.9	15.4	15.6
S2LB	19.9	20.7	33.3	14.1	15.8	20.7	9.2	14.3	18.4	9.7	18.7	22.8
RSTB	26.5	23.0	35.4	20.6	18.4	20.9	11.3	13.5	14.8	12.3	18.2	17.7

< 5%	5-10%	10-15%	15-20%	20-30%	>30%

5.3.2 Case Results

5.3.2.1 1^{st} Mixed Case

The u velocity relative error shown in Tables 5.3 and 5.4 depict the pattern of the turbulence model agreement results as shown in Fig. 5.11. At all three HFS locations the SLR turbulence model gave the best results, giving excellent results at the second and third HFS for the VSL in the range of $\left|\frac{\tilde{E}}{\bar{y}_e}\right|_{avg} < 3\%$ and 9.5% for FULL. Good results were also given by the SST and V2F models at the second and third HFS, giving $\left|\frac{\tilde{E}}{\bar{y}_e}\right|_{avg} < 13\%$ for the VSL and FULL assessments.

The SLR model also gave the best wall heat flux results at the first and second HFS, giving $\frac{\tilde{E}}{\bar{y}_e} \approx 18\%$ at both locations. While the $k-\omega$ model gave the best results at the third HFS with $\frac{\tilde{E}}{\bar{y}_e} = 10.7\%$ as shown in Table 5.5. The V2F model also gave good results at the third HFS, giving $\frac{\tilde{E}}{\bar{y}_e} = -11.8\%$.

It is interesting to note from general inspection of the relative error results that good agreement for the u velocity does not imply good agreement for the heat flux, and vice versa, as demonstrated by the SLR and $k-\omega$ models at the third HFS location where the $k-\omega$ model gave $\left|\frac{\tilde{E}}{\bar{y}_e}\right|_{avg} \approx 30\%$ and $\approx 16\%$ for the VSL and FULL, respectively.

5.3.2.2 1^{st} Forced Case

The FULL assessment results show that good agreement with the experimental u velocity is found by all of the turbulence models at all three HFS locations, giving results in the range of $\left|\frac{\tilde{E}}{\bar{y}_e}\right|_{avg} \approx 5\%$. Fig. 5.11 reveals however, that large errors are present in the near-wall u velocity predicted by most of the models, which is also indicated by the VSL relative error results. The SA model gave the best results at the second and third HFS locations, giving excellent results in the range of $\left|\frac{\tilde{E}}{\bar{y}_e}\right|_{avg} < 2.5\%$ for the VSL assessment. At the first HFS, the R2L, V2F, $k-\omega$, RST and SA model all gave excellent results for the VSL validation. The best results being from the RST model, giving $\left|\frac{\tilde{E}}{\bar{y}_e}\right|_{avg} = 0.7\%$.

The excellent results for the u velocity validations however did not correlate to good heat flux results in most cases, similar to the occurrence at the third HFS for the M1 case.

At the first HFS, the SLR model gave the best heat flux relative error, $\frac{\tilde{E}}{\bar{y}_e} = -4.3\%$, while only giving $\left|\frac{\tilde{E}}{\bar{y}_e}\right|_{avg} = 13.3\%$ for the VSL assessment. And at the second HFS, the SST model gave the best heat flux result, $\frac{\tilde{E}}{\bar{y}_e} = 0.6\%$, but gave $\left|\frac{\tilde{E}}{\bar{y}_e}\right|_{avg} = 15.7\%$ for the VSL. While at the third HFS, the SA model gave the best heat flux result in addition to the u velocity, giving $\frac{\tilde{E}}{\bar{y}_e} = 3.1\%$. Note also that the R2L and RST models gave excellent results for the heat flux assessment at HFS three despite giving poorer results for the u velocity.

5.3.2.3 2^{nd} Mixed Case

The FULL relative error results show that fair agreement is found by all the turbulence models with the experiment, giving $\left|\frac{\tilde{E}}{\bar{y}_e}\right|_{avg} < 14\%$ with the extreme values generally from the results at the first HFS. As with the M1 case, the best results are given by the SLR, SST and V2F models. The SLR gave the best results in FULL, VSL and heat flux assessments at the first HFS, giving values of $\left|\frac{\tilde{E}}{\bar{y}_e}\right|_{avg} = 9.3\%$, 28.8% and $\frac{\tilde{E}}{\bar{y}_e} = 21.2\%$, respectively. And at the third HFS, the V2F model also gave the best results for all three assessments, giving values of $\left|\frac{\tilde{E}}{\bar{y}_e}\right|_{avg} = 6\%$, 4.9% and $\frac{\tilde{E}}{\bar{y}_e} = -9.8\%$, respectively.

Note that the heat flux relative error results, $\frac{\tilde{E}}{\bar{y}_e}$, of the M1 and M2 cases are relatively equivalent for most of the turbulence models. A likely reason for this equivalence was mentioned earlier. The lower fluid velocity allowed the heat in the plate to be conducted axially rather than being convected away, which allowed the heated plate to become more uniform in temperature (see Fig. 3.14). Therefore, the two cases to have similar boundary conditions and results.

5.3.2.4 2^{nd} Forced Case

As with the F1 case, very good general agreement is found by all of the turbulence models from the FULL assessment results, giving results in the range of $\left|\frac{\tilde{E}}{\bar{y}_e}\right|_{avg} \approx 5\%$. In contrast to the F1 results however, good agreement was also found by all the turbulence models in the VSL assessment, with the worst models giving results in the range of $\left|\frac{\tilde{E}}{\bar{y}_e}\right|_{avg} \approx 10\%$ and the best giving $\left|\frac{\tilde{E}}{\bar{y}_e}\right|_{avg} \approx 2\%$. This greater level of agreement with experiment is evident in Fig. 5.12 when compared with Fig. 5.11.

For the heat flux assessment, the SLR gave the best results at the first HFS location, giving $\frac{\tilde{E}}{\overline{y}_e} = -5.3\%$. The $k - \omega$ model performed best at the third HFS, giving $\frac{\tilde{E}}{\overline{y}_e} = 1.5\%$, but the R2L, S2L, V2F, SST and RST models also showed excellent agreement.

It is unclear why the CFD turbulence models were more capable of predicting the fluid velocity and heat flux of the F2 flow over the F1 flow. Better results were expected for the F1 flow, because its thermal boundary condition presented a less difficult situation to model than the F2 thermal condition. It is recommended that future research be conducted to investigate this result.

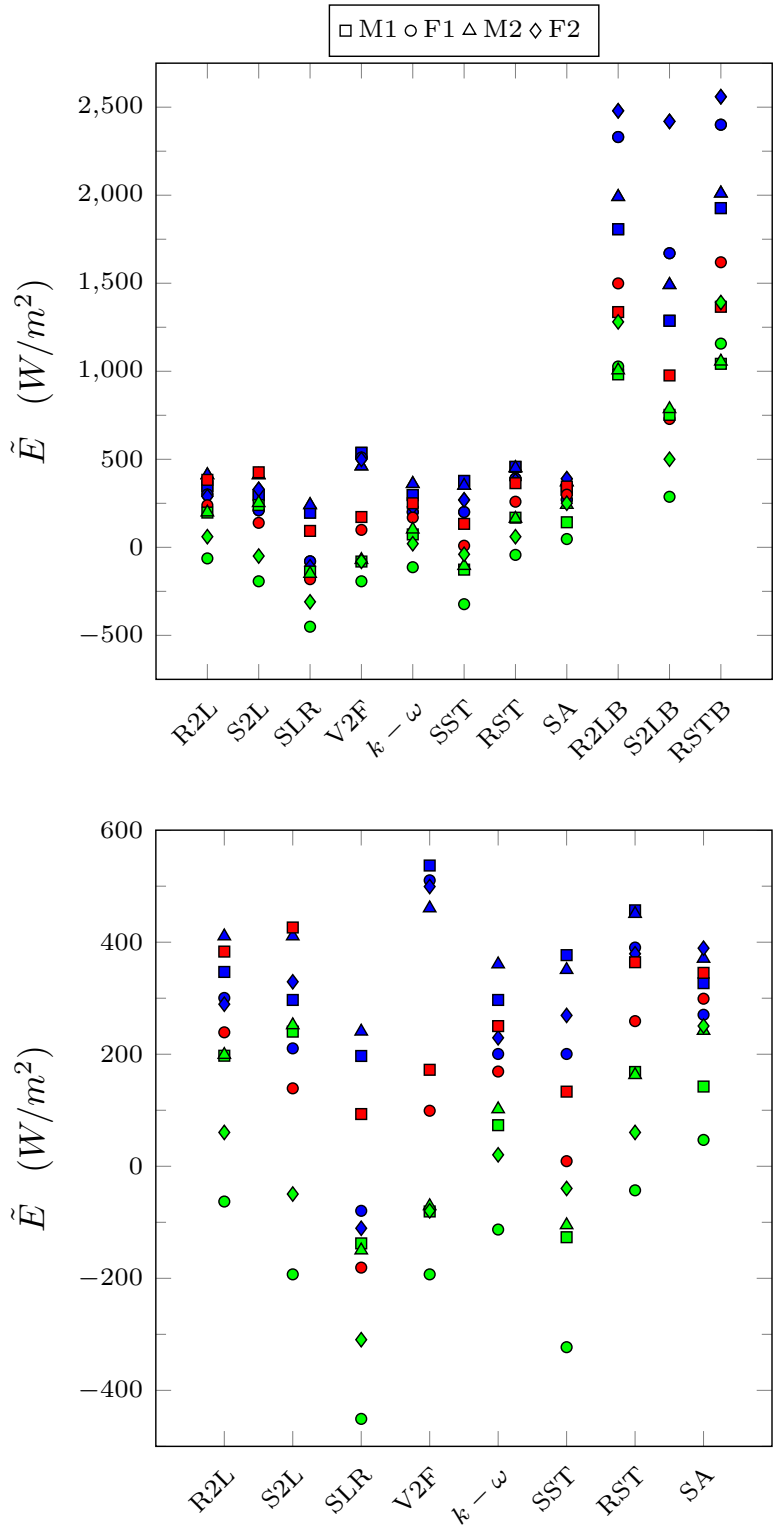

Fig. 5.10: Heat flux error of each turbulence model for each validation case and HFS location: $x = 16$ cm (blue), $x = 77$ cm (red), $x = 139$ cm (green).

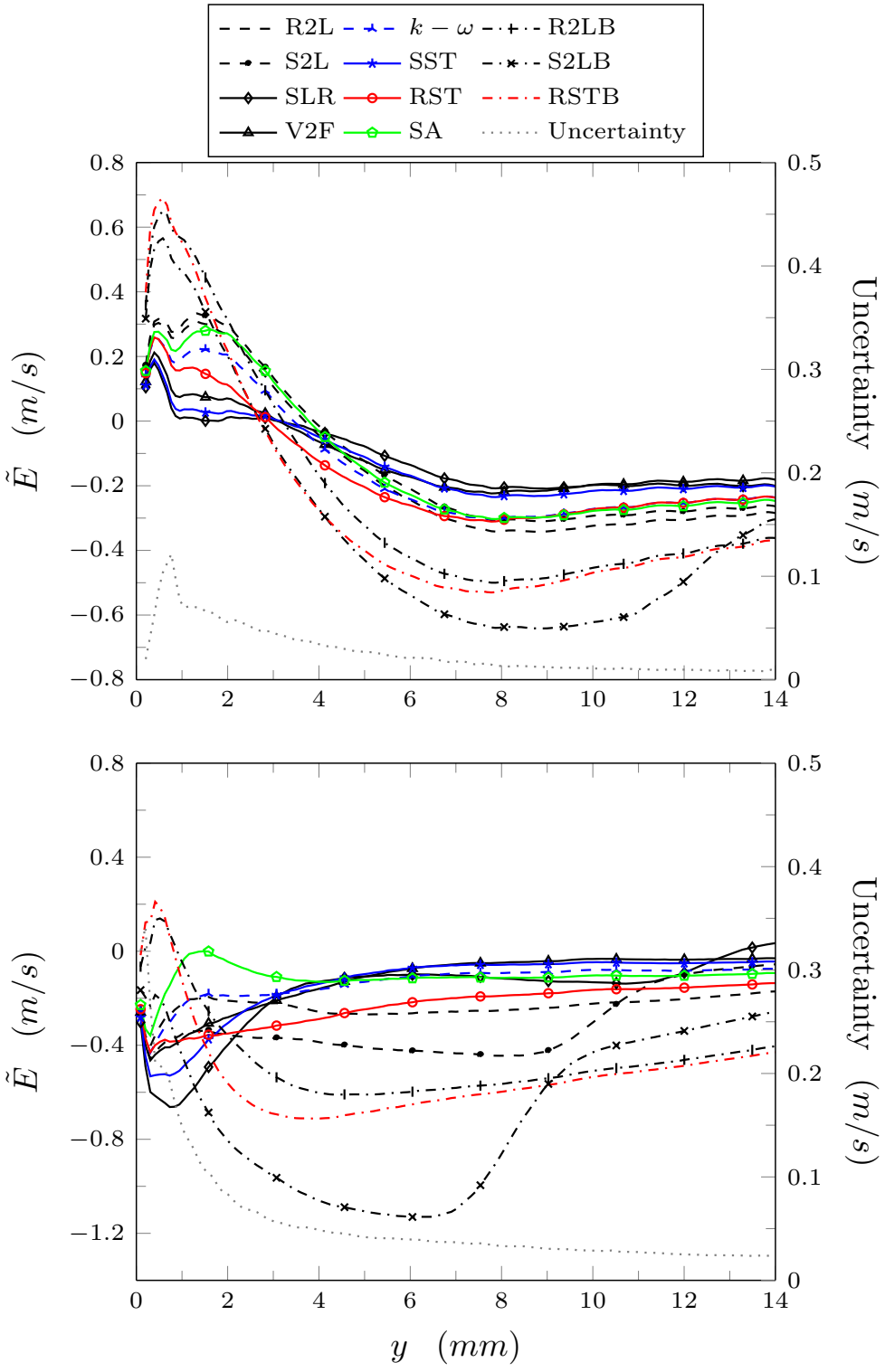

Fig. 5.11: Streamwise velocity (u) error of each turbulence model for the M1 (top) and F1 (bottom) validation case at HFS location 3.

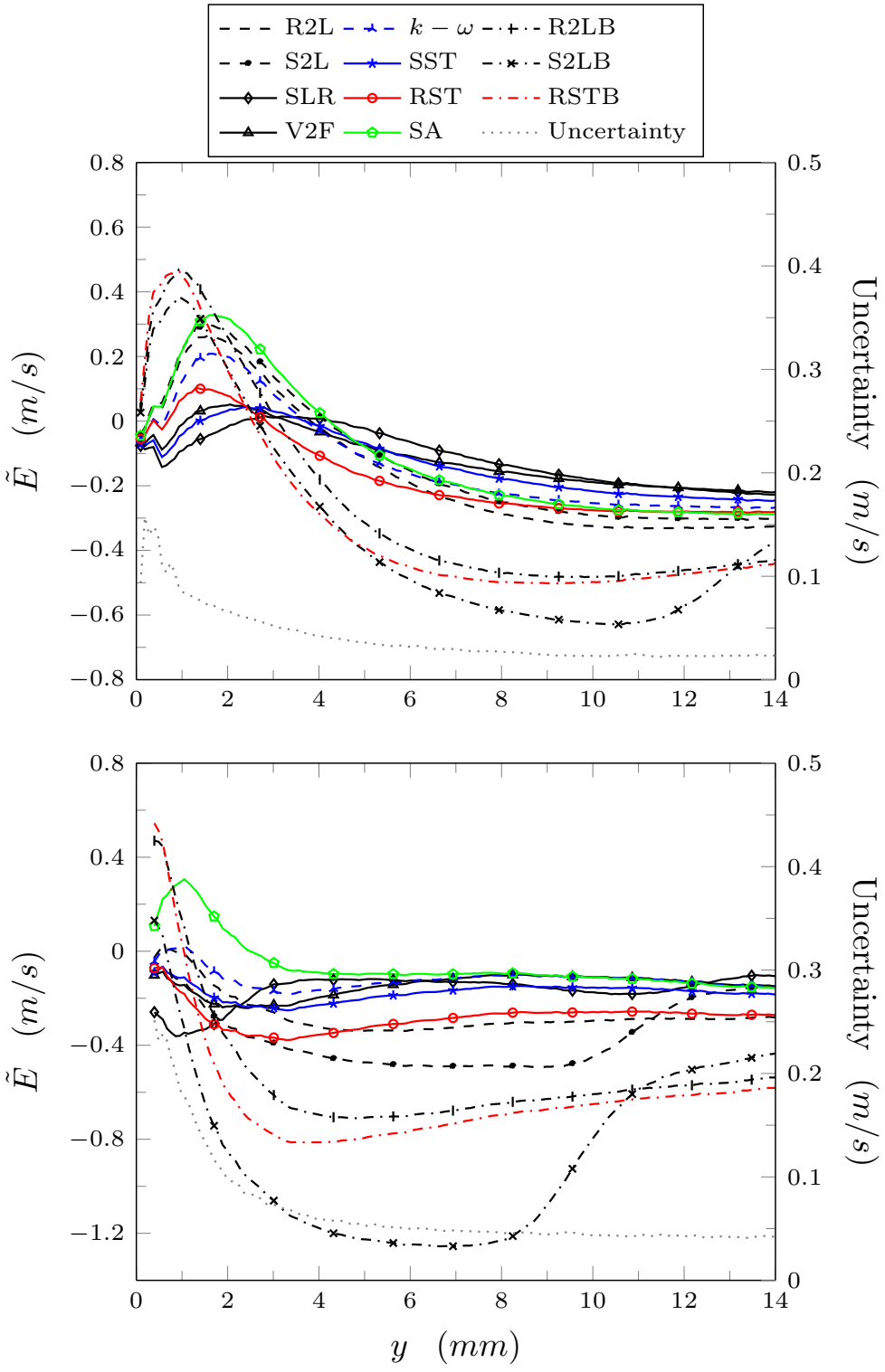

Fig. 5.12: Streamwise velocity (u) error of each turbulence model for the M2 (top) and F2 (bottom) validation case at HFS location 3.

Table 5.3: FULL Assessment: Relative error of u velocity for each turbulence model and validation case with 95% confidence indicator at the third HFS location.

	M1		F1		M2		F2	
Model	Average (%)	Maximum (%)	Average (%)	Maximum (%)	Average (%)	Maximum (%)	Average (%)	Maximum (%)
R2L	19.4 ± 3.2	380.3 ± 62.0	7.2 ± 2.2	54.4 ± 71.7	11.0 ± 3.5	30.1 ± 62.1	7.1 ± 2.4	9.3 ± 1.5
S2L	19.2 ± 3.2	391.8 ± 62.0	9.0 ± 2.2	58.2 ± 71.7	10.6 ± 3.5	29.0 ± 7.9	9.4 ± 2.4	12.9 ± 1.3
SLR	9.5 ± 3.2	241.3 ± 62.0	6.4 ± 2.2	68.0 ± 71.7	6.1 ± 3.5	50.9 ± 62.1	5.0 ± 2.4	27.6 ± 26.8
V2F	11.5 ± 3.2	279.9 ± 62.0	4.5 ± 2.2	58.4 ± 71.7	6.0 ± 3.5	44.5 ± 62.1	4.3 ± 2.4	10.9 ± 26.8
$k-\omega$	16.3 ± 3.2	330.6 ± 62.0	4.6 ± 2.2	56.5 ± 71.7	8.7 ± 3.5	36.5 ± 62.1	3.3 ± 2.4	5.3 ± 2.0
SST	10.7 ± 3.2	254.1 ± 62.0	5.1 ± 2.2	63.3 ± 71.7	6.7 ± 3.5	47.4 ± 62.1	5.0 ± 2.4	9.6 ± 26.8
RST	15.9 ± 3.2	337.7 ± 62.0	7.3 ± 2.2	55.4 ± 71.7	8.5 ± 3.5	36.5 ± 62.1	7.8 ± 2.4	11.6 ± 11.6
SA	17.6 ± 3.2	353.0 ± 62.0	3.7 ± 2.2	51.3 ± 71.7	10.5 ± 3.5	30.5 ± 7.9	3.6 ± 2.4	17.5 ± 18.6
R2LB	33.5 ± 3.2	801.7 ± 62.0	12.8 ± 2.2	18.0 ± 1.4	19.7 ± 3.5	92.8 ± 39.8	15.6 ± 2.4	50.2 ± 26.8
S2LB	33.3 ± 3.2	710.1 ± 62.0	18.4 ± 2.2	37.2 ± 71.7	20.7 ± 3.5	77.0 ± 39.8	22.8 ± 2.4	33.3 ± 1.5
RSTB	35.4 ± 3.2	889.7 ± 62.0	14.8 ± 2.2	21.9 ± 1.8	20.9 ± 3.5	109.3 ± 46.0	17.7 ± 2.4	58.0 ± 26.8

Table 5.4: VSL Assessment: Relative error of u velocity for each turbulence model and validation case with 95% confidence indicator at the third HFS location.

	M1		F1		M2		F2	
Model	Average (%)	Maximum (%)	Average (%)	Maximum (%)	Average (%)	Maximum (%)	Average (%)	Maximum (%)
R2L	40.7 ± 11.8	72.4 ± 28.5	10.9 ± 6.7	18.2 ± 12.9	23.0 ± 11.5	26.0 ± 7.9	3.7 ± 6.7	6.2 ± 3.7
S2L	43.9 ± 11.8	76.5 ± 28.5	17.3 ± 6.7	24.6 ± 12.9	26.3 ± 11.5	29.0 ± 7.9	9.3 ± 6.7	10.8 ± 3.7
SLR	2.6 ± 11.8	22.6 ± 28.5	28.3 ± 6.7	41.0 ± 12.9	11.7 ± 11.5	24.9 ± 19.6	15.0 ± 6.7	20.1 ± 11.3
V2F	12.2 ± 11.8	35.9 ± 28.5	17.3 ± 6.7	26.0 ± 12.9	4.9 ± 11.5	15.5 ± 19.6	8.5 ± 6.7	8.3 ± 3.7
$k-\omega$	29.6 ± 11.8	55.7 ± 28.5	11.1 ± 6.7	20.5 ± 12.9	15.1 ± 11.5	19.2 ± 7.9	2.1 ± 6.7	4.0 ± 3.7
SST	6.0 ± 11.8	27.2 ± 28.5	22.0 ± 6.7	33.2 ± 12.9	6.0 ± 11.5	19.5 ± 19.6	7.2 ± 6.7	7.6 ± 3.7
RST	23.1 ± 11.8	53.7 ± 28.5	18.1 ± 6.7	23.9 ± 12.9	7.9 ± 11.5	10.3 ± 7.9	11.3 ± 6.7	11.6 ± 3.7
SA	36.2 ± 11.8	63.5 ± 28.5	2.5 ± 6.7	11.6 ± 12.9	26.8 ± 11.5	30.5 ± 7.9	10.1 ± 6.7	15.6 ± 11.3
R2LB	75.8 ± 11.8	162.0 ± 28.5	7.4 ± 6.7	11.6 ± 3.3	54.5 ± 11.5	67.8 ± 19.6	7.9 ± 6.7	12.6 ± 11.3
S2LB	61.4 ± 11.8	139.1 ± 28.5	25.5 ± 6.7	27.8 ± 3.3	43.6 ± 11.5	55.0 ± 19.6	24.5 ± 6.7	28.6 ± 3.7
RSTB	72.4 ± 11.8	169.4 ± 28.5	12.3 ± 6.7	18.7 ± 3.3	52.3 ± 11.5	74.9 ± 19.6	12.7 ± 6.7	19.6 ± 3.7

Table 5.5: Heat flux results for each turbulence model and validation case with relative error ($\tilde{E}/\bar{y}_e$) and uncertainty at the third HFS location.

	M1			F1			M2			F2		
Model	y_m (W/m^2)	$\bar{y}_e$ (W/m^2)	$\tilde{E}/\bar{y}_e$ (%)	y_m (W/m^2)	$\bar{y}_e$ (W/m^2)	$\tilde{E}/\bar{y}_e$ (%)	y_m (W/m^2)	$\bar{y}_e$ (W/m^2)	$\tilde{E}/\bar{y}_e$ (%)	y_m (W/m^2)	$\bar{y}_e$ (W/m^2)	$\tilde{E}/\bar{y}_e$ (%)
R2L	885.3	687.7	28.7	1283.8	1343.0	-4.4	922.8	723.9	27.5	1446.1	1389.6	4.1
S2L	928.2		35.0	1146.6		-14.6	976.0		34.8	1335.6		-3.9
SLR	550.2		-20.0	892.3		-33.6	574.1		-20.7	1083.7		-22.0
V2F	606.6		-11.8	1153.4		-14.1	653.0		-9.8	1313.5		-5.5
$k-\omega$	761.0		10.7	1231.8		-8.3	826.3		14.1	1411.1		1.5
SST	561.4		-18.4	1021.4		-23.9	619.4		-14.4	1346.0		-3.1
RST	855.7		24.4	1299.8		-3.2	887.3		22.6	1449.7		4.3
SA	829.5		20.6	1385.1		3.1	966.1		33.5	1641.7		18.1
R2LB	1667.3		142.5	2373.7		76.8	1725.4		138.3	2673.7		92.4
S2LB	1437.5		109.0	1627.8		21.2	1510.5		108.7	1889.9		36.0
RSTB	1727.0		151.1	2499.7		86.1	1779.2		145.8	2777.2		99.9
Uncertainty		± 14.2	± 2.1		± 27.6	± 2.1		± 14.5	± 2.0		± 27.8	± 2.0

5.4 Grid Convergence Results

Values for the grid sizes N, characteristic cell size h, and step size ratios r for each of the four validation cases are shown in Table 5.6. Results from the GCI method for grid refinement outlined in Chapter 3 are tabulated in Tables 5.7–5.11 for the heat flux and u velocity at the third HFS of each validation case. The GCI method results for the other HFS locations are contained in Appendix D. Note that the tabulated GCI results for the u velocity illustrate the global character of each turbulence model, showing the global order of accuracy, p_{avg}, the maximum discretization error found in the velocity profile, GCI_{fine}, and the percentage of the velocity profile where oscillatory convergence occurred.

In Tables 5.7–5.11, the values listed for the GCI_{fine} index for each turbulence model can be considered the amount of error in the CFD solution due to the level of refinement in the mesh. For example, from Table D.3, based off the three different characteristic cell sizes used in the simulations for the SLR M2 case, one can expect the value for the simulated wall heat flux to be within 28.64% of $\phi_1 = 1392.9\ W/m^2$ as the characteristic cell size approaches zero. In this particular case, because the discretization error is similar in magnitude to the relative error between the experimental value and the SLR CFD solution, $\frac{\tilde{E}}{\overline{y}_e} = 20\%$, the error due to grid refinement is significant and therefore must be considered among other possible sources of error; such as turbulence modeling, boundary conditions, etc. This example however, illustrates a discretization error outside the general norm seen in the GCI results. The GCI values shown in the tabulated results are generally in the range of $GCI_{fine} \approx 1.0\%$ and most being less than 0.5%, for both the heat flux and u velocity, implying that the error due to grid refinement is insignificant in comparison with other error sources.

The exceptions to the general results are given by the SLR, S2L and S2LB turbulence models. The SLR model GCI results only varied significantly from 1.0% at the first HFS location, whereas the S2L and S2LB models varied significantly in almost every instance. Also, note that the max u velocity discretization error in the range of $GCI_{fine} \approx 15\%$ listed in Table D.5 for the M2 case is relative to an isolated near-wall location in the velocity

profile. The general results for the discretization error in that case are in agreement with those shown in the other tabulated results, where the max GCI_{fine} is less than 1.0%.

The level of grid refinement in this study was sufficiently refined that, at a few instances, the GCI method for estimation of the discretization error was invalid, see Section 3.1.4. For example, from Table D.3, the three simulations used to predict the wall heat flux at the first HFS gave $\phi_1 = 1561.1$, $\phi_2 = 1559.6$ and $\phi_3 = 1558.1$ W/m^2; clearly denoting a nearly grid converged solution. However, the discretization error was estimated as $GCI_{fine} = 73.86\%$ with an order of accuracy of $p = 0.0027$. The occurrence of situations where the GCI method is invalid shows that the level of refinement required to achieve a CFD solution with negligible discretization error varies between turbulence models.

Table 5.6: Grid size N, characteristic cell size h and grid ratios used for the GCI method.

Parameter	M1	F1	M2	F2
N_1	20,482,880	24,686,420	20,930,580	26,680,500
N_2	9,290,400	11,095,866	9,423,594	11,907,828
N_3	4,333,500	5,133,375	4,443,494	5,475,734
h_1 (m^3)	2.3087E-9	1.5247E-9	2.3099E-9	1.5207E-9
h_2 (m^3)	4.2697E-9	2.8259E-9	4.2923E-9	2.8385E-9
h_3 (m^3)	7.7814E-9	5.1863E-9	7.8263E-9	5.2090E-9
r_{21}	1.849	1.853	1.858	1.867
r_{32}	1.822	1.835	1.823	1.835

Table 5.7: M1 GCI method results for grid refinement of the heat flux at the third HFS.

Parameter	R2L	S2L	SLR	V2F	$k-\omega$	SST	RST	SA	R2LB	S2LB	RSTB
ϕ_1 (W/m^2)	885.3	928.2	550.2	606.6	761.0	561.4	855.7	829.5	1667.3	1437.5	1727.0
ϕ_2 (W/m^2)	882.4	926.7	551.3	607.4	761.2	561.6	853.9	828.6	1664.6	1701.3	1727.1
ϕ_3 (W/m^2)	879.0	924.8	555.6	609.1	762.6	562.2	852.0	828.3	1661.2	1746.5	1728.3
p	0.37	0.48	2.25	1.14	3.09	1.47	0.04	1.43	0.39	2.79	4.52
ϕ_{ext}^{21}	896.2	932.4	549.9	605.7	761.0	561.2	921.8	830.2	1677.5	1379.5	1727.0
e_a^{21}	0.32%	0.16%	0.20%	0.14%	0.03%	0.04%	0.21%	0.11%	0.16%	18.35%	0.00%
e_{ext}^{21}	1.22%	0.45%	0.07%	0.14%	0.00%	0.03%	7.17%	0.08%	0.61%	4.20%	0.00%
GCI_{fine}^{21}	1.55%	0.57%	0.08%	0.17%	0.01%	0.04%	9.65%	0.10%	0.76%	5.04%	0.00%
Convergence*	M	M	M	M	M	M	M	M	M	M	M

* Note: M and O denote monotonic and oscillatory convergence, respectively.

Table 5.8: F1 GCI method results for grid refinement of the heat flux at the third HFS.

Parameter	R2L	S2L	SLR	V2F	$k-\omega$	SST	RST	SA	R2LB	S2LB	RSTB
ϕ_1 (W/m^2)	1283.8	1146.6	892.3	1153.4	1231.8	1021.4	1299.8	1385.1	2373.7	1627.8	2499.7
ϕ_2 (W/m^2)	1280.5	1257.6	981.3	1154.6	1232.1	1005.5	1301.4	1404.4	2371.8	1810.5	2504.0
ϕ_3 (W/m^2)	1276.0	1358.8	979.7	1157.0	1231.5	1023.9	1303.3	1408.4	2370.4	2126.0	2506.0
p	0.53	0.12	6.40	1.15	1.45	0.24	0.33	2.93	0.50	0.92	1.24
ϕ_{ext}^{21}	1292.3	265.8	890.6	1152.2	1231.6	1122.9	1292.7	1379.8	2379.0	1388.3	2495.9
e_a^{21}	0.26%	9.68%	9.98%	0.11%	0.02%	1.55%	0.12%	1.39%	0.08%	11.23%	0.17%
e_{ext}^{21}	0.66%	531.38%	0.20%	0.10%	0.01%	9.04%	0.55%	0.38%	0.22%	17.25%	0.15%
GCI_{fine}^{21}	0.83%	153.98%	0.25%	0.13%	0.02%	12.42%	0.68%	0.48%	0.28%	18.39%	0.19%
Convergence*	M	M	O	M	O	O	M	M	M	M	M

* Note: M and O denote monotonic and oscillatory convergence, respectively.

Table 5.9: M2 GCI method results for grid refinement of the heat flux at the third HFS.

Parameter	R2L	S2L	SLR	V2F	$k-\omega$	SST	RST	SA	R2LB	S2LB	RSTB
ϕ_1 (W/m^2)	922.8	976.0	574.1	653.0	826.3	619.4	887.3	966.1	1725.4	1510.5	1779.2
ϕ_2 (W/m^2)	919.7	975.0	577.2	654.0	825.7	624.3	886.1	964.0	1722.8	1793.4	1780.1
ϕ_3 (W/m^2)	916.2	974.0	579.7	655.9	825.4	631.6	885.9	965.7	1719.6	1823.0	1781.8
p	0.18	0.06	0.28	0.98	0.84	0.69	2.61	0.34	0.39	3.52	0.93
ϕ_{ext}^{21}	950.2	1002.6	557.6	651.7	827.2	610.2	887.5	975.1	1735.2	1474.5	1777.9
e_a^{21}	0.34%	0.10%	0.54%	0.16%	0.08%	0.79%	0.13%	0.22%	0.15%	18.73%	0.05%
e_{ext}^{21}	2.88%	2.65%	2.96%	0.20%	0.11%	1.51%	0.03%	0.92%	0.56%	2.44%	0.07%
GCI_{fine}^{21}	3.71%	3.40%	3.59%	0.24%	0.14%	1.86%	0.04%	1.17%	0.70%	2.98%	0.09%
Convergence*	M	M	M	M	M	M	M	O	M	M	M

* Note: M and O denote monotonic and oscillatory convergence, respectively.

Table 5.10: F2 GCI method results for grid refinement of the heat flux at the third HFS.

Parameter	R2L	S2L	SLR	V2F	$k-\omega$	SST	RST	SA	R2LB	S2LB	RSTB
ϕ_1 (W/m^2)	1446.1	1335.6	1083.7	1313.5	1411.1	1346.1	1449.7	1641.7	2673.7	1889.9	2777.2
ϕ_2 (W/m^2)	1441.9	1469.6	1113.7	1314.1	1411.7	1334.1	1448.0	1634.8	2672.3	2158.1	2779.7
ϕ_3 (W/m^2)	1435.7	1517.8	1122.4	1315.4	1412.2	1318.7	1447.0	1637.0	2667.3	2613.4	2782.2
p	0.68	1.57	1.90	1.21	0.62	0.47	0.97	1.83	2.11	0.91	0.04
ϕ_{ext}^{21}	1454.0	1254.9	1070.6	1312.9	1409.7	1381.1	1451.9	1645.0	2674.2	1537.5	2684.2
e_a^{21}	0.29%	10.03%	2.77%	0.05%	0.05%	0.89%	0.12%	0.42%	0.05%	14.19%	0.09%
e_{ext}^{21}	0.54%	6.43%	1.23%	0.04%	0.10%	2.54%	0.15%	0.20%	0.02%	22.93%	3.46%
GCI_{fine}^{21}	0.68%	7.55%	1.51%	0.05%	0.12%	3.26%	0.18%	0.25%	0.02%	23.31%	4.19%
Convergence*	M	M	M	M	M	M	M	O	M	M	M

* Note: M and O denote monotonic and oscillatory convergence, respectively.

Table 5.11: Global GCI method results for grid refinement of the u velocity profile at the third HFS.

Case	Parameter	R2L	S2L	SLR	V2F	$k-\omega$	SST	RST	SA	R2LB	S2LB	RSTB
M1	p_{local} (Min -Max)	0.0 -8.6	0.0 -9.3	0.0 -6.1	0.0 -7.0	0.2 -7.3	0.0 -8.4	0.1 -6.2	0.3 -6.7	0.1 -8.7	0.0 -7.7	0.1 -8.7
	p_{avg}	3.06	1.66	3.15	2.92	2.70	3.09	3.45	3.33	3.26	1.67	3.38
	Max GCI_{fine} (%)	0.08	0.18	0.07	0.06	0.08	0.07	0.04	0.06	0.05	6.78	0.02
	Osc. Convergence (%)	86.29	15.86	75.86	74.14	69	72.86	92.43	91.57	92.57	25.71	96.43
F1	p_{local} (Min -Max)	0.0 -11.5	0.0 -5.6	0.0 -10.0	0.0 -6.0	0.0 -6.1	0.0 -6.1	0.0 -7.1	0.0 -8.7	0.0 -6.9	0.0 -6.6	0.0 -6.7
	p_{avg}	2.29	1.15	2.37	2.62	2.31	2.35	1.19	2.14	2.8	1.21	1.44
	Max GCI_{fine} (%)	0.12	9.46	3.07	0.12	0.13	0.51	0.45	0.69	0.03	14.37	0.22
	Osc. Convergence (%)	53.43	10.71	11.57	62.57	57.57	59.71	9.57	23.86	70.86	13.43	20.57
M2	p_{local} (Min -Max)	0.0 -8.1	0.0 -5.9	0.0 -7.5	0.0 -7.0	0.1 -8.2	0.0 -8.8	0.2 -9.7	0.0 -6.8	0.0 -6.0	0.0 -8.1	0.1 -10.2
	p_{avg}	3.05	0.71	2.58	2.99	3.20	2.55	2.40	2.71	3.04	1.94	2.31
	Max GCI_{fine} (%)	0.08	0.60	0.18	0.08	0.05	0.25	0.08	0.11	0.08	5.03	0.18
	Osc. Convergence (%)	39	3.71	49.57	77.86	80.43	56.14	13.14	69	84.86	25	20.43
F2	p_{local} (Min -Max)	0.0 -5.1	0.0 -5.9	0.0 -7.1	0.0 -7.2	0.1 -7.4	0.0 -8.5	0.0 -7.4	0.0 -7.7	0.0 -6.4	0.1 -8.6	0.0 -5.7
	p_{avg}	1.79	0.93	1.73	1.80	0.9	3.30	1.69	2.31	1.42	1.39	1.07
	Max GCI_{fine} (%)	0.23	14.43	1.78	0.14	0.42	0.15	0.14	0.19	0.13	11.35	0.24
	Osc. Convergence (%)	38.86	7.57	19.14	39.43	16.14	61	22.14	34.43	29.71	13.14	7.57

Chapter 6

Conclusion

This study found that the SLR turbulence model was most capable of predicting mixed convection flow, predicting the experimental heat flux values within $\frac{\tilde{E}}{\bar{y}_e} \approx 20\%$ and the FULL and VSL velocity profiles within $\left|\frac{\tilde{E}}{\bar{y}_e}\right|_{avg} \approx 10\%$ and 3%, respectively. For forced convection flow, results varied depending on the thermal state of the heated plate boundary condition, though more consistent results were found at the third HFS where the flow was more developed thermally. The SA turbulence model predicted the u velocity very well in the F1 case for both the FULL and VSL assessments, predicting the velocity within $\left|\frac{\tilde{E}}{\bar{y}_e}\right|_{avg} \approx 5\%$ and 2.5% of the experiment, respectively. While for F2 case, many of the turbulence models were able to predict the u velocity and the heat flux at the third HFS very well. Overall, it was deduced that for forced convection the $k-\omega$ model gave the most consistent results, simulating the experimental heat flux within $\frac{\tilde{E}}{\bar{y}_e} \approx 15\%$ and the FULL and VSL u velocity profiles within $\left|\frac{\tilde{E}}{\bar{y}_e}\right|_{avg} \approx 5\%$ and 10%, respectively.

The study results showed that the SLR turbulence model was most capable of predicted the wall heat flux in the developing thermal boundary layer, for both mixed and forced convection, simulating the mixed convection heat flux within $\frac{\tilde{E}}{\bar{y}_e} \approx 20\%$ and the forced convection heat flux within $\frac{\tilde{E}}{\bar{y}_e} \approx 5\%$. Also, as the flow developed along the test section the V2F and $k-\omega$ models gave more consistent and accurate predictions of the wall heat flux than the other turbulence models, see Fig. 5.10, simulating the experiment within $\frac{\tilde{E}}{\bar{y}_e} \approx 15\%$.

The GCI method estimation of the discretization error for the simulated wall heat flux and u velocity was generally within 1.0%; exceptions often occurring by the S2L, S2LB, and SLR turbulence models, particularly at the first HFS location. Most of the estimated discretization errors were within 0.5%, indicating excellent grid convergence in the CFD

simulations.

6.1 Sources of CFD Uncertainty

Versteeg [7] cites the main sources of error and uncertainty that are prevalent in CFD. Causes of error include: numerical, coding and user errors. Numerical errors refer to round-off, iterative convergence and discretization errors; coding errors refer to mistakes in the software, which are inherent in unverified CFD code; and user errors refer to human errors made through incorrect use of the software. For this study, the verified STAR-CCM+ software was executed in double precision by an individual competent in CFD simulation and the ASME iterative convergence threshold was upheld by all of the CFD simulations performed; except for the intermittency transport equation included in the SST turbulence model simulations. The numerical discretization cause of error however, must be considered.

The grid convergence results from the GCI method showed that the error due to discretization in many instances was insignificant compared to other sources of error. However, for the SLR turbulence model, there were many instances where the discretization error was greater than the estimated 1.0% uncertainty noted for the PIV data in Chapter 2, where GCI_{fine} values were found in the $1.2 - 3\%$ range for the forced convection cases. Furthermore, for the F1 and M2 cases, discretization errors in excess of the experimental uncertainty were found for the heat flux calculated, see Tables D.2 and D.3. These discrepancies are significant because the SLR model was found to give the best results for the wall heat flux at the HFS location in question; meaning that, due to the uncertainty implied by the large discretization error, the SLR model may not be the most capable model in predicting the heat flux in the developing thermal boundary layer.

Mesh discretization as a source of error in this study, though generally only significant in a few instances, is mainly due to the solution of the CFD turbulence models over the same set of three discretized meshes for each validation case. The uniformity in the mesh between the model simulations eliminated sources of error in the validation study based on the mesh discretization and therefore the simulation boundary conditions. However, each turbulence model requires a different level of mesh refinement in order to obtain a solution where

discretization error is negligible. Therefore, as a result of the mesh uniformity between the turbulence models some of the CFD solutions contain discretization error that is not negligible. This is in conflict with the mean comparison validation method implemented in this study, which assumes the discretization error is negligible. Thus, for the turbulence models with significant discretization error in their solutions, the modeling error confidence intervals reported do not account for the significant discretization error. However, because the discretization error is negligible for most of the turbulence model solutions, the mesh uniformity revealed which models require more or less mesh refinement and subsequently require a greater or lesser computational cost. It is therefore apparent that the SLR model requires additional mesh refinement, particularly in the region around the first HFS location, while the level of mesh refinement implemented is sufficient for the SA, V2F and $k-\omega$ models mentioned above.

From Versteeg, causes of uncertainty include: input and physical model uncertainty. Input uncertainty refers to inaccuracies due to limited information or approximate representation of geometry, boundary conditions, material properties, etc. Physical model uncertainty refers to discrepancies between real flows and CFD due to inadequate representation of physical or chemical processes (e.g. turbulence) or due to simplifying assumptions in the modeling process (e.g. incompressible flow, steady flow).

While neither input or physical model uncertainty can be neglected in this study, it is the author's belief that the most significant uncertainties in the CFD simulations presented in this study are due to the turbulence modeling. The fluid flow in the mixed convection cases was predicted to be considerably more turbulent than the experiment. As discussed earlier, the fluid flow appears to be transitional and not fully turbulent, thus the discrepancies between the model and experiment are reasonable because the turbulence models were used to solve a flow for which they were not formulated. In the forced convection cases, the u velocity error plots show that the turbulence models fail to duplicate the near-wall viscous flow, where there is a small buoyancy influence. Failure of the model to accurately account for buoyancy would affect the heat transfer predicted, thus the inconsistency of

the turbulence models in predicting the forced convection wall heat flux seems reasonable. This conclusion is in agreement with turbulence model assessments cited in the literature review [22, 23], where it was shown that the predicted turbulent kinetic energy, turbulent dissipation rate, and damping functions of turbulence models failed to duplicate those found in DNS studies.

As for input uncertainty, both the inlet and outlet boundary conditions are of concern. The velocity and turbulence profiles mapped onto the simulation velocity inlet were discussed in Chapter 3. It was assumed that the transverse velocities were equivalent, $w = v$, which was investigated in the freestream by comparison of PIV results from two orthogonal planes. However, it is possible that the transverse velocities in the boundary layer are not equivalent, which is pertinent because the boundary-layer flow was under investigation in this study. Additionally, the interpolation of the PIV velocity to a finer grid may have compounded the incorrect velocity and turbulence gradients. Thus the large discrepancies found in the results for the first HFS location may be due to the incorrect inlet conditions rather than any fault of the turbulence model.

The outlet boundary condition is of concern due to the zero gauge pressure enforced. As noted previously, this pressure specification is inaccurate because the simulation exit plane is not coincident with the RoBuT outlet to the ambient lab atmosphere, see Fig. 2.2. Though the simulated pressure drop is small, in the range of 5.0 Pa for both forced and mixed convection cases, this inaccurate pressure specification may be a concern due to its relation with the buoyancy influence predicted in the flow through the compressible ideal gas physics model. Direct measurement of the pressure at the inlet and outlet of the RoBuT test section in future studies would eliminate this concern.

6.2 Concluding Remarks

Computational fluid dynamics is an impressive tool in analyzing and modeling real world problems. However, it has its limitations, many of which due to turbulence modeling. In attempting to resolve the non-linearities that arise in the governing differential equations, turbulence models will never be exact. However, the insight obtained from CFD by visual-

izing and analyzing complex flows with little or no experimental validation is desirable in almost any industry today.

In this study, CFD turbulence models were able to model the overall behavior of fluid flow exhibiting forced and mixed convection heat transfer. For mixed convection, of the turbulence models validated, the SLR model was most adept at predicting the near-wall u velocity profile and heat flux; though consideration must be given to the level of uncertainty in its results due to discretization and modeling error. In modeling forced convection flow, the SLR model was most suited to predicting the developing thermal boundary layer heat flux. Additionally, if the heat transfer being modeled originates from a more ideal thermal boundary, one could expect excellent prediction of the near-wall u velocity and fully developed flow heat flux from the SA turbulence model. Overall, the V2F and $k-\omega$ models may be recommended for predicting the fully developed flow and heat transfer. It is worth noting that despite the relative differences between simulated and experimental values, CFD simulations can be used to predict values on or near the same order of magnitude as the real life values one is investigating, which is especially useful if experimentation is impossible.

References

[1] AMWEL Enterprises, "A Brief History of CFD," http://www.amwel.com/history.html, 2008, accessed 5/25/2013.

[2] Wolfram, S., *A New Kind of Science*, Wolfram Media Incorporated, Champaign, IL, 2002, pp. 996–1000.

[3] So, R. M. C., Sarkar, A., Gerodimos, G., and Zhang, J., "A Dissipation Rate Equation for Low-Reynolds-Number and Near-Wall Turbulence," *Theoretical and Computational Fluid Dynamics*, Vol. 9, 1997, pp. 47–63.

[4] Sarkar, A., and So, R. M. C., "A Critical Evaluation of Near-Wall Two-Equation Models against Direct Numerical Simulation Data," *Theoretical and Computational Fluid Dynamics*, Vol. 18, No. 2, April 1997, pp. 197–208.

[5] So, R. M. C., and Speziale, C. G., "A Review of Turbulent Heat Transfer Modeling," *Annual Review of Heat Transfer*, edited by C.-L. Tien, Vol. 10, Begell House Incorporated, New York, 1999, pp. 177–219.

[6] Kays, W., Crawford, M., and Weigand, B., *Convective Heat and Mass Transfer*, 4th ed., chap. 14, McGraw-Hill, Champaign, IL, 2005, pp. 292–329.

[7] Versteeg, H. K., and Malalasekera, W., *An Introduction to Computational Fluid Dynamics: The Finete Volume Method*, Pearson Education Limited, 2nd ed., Edinburgh Gate, Harlow, Essex CM20 2JE, England, 2007.

[8] Kader, B. A., and Yaglom, A. M., "Heat and Mass Transfer Laws for Fully Turbulent Wall Flows," *International Journal of Heat and Mass Transfer*, Vol. 15, 1972, pp. 2329–2351.

[9] Kader, B. A., "Temperature and Concentration Profiles in Fully Turbulent Boundary Layers," *International Journal of Heat and Mass Transfer*, Vol. 24, No. 9, 1981, pp. 1541–1544.

[10] Launder, B. E., and Spalding, D. B., "The Numerical Computation of Turbulent Flows," *Computer Methods in Applied Mechanics and Engineering*, Vol. 3, No. 2, 1974, pp. 269–289.

[11] Neale, A., Derome, D., Blocken, B., and Carmeliet, J., "Determination of Surface Convective Heat Transfer Coefficients by CFD," *Proceedings of NBEC 11th Building Science and Technology Conference*, Vol. 1, Banff, AB, Canada, March 2007, pp. 67–78.

[12] Thomas, E., Florian, M., and Wolfgang, V., "Heat Transfer Predictions Based on Two-Equation Turbulence Models," *The 6th ASME-JSME Thermal Engineering Joint Conference*, Vol. 1, Japan Society of Mechanical Engineers, Waimea, HI, 2007, pp. 67–78.

[13] Malhotra, A., and Hauptmann, E. G., "Heat Transfer to a Supercritical Fluid during Turbulent, Vertical Flow in a Circular Duct," *Heat Transfer and Turbulent Buoyant Convection*, edited by D. B. Spalding and N. Afgan, Vol. 1 of *Series in Thermal and Fluids Engineering*, Hemisphere Publishing Corporation, Washington, DC, 1977, pp. 405–414.

[14] Stillinger, D. C., Helland, K. N., and Van Atta, C. W., "Experiments on the Transition of Homogeneous Turbulence to Internal Waves in a Stratified Fluid," *Journal of Fluid Mechanics*, Vol. 131, 1983, pp. 91–122.

[15] Launder, B. E., "Heat and Mass Transport," *Topics in Applied Physics: Turbulence*, edited by P. Bradshaw, Vol. 12, Springer-Verlag, Berlin, Heidelberg, 1977, pp. 222–287.

[16] Petukhov, B. S., Poliakov, A. F., Shekhter, Y. L., and a Kuleshov, V., "Experimental Study of the Effect of Thermogravitation upon Turbulent Flow and Heat Transfer in Horizontal Pipes," *Heat Transfer and Turbulent Buoyant Convection*, edited by D. B. Spalding and N. Afgan, Vol. 2 of *Series in Thermal and Fluids Engineering*, Hemisphere Publishing Corporation, Washington, DC, 1977, pp. 719–727.

[17] Jackson, J. D., and Fewster, J., "Enhancement of Turbulent Heat Transfer due to Buoyancy for Downward Flow of Water in Vertical Tubes," *Heat Transfer and Turbulent Buoyant Convection*, edited by D. B. Spalding and N. Afgan, Vol. 2 of *Series in Thermal and Fluids Engineering*, Hemisphere Publishing Corporation, Washington, DC, 1977, pp. 759–775.

[18] Jackson, J. D., and Hall, W. B., "Forced Convection Heat Transfer to Fluids at Supercritical Pressure," *Turbulent Forced Convection in Channels & Rod Bundles*, Vol. 2, Hemisphere, NY, 1979, pp. 563–611.

[19] Petukhov, B. S., and Polyakov, A. F., *Heat Transfer in Turbulent Mixed Convection*, Hemisphere Publishing Corporation, New York, 1988.

[20] Sommer, T. P., and So, R. M. C., "Wall-Bounded Buoyant Turbulent Flow and its Modeling," *International Journal of Heat and Mass Transfer*, Vol. 39, No. 17, 1996, pp. 3595–3606.

[21] Spall, R. E., Richards, A., and McEligot, D. M., "An Assessment of $\kappa - \omega$ and $v^2 - f$ Turbulence Models for Strongly Heated Internal Gas Flows," *Numerical Heat Transfer: Part A: Applications*, Vol. 46, 2004, pp. 831–849.

[22] He, S., Kim, W. S., and Bae, J. H., "Assessment of Performance of Turbulence Models in Predicting Supercritical Pressure Heat Transfer in a Vertical Tube," *International Journal of Heat and Mass Transfer*, Vol. 51, 2008, pp. 4359–4675.

[23] Kim, W. S., He, S., and Jackson, J. D., "Assessment by Comparison with DNS Data of Turbulence Models used in Simulations of Mixed Convection," *International Journal of Heat and Mass Transfer*, Vol. 51, 2008, pp. 1293–1312.

[24] Petukhov, B. S., "Turbulent Flow and Heat Transfer in Pipes under Considerable Effect of Thermogravitational Forces," *Heat Transfer and Turbulent Buoyant Convection*, edited by D. B. Spalding and N. Afgan, Vol. 2 of *Series in Thermal and Fluids Engineering*, Hemisphere Publishing Corporation, Washington, DC, 1977, pp. 701–717.

[25] Spall, R. E., Nisipeanu, E., and Richards, A., "Assessment of a Second-Moment Closure Model for Strongly Heated Internal Gas Flows," *Journal of Heat Transfer*, Vol. 129, 2007, pp. 1719–1722.

[26] Harris, J. R., Lance, B. W., Iverson, J. M., Spall, R. E., Johnson, R. W., and Smith, B. L., "Validation Study on Forced and Mixed Convection in the Rotatable Buoyancy Tunnel," *Proceedings of the ASME 2013 Fluids Engineering Division Summer Meeting*, 2013, FEDSM2013-16214.

[27] Harris, J. R., Lance, B. W., Spall, R. E., and Smith, B. L., "Transient Mixed Convection Validation Facility and Study," *The 15th International Topical Meeting on Nuclear Reactor Thermalhydraulics*, Pisa, Italy, May 2013, NURETH15.

[28] Timmins, B. H., Wilson, B. M., Smith, B. L., and Vlachos, P. P., "A Method for Automatic Estimation of Instantaneous Local Uncertainty in Particle Image Velocimetry Measurements," *Experiments in Fluids*, Vol. 53, 2012, pp. 1133–1147.

[29] Lin, H. T., and Chen, C. C., "Mixed Convection on Vertical Plate for Fluids of any Prandtl Number," *Wärme- und Stoffübertragung*, Vol. 22, 1988, pp. 159–168.

[30] Oberkampf, W. L., and Roy, C. J., *Verification and Validation in Scientific Computing*, Cambridge University Press, New York, 2010, pp. 369–670.

[31] *USER GUIDE STAR-CCM+ Version 8.04.007*, CD-adapco, 2013.

[32] Chapra, S. C., and Canale, R. P., *Numerical Methods for Engineers*, 6th ed., McGraw-Hill, New York, 2010.

[33] Celik, I. B., Ghia, U., Roache, P. J., and Freitas, C. J., "Procedure for Estimation and Reporting of Uncertainty Due to Discretization in CFD Applications," http://journaltool.asme.org/Content/JFENumAccuracy.pdf, 2008, access 5/15/2013.

[34] Jones, W. P., and Launder, B. E., "The Prediction of Laminarization with a Two-Equation Model of Turbulence," *International Journal of Heat and Mass Transfer*, Vol. 15, 1972, pp. 301–314.

[35] Lien, F. S., Chen, W. L., and Leschziner, M. A., "Low-Reynolds Number Eddy-Viscosity Modelling based on Non-Linear Stress-Strain/Vorticity Relations," *Proceedings of the 3rd Symposium on Engineering Turbulence Modelling and Measurements*, Vol. 1, Crete, Greece, May 1996, pp. 27–29.

[36] Shih, T. H., Liou, W. W., Shabbir, A., Yang, Z., and Zhu, J., "A New $k - \varepsilon$ Eddy Viscosity Model for High Reynolds Number Turbulent Flows – Model Development and Validation," 1994, NASA TM 106721.

[37] Davidson, L., Nielson, P. V., and Sveningsson, A., "Modifications of the $\bar{v^2} - f$ Model for Computing the Flow in a 3D Wall Jet," *Turbulence, Heat and Mass Transfer 4*, edited by K. Hanjalič, Y. Nagano, and M. Tummers, Begell House, Antalya, Turkey, 2003.

[38] Lien, L. S., Kalitzin, G., and Durbin, P. A., "RANS Modeling for Compressible and Transitional Flows," *Center for Turbulence Research - Proceedings of the Summer Program*, Stanford, CA, 1998.

[39] Durbin, P. A., "On the $k - \varepsilon$ Stagnation Point Anomaly," *International Journal of Heat and Fluid Flow*, Vol. 17, 1996, pp. 89–90.

[40] Wilcox, D. C., *Turbulence Modeling for CFD*, 2nd ed., DCW Industries, Inc, La Canada, CA, 1998.

[41] Menter, F. R., "Two-Equation Eddy-Viscosity Turbulence Modeling for Engineering Applications," *AIAA Journal*, Vol. 32, No. 8, 1994, pp. 1598–1605.

[42] Spalart, P. R., and Allmaras, S. R., "A One-Equation Turbulence Model for Aerodynamic Flows," 1992, AIAA-92-0439.

[43] Sharp, K. V., and Adrian, R. J., "PIV Study of Small-Scale Flow Structure around a Rushton Turbine," *American Institute of Chemical Engineers*, Vol. 47, No. 4, 2001, pp. 766–778.

[44] Roache, P. J., Ghia, K. N., and White, F. M., "Journal of Fluids Engineering Editorial Policy Statement on the Control of Numerical Accuracy," http://journaltool.asme.org/Content/JFENumAccuracy.pdf, 1986, access 5/15/2013.

[45] *Standard for Verification and Validation in Computational Fluid Dynamics and Heat Transfer*, The American Society of Mechanical Engineers, New York, 2009.

[46] Beckwith, T. G., Marangoni, R. D., and V, J. H. L., *Mechanical Measurements*, 6th ed., chap. 3, Pearson Prentice Hall, Upper Saddle River, NJ, 2007, p. 58.

Appendices

Appendix A

Inlet Velocity Profiles

A.1 M1

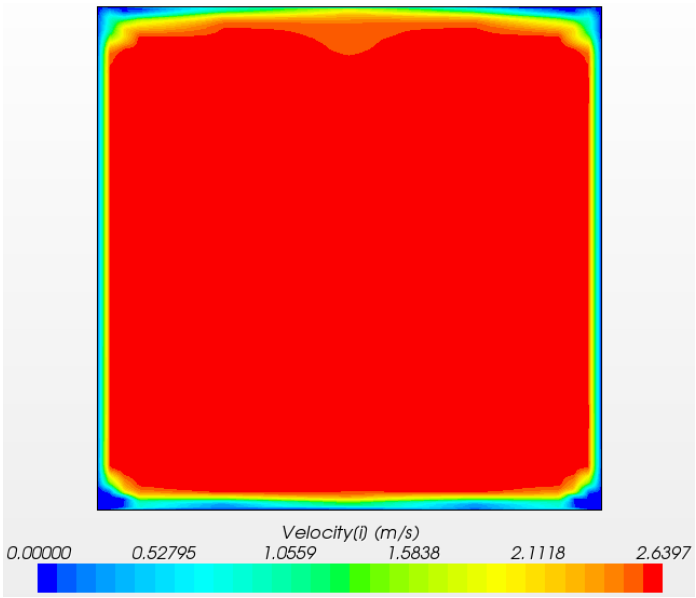

Fig. A.1: u velocity mapped onto the velocity inlet of the computational domain for the M1 validation case.

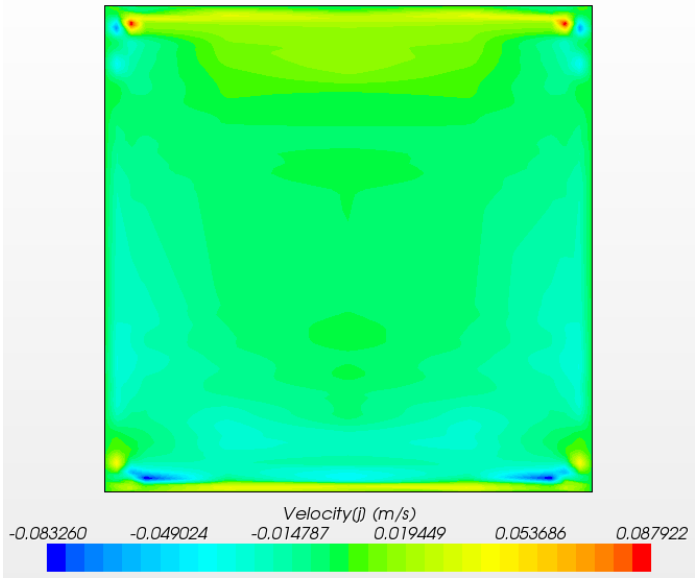

Fig. A.2: v and w velocity mapped onto the velocity inlet of the computational domain for the M1 validation case.

A.2 F1

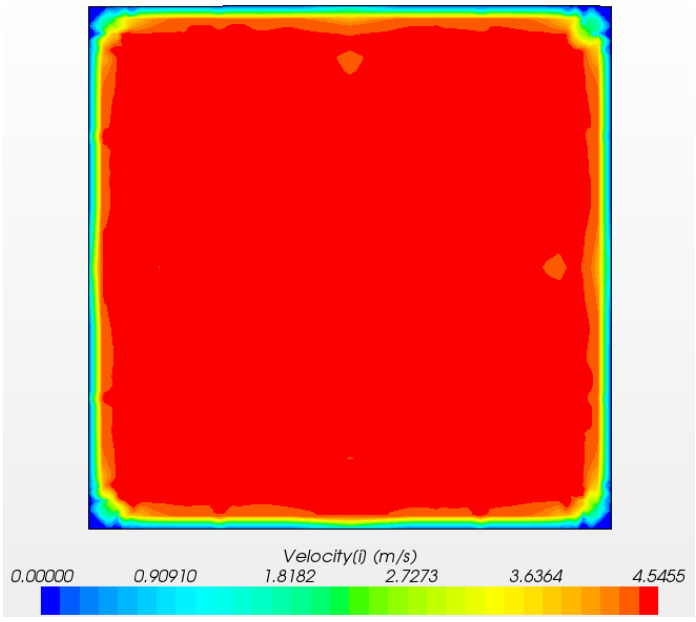

Fig. A.3: u velocity mapped onto the velocity inlet of the computational domain for the F1 validation case.

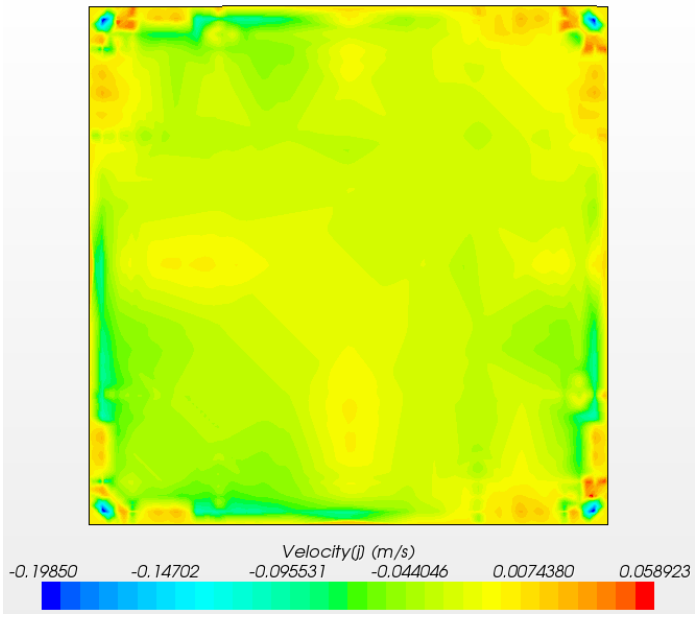

Fig. A.4: v and w velocity mapped onto the velocity inlet of the computational domain for the F1 validation case.

A.3 M2

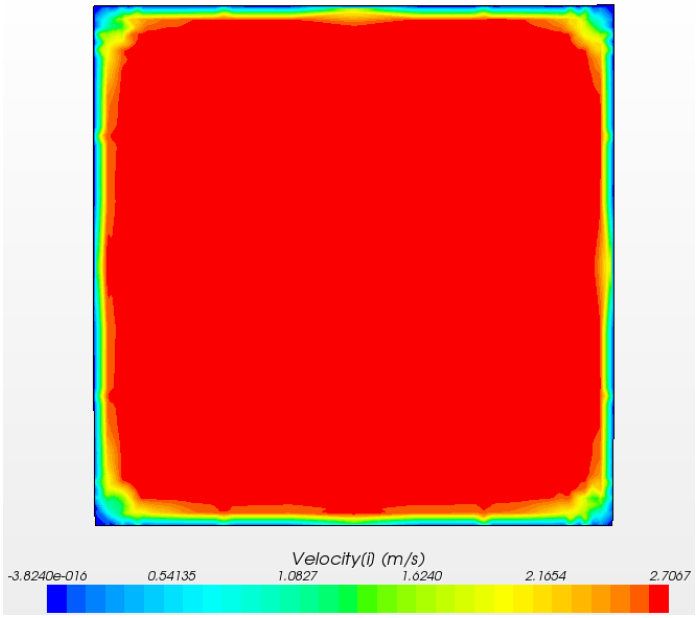

Fig. A.5: u velocity mapped onto the velocity inlet of the computational domain for the M2 validation case.

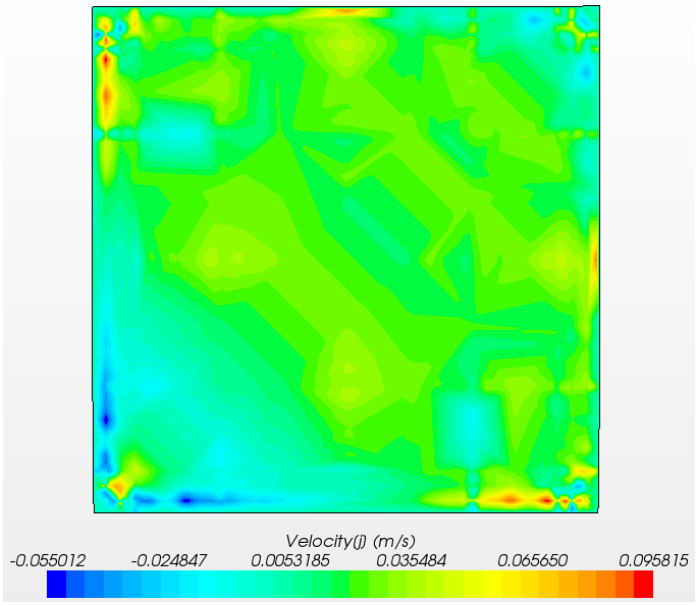

Fig. A.6: v and w velocity mapped onto the velocity inlet of the computational domain for the M2 validation case.

Appendix B

Inlet Turbulence Profiles

B.1 M1

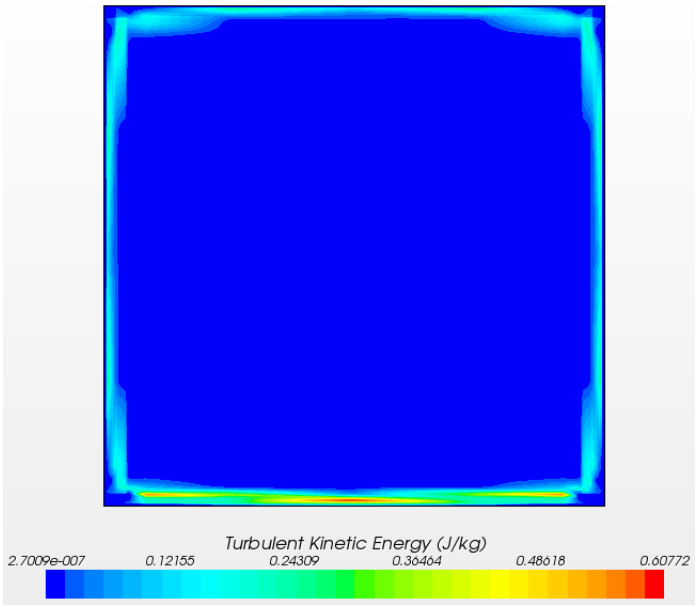

Fig. B.1: Turbulent kinetic energy (k) mapped onto the velocity inlet of the computational domain for the M1 validation case.

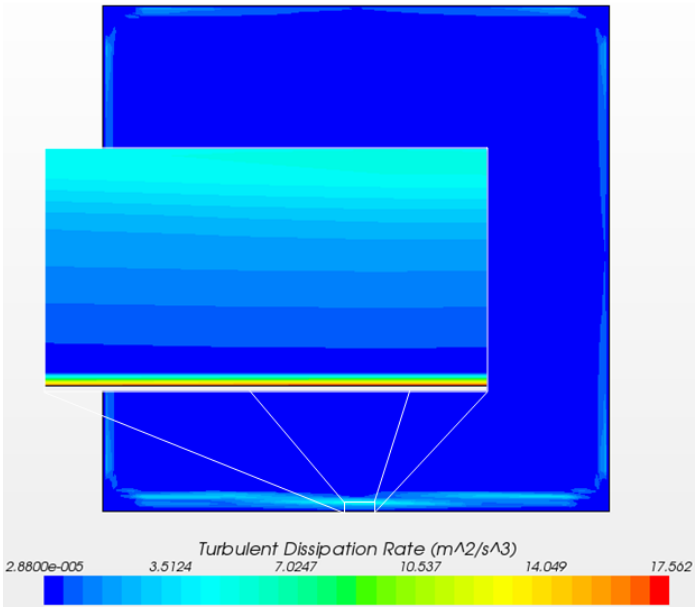

Fig. B.2: Turbulent dissipation rate (ε) mapped onto the velocity inlet of the computational domain for the M1 validation case.

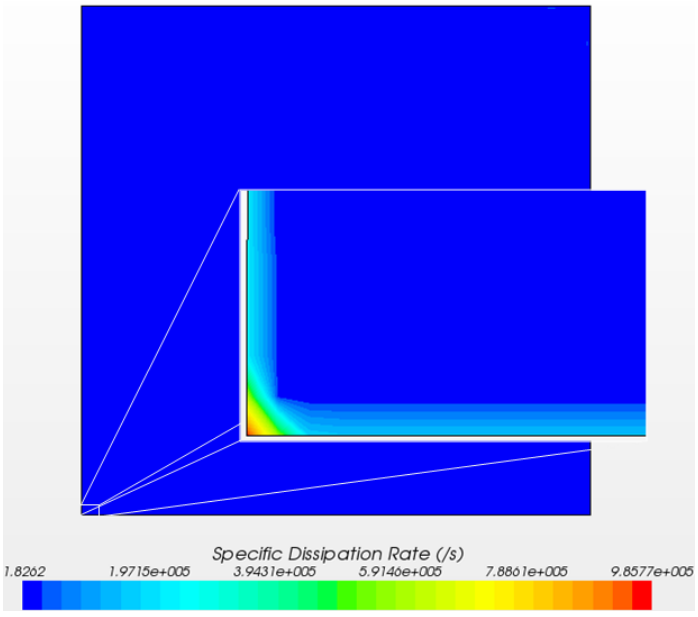

Fig. B.3: Specific turbulent dissipation rate (ω) mapped onto the velocity inlet of the computational domain for the M1 validation case.

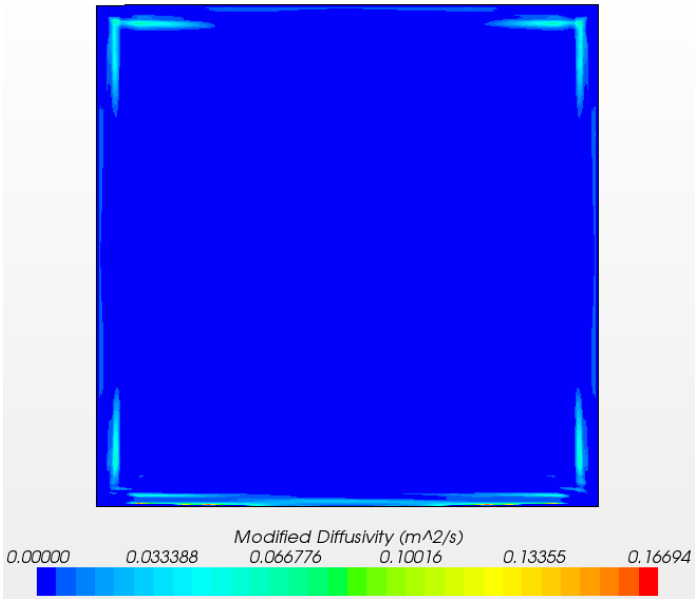

Fig. B.4: Modified turbulent diffusivity ($\tilde{\nu}$) mapped onto the velocity inlet of the computational domain for the M1 validation case.

B.2 M2

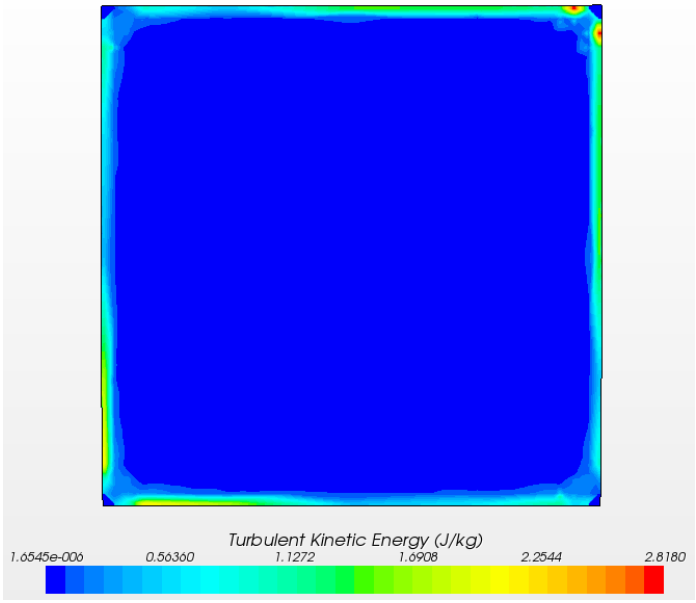

Fig. B.5: Turbulent kinetic energy (k) mapped onto the velocity inlet of the computational domain for the M2 validation case.

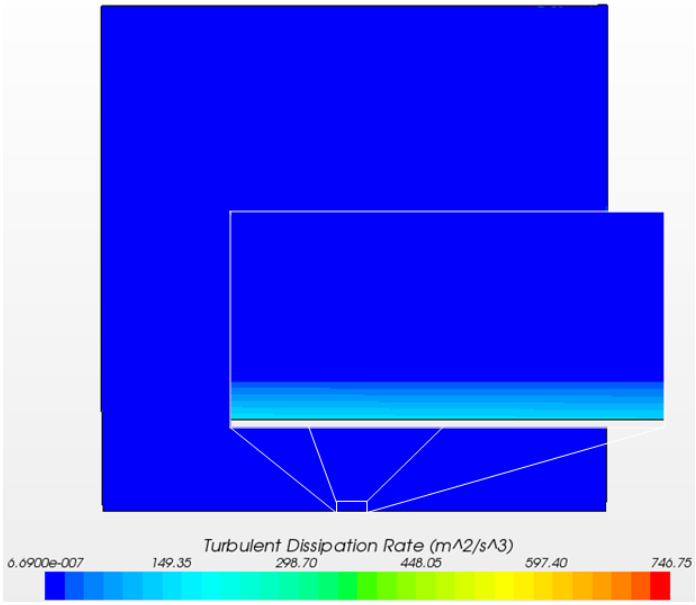

Fig. B.6: Turbulent dissipation rate (ε) mapped onto the velocity inlet of the computational domain for the M2 validation case.

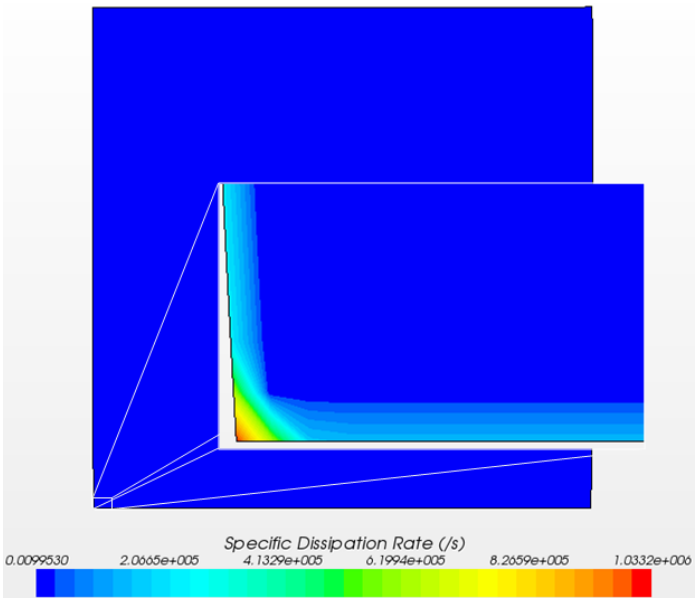

Fig. B.7: Specific turbulent dissipation rate (ω) mapped onto the velocity inlet of the computational domain for the M2 validation case.

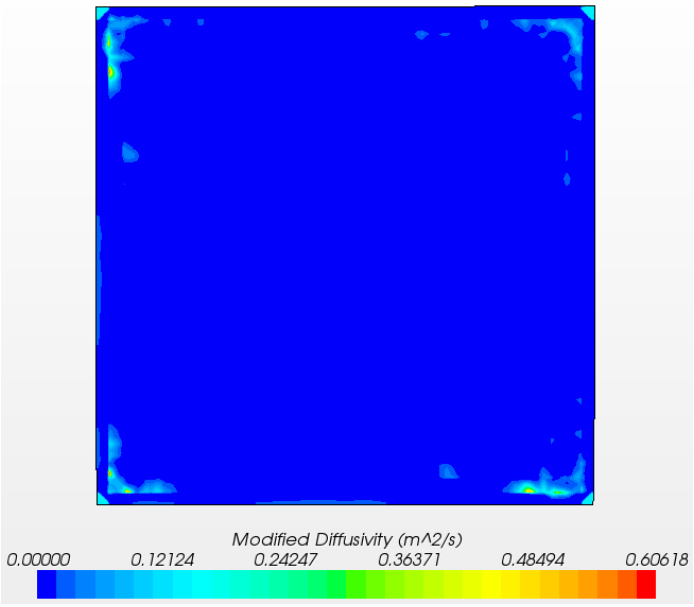

Fig. B.8: Modified turbulent diffusivity ($\tilde{\nu}$) mapped onto the velocity inlet of the computational domain for the M2 validation case.

B.3 F2

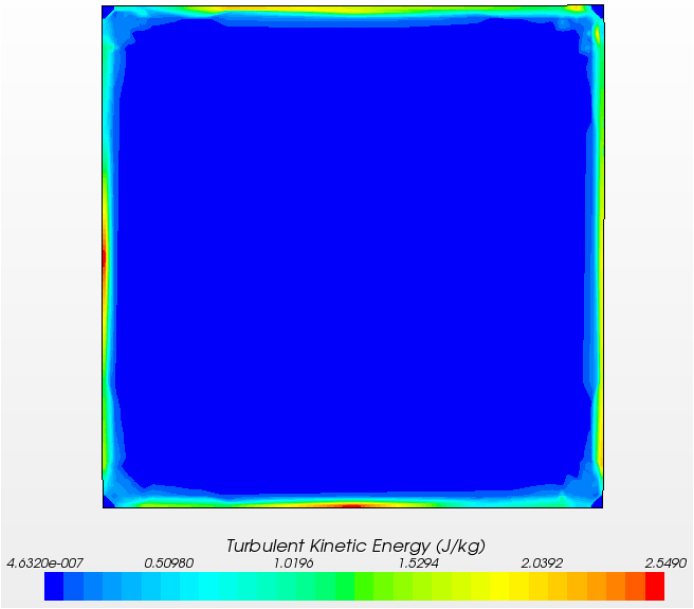

Fig. B.9: Turbulent kinetic energy (k) mapped onto the velocity inlet of the computational domain for the F2 validation case.

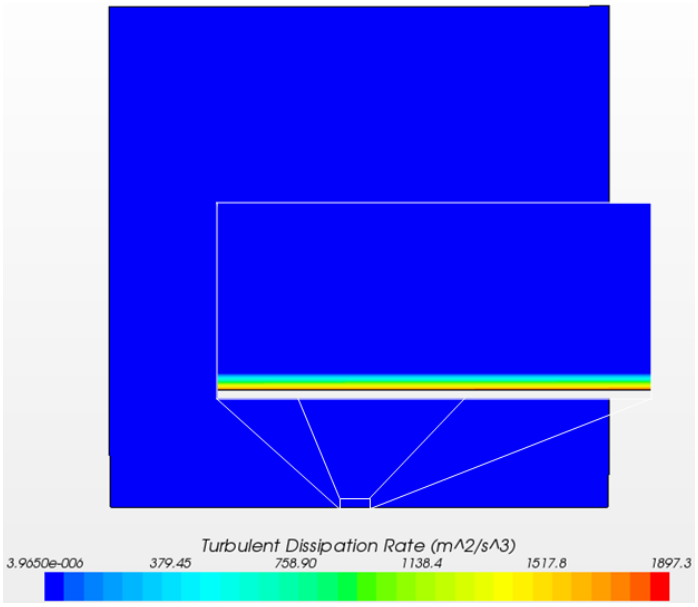

Fig. B.10: Turbulent dissipation rate (ε) mapped onto the velocity inlet of the computational domain for the F2 validation case.

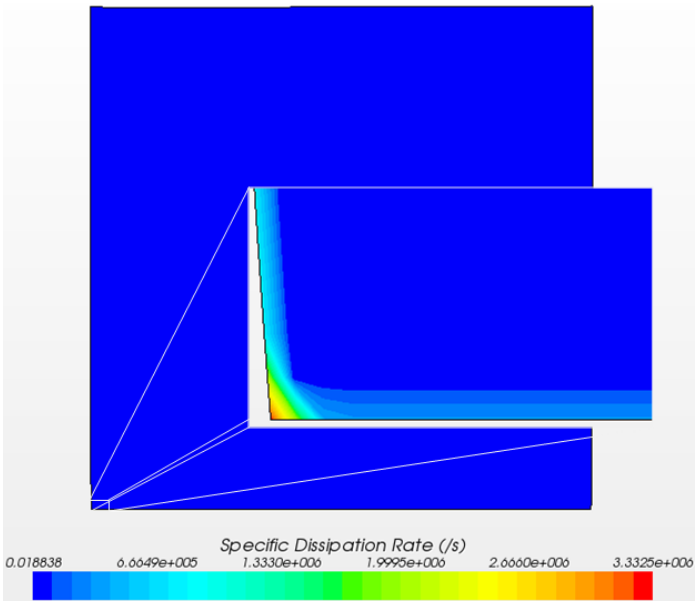

Fig. B.11: Specific turbulent dissipation rate (ω) mapped onto the velocity inlet of the computational domain for the F2 validation case.

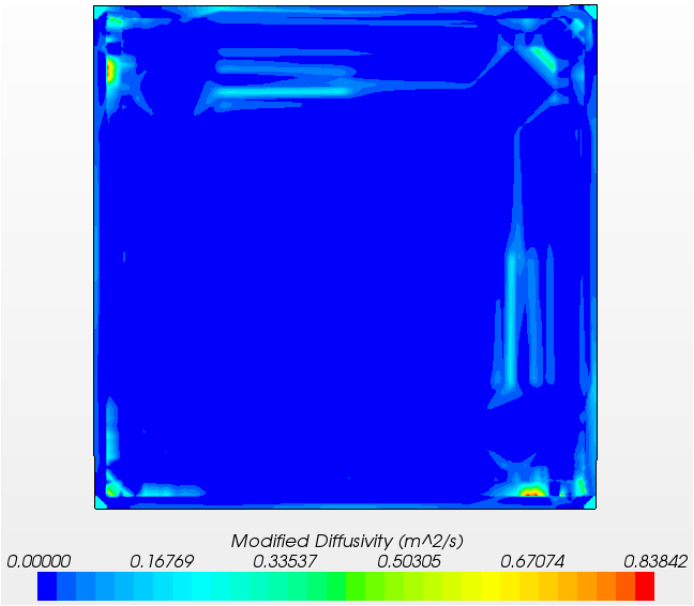

Fig. B.12: Modified turbulent diffusivity ($\tilde{\nu}$) mapped onto the velocity inlet of the computational domain for the F2 validation case.

Appendix C

Validation Results: HFS 2 & 3

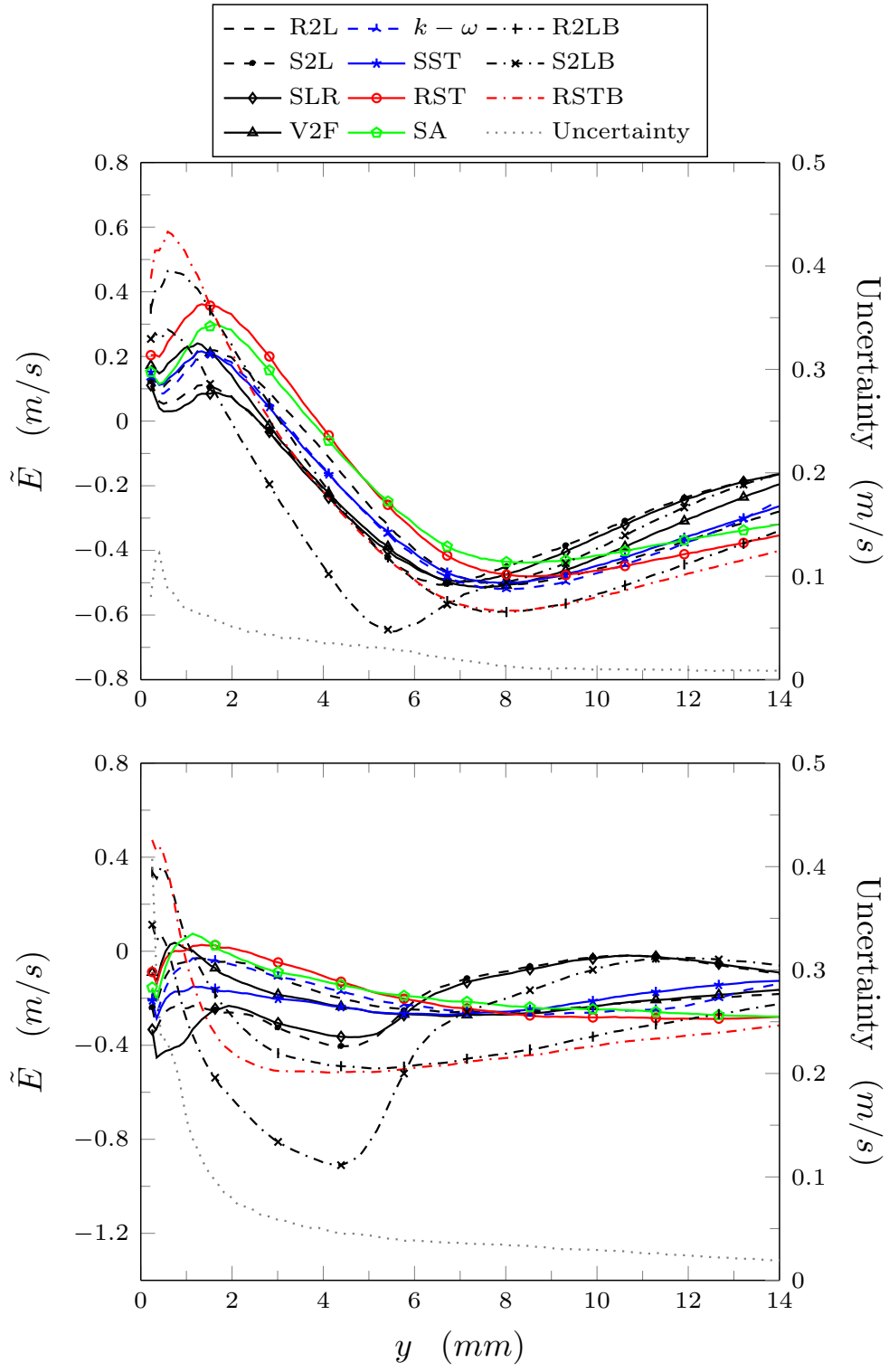

Fig. C.1: Streamwise velocity (u) error of each turbulence model for the M1 (top) and F1 (bottom) validation case at HFS location 1.

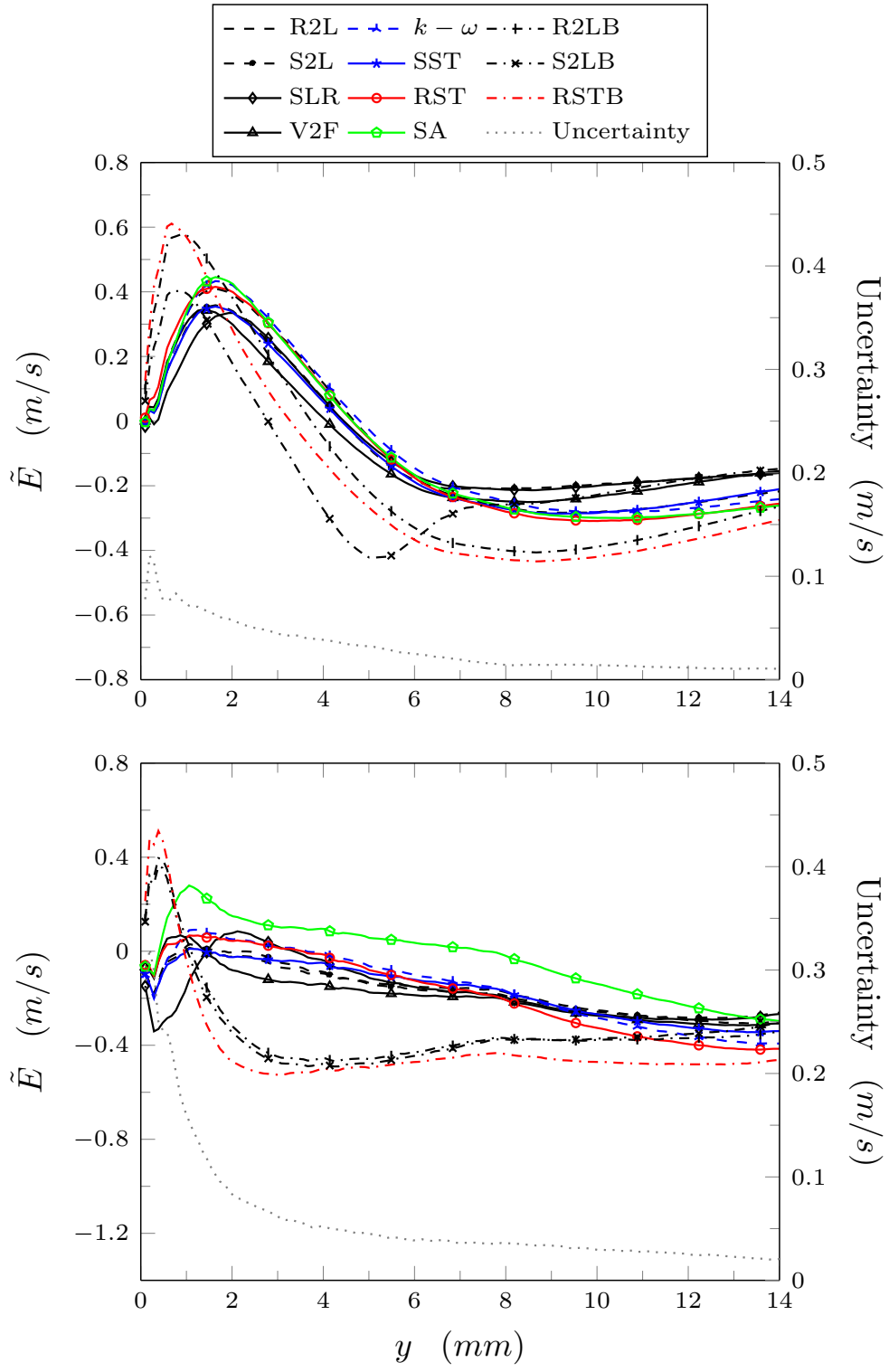

Fig. C.2: Streamwise velocity (u) error of each turbulence model for the M2 (top) and F2 (bottom) validation case at HFS location 1.

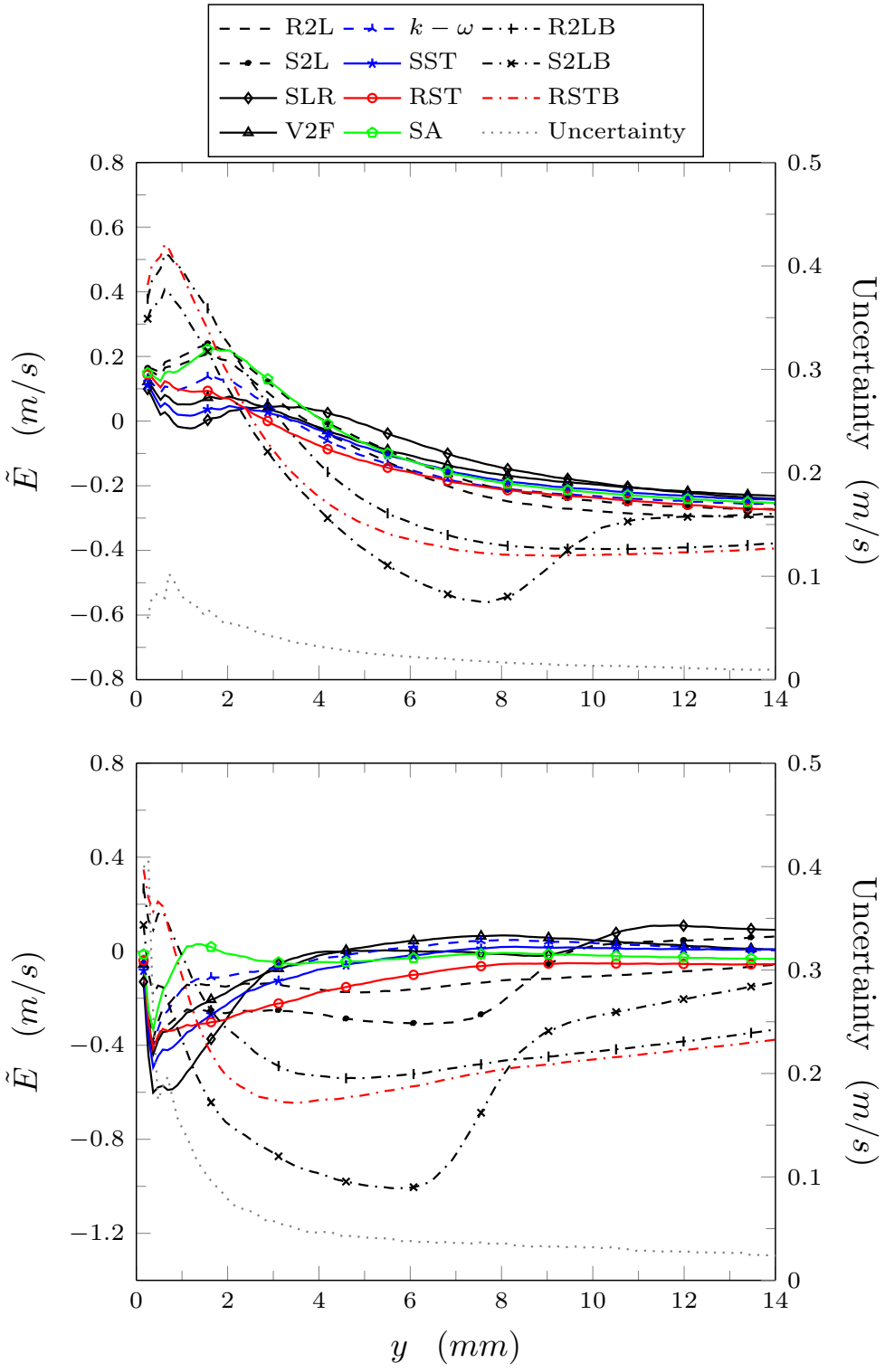

Fig. C.3: Streamwise velocity (u) error of each turbulence model for the M1 (top) and F1 (bottom) validation case at HFS location 2.

Table C.1: FULL Assessment: Relative error of u velocity for each turbulence model and validation case with 95% confidence indicator at the first HFS location.

	M1		F2		M2		F2	
Model	Average (%)	Maximum (%)	Average (%)	Maximum (%)	Average (%)	Maximum (%)	Average (%)	Maximum (%)
R2L	15.8 ± 3.4	173.8 ± 95.3	4.9 ± 1.9	18.5 ± 46.3	12.6 ± 3.0	42.0 ± 8.7	4.6 ± 2.2	24.3 ± 72.5
S2L	13.0 ± 3.4	144.8 ± 95.3	5.1 ± 1.9	27.3 ± 46.3	10.3 ± 3.0	36.8 ± 8.7	4.4 ± 2.2	23.6 ± 72.5
SLR	12.6 ± 3.4	131.8 ± 95.3	5.6 ± 1.9	37.8 ± 46.3	9.3 ± 3.0	29.3 ± 7.6	5.3 ± 2.2	38.1 ± 72.5
V2F	16.4 ± 3.4	205.1 ± 95.3	5.1 ± 1.9	10.7 ± 24.0	10.5 ± 3.0	38.5 ± 9.6	5.2 ± 2.2	17.1 ± 72.5
$k-\omega$	15.7 ± 3.4	161.0 ± 95.3	5.0 ± 1.9	22.8 ± 46.3	12.7 ± 3.0	42.4 ± 7.6	5.0 ± 2.2	26.0 ± 72.5
SST	15.8 ± 3.4	179.9 ± 95.3	5.7 ± 1.9	23.7 ± 46.3	11.5 ± 3.0	36.1 ± 8.7	4.7 ± 2.2	24.6 ± 72.5
RST	18.9 ± 3.4	242.9 ± 95.3	4.9 ± 1.9	11.5 ± 24.0	13.7 ± 3.0	44.9 ± 13.5	5.2 ± 2.2	15.3 ± 72.5
SA	15.8 ± 3.4	180.4 ± 95.3	4.9 ± 1.9	17.5 ± 46.3	13.2 ± 3.0	44.0 ± 7.6	4.0 ± 2.2	16.8 ± 72.5
R2LB	24.1 ± 3.4	414.0 ± 95.3	9.7 ± 1.9	38.3 ± 46.3	19.5 ± 3.0	123.1 ± 60.8	9.9 ± 2.2	44.8 ± 44.3
S2LB	19.9 ± 3.4	302.6 ± 95.3	9.2 ± 1.9	24.9 ± 1.3	14.1 ± 3.0	85.9 ± 60.8	9.7 ± 2.2	41.5 ± 44.3
RSTB	26.5 ± 3.4	524.6 ± 95.3	11.3 ± 1.9	53.7 ± 46.3	20.6 ± 3.0	149.7 ± 60.8	12.3 ± 2.2	65.9 ± 44.3

Table C.2: VSL Assessment: Relative error of u velocity for each turbulence model and validation case with 95% confidence indicator at the first HFS location.

	M1		F1		M2		F2	
Model	Average (%)	Maximum (%)	Average (%)	Maximum (%)	Average (%)	Maximum (%)	Average (%)	Maximum (%)
R2L	24.1 ± 9.7	23.9 ± 7.1	1.7 ± 5.6	2.9 ± 10.8	42.9 ± 9.7	42.0 ± 8.7	0.7 ± 7.1	2.7 ± 14.2
S2L	11.4 ± 9.7	12.1 ± 7.1	10.4 ± 5.6	12.1 ± 10.8	37.4 ± 9.7	36.8 ± 8.7	0.7 ± 7.1	1.9 ± 14.2
SLR	8.0 ± 9.7	8.9 ± 6.6	13.3 ± 5.6	20.9 ± 10.8	28.8 ± 9.7	29.3 ± 7.6	6.1 ± 7.1	16.9 ± 14.2
V2F	27.5 ± 9.7	34.4 ± 15.5	1.8 ± 5.6	3.4 ± 2.8	38.6 ± 9.7	38.5 ± 9.6	2.0 ± 7.1	3.2 ± 14.2
$k-\omega$	21.5 ± 9.7	21.9 ± 7.1	2.0 ± 5.6	4.6 ± 10.8	43.0 ± 9.7	42.4 ± 7.6	2.7 ± 7.1	3.6 ± 6.2
SST	23.9 ± 9.7	25.6 ± 15.5	6.9 ± 5.6	8.8 ± 10.8	36.9 ± 9.7	36.1 ± 8.7	0.8 ± 7.1	3.4 ± 14.2
RST	41.8 ± 9.7	47.7 ± 15.5	0.7 ± 5.6	1.0 ± 4.4	45.9 ± 9.7	44.9 ± 2.1	2.3 ± 7.1	2.7 ± 6.2
SA	30.8 ± 9.7	30.5 ± 7.1	1.7 ± 5.6	3.0 ± 5.5	44.6 ± 9.7	44.0 ± 7.6	10.1 ± 7.1	11.3 ± 6.2
R2LB	51.7 ± 9.7	84.9 ± 15.5	5.3 ± 5.6	11.4 ± 10.8	72.2 ± 9.7	106.8 ± 15.0	6.8 ± 7.1	20.6 ± 14.2
S2LB	24.4 ± 9.7	50.2 ± 15.5	16.8 ± 5.6	19.7 ± 2.8	48.4 ± 9.7	76.3 ± 15.0	6.8 ± 7.1	18.3 ± 14.2
RSTB	58.6 ± 9.7	105.3 ± 15.5	9.2 ± 5.6	13.4 ± 2.8	70.8 ± 9.7	117.9 ± 15.0	9.7 ± 7.1	23.0 ± 14.2

Table C.3: Heat flux results for each turbulence model and validation case with relative error ($\tilde{E}/\bar{y}_e$) and uncertainty at the first HFS location.

	M1			F1			M2			F2		
Model	y_m (W/m^2)	$\bar{y}_e$ (W/m^2)	$\tilde{E}/\bar{y}_e$ (%)	y_m (W/m^2)	$\bar{y}_e$ (W/m^2)	$\tilde{E}/\bar{y}_e$ (%)	y_m (W/m^2)	$\bar{y}_e$ (W/m^2)	$\tilde{E}/\bar{y}_e$ (%)	y_m (W/m^2)	$\bar{y}_e$ (W/m^2)	$\tilde{E}/\bar{y}_e$ (%)
R2L	1457.4	1113.1	30.9	2064.1	1759.5	17.3	1561.1	1149.3	35.8	2309.9	2020.7	14.3
S2L	1408.1		26.5	1972.8		12.1	1555.9		35.4	2351.9		16.4
SLR	1314.5		18.1	1683.8		-4.3	1392.9		21.2	1914.6		-5.3
V2F	1652.8		48.5	2272.7		29.2	1610.9		40.2	2516.7		24.5
$k-\omega$	1408.7		26.6	1960.3		11.4	1505.8		31.0	2249.5		11.3
SST	1492.3		34.1	1955.4		11.1	1504.7		30.9	2285.4		13.1
RST	1568.6		40.9	2152.2		22.3	1602.8		39.5	2402.1		18.9
SA	1440.6		29.4	2033.1		15.5	1518.0		32.1	2412.6		19.4
R2LB	2920.7		162.4	4088.8		132.4	3138.4		173.1	4497.5		122.6
S2LB	2399.0		115.5	3431.8		95.0	2642.8		130.0	4444.6		120.0
RSTB	3037.7		172.9	4164.2		136.7	3156.7		174.7	4584.4		126.9
Uncertainty		± 22.8	± 2.0		± 35.3	± 2.0		± 23.0	± 2.0		± 40.4	± 2.0

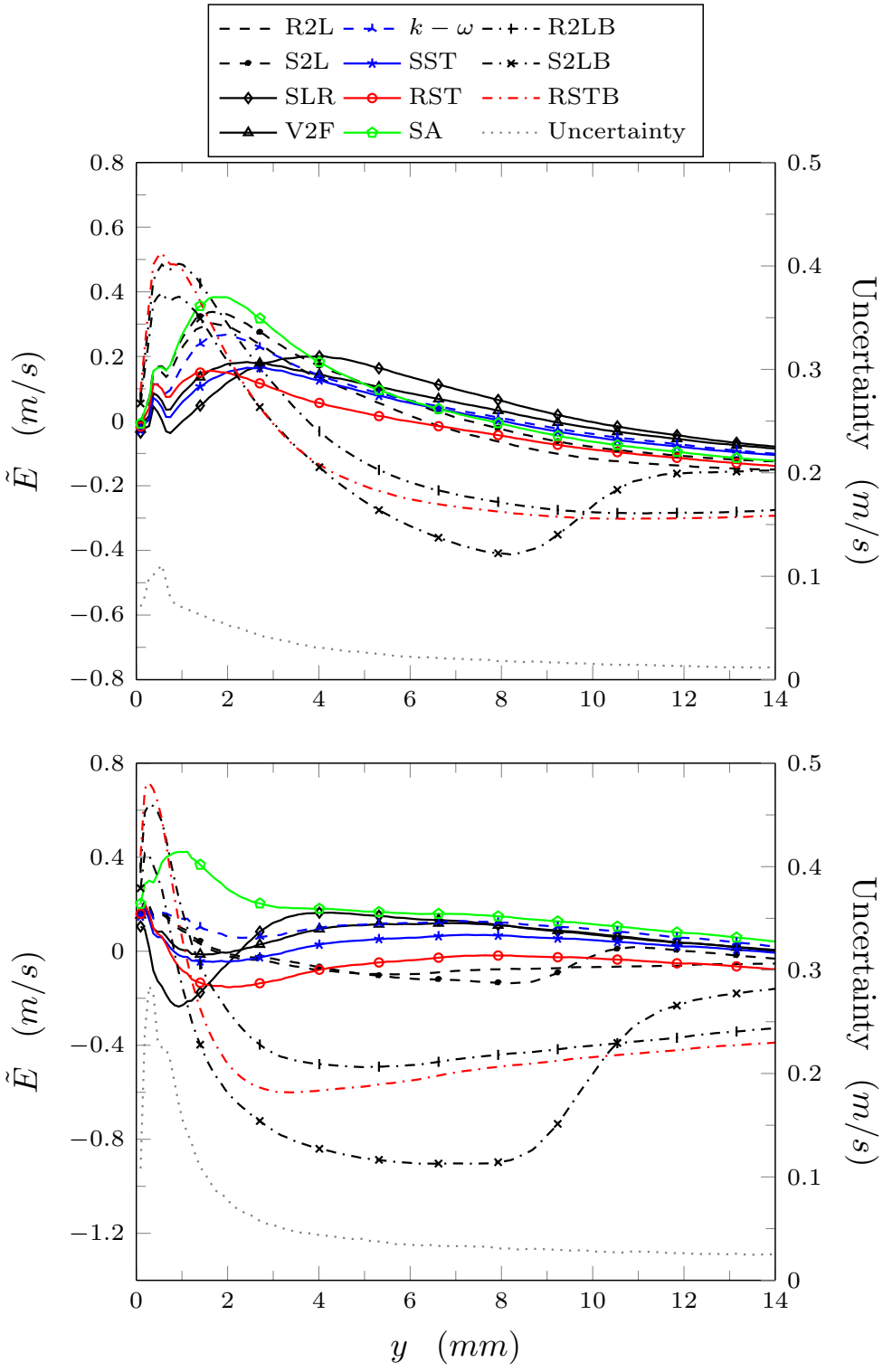

Fig. C.4: Streamwise velocity (u) error of each turbulence model for the M2 (top) and F2 (bottom) validation case at HFS location 2.

Table C.4: FULL Assessment: Relative error of u velocity for each turbulence model and validation case with 95% confidence indicator at the second HFS location.

	M1		F1		M2		F2	
Model	Average (%)	Maximum (%)	Average (%)	Maximum (%)	Average (%)	Maximum (%)	Average (%)	Maximum (%)
R2L	11.8 ± 2.6	167.1 ± 63.2	3.9 ± 2.2	32.1 ± 47.0	8.6 ± 2.9	56.5 ± 39.3	3.6 ± 3.3	237.1 ± 154.9
S2L	11.5 ± 2.6	174.4 ± 63.2	5.6 ± 2.2	36.3 ± 47.0	9.0 ± 2.9	61.3 ± 39.3	3.5 ± 3.3	239.6 ± 154.9
SLR	6.1 ± 2.6	106.1 ± 63.2	4.3 ± 2.2	51.0 ± 47.0	5.0 ± 2.9	31.6 ± 63.0	3.7 ± 3.3	150.8 ± 154.9
V2F	7.4 ± 2.6	130.7 ± 63.2	2.7 ± 2.2	37.2 ± 47.0	5.2 ± 2.9	33.5 ± 39.3	3.2 ± 3.3	220.5 ± 154.9
$k-\omega$	9.5 ± 2.6	140.2 ± 63.2	2.0 ± 2.2	34.7 ± 47.0	6.7 ± 2.9	44.1 ± 39.3	4.1 ± 3.3	232.1 ± 154.9
SST	7.3 ± 2.6	118.6 ± 63.2	3.0 ± 2.2	42.0 ± 47.0	4.7 ± 2.9	27.9 ± 39.3	2.4 ± 3.3	211.3 ± 154.9
RST	9.6 ± 2.6	153.9 ± 63.2	4.3 ± 2.2	34.8 ± 21.6	5.4 ± 2.9	44.5 ± 39.3	3.4 ± 3.3	228.0 ± 154.9
SA	10.5 ± 2.6	159.3 ± 63.2	1.4 ± 2.2	28.7 ± 47.0	9.3 ± 2.9	60.1 ± 39.3	7.2 ± 3.3	289.3 ± 154.9
R2LB	21.6 ± 2.6	405.1 ± 63.2	11.4 ± 2.2	69.3 ± 103.5	17.5 ± 2.9	168.5 ± 39.3	15.4 ± 3.3	507.4 ± 154.9
S2LB	20.7 ± 2.6	33.9 ± 63.2	14.3 ± 2.2	29.1 ± 1.2	15.8 ± 2.9	141.1 ± 39.3	18.7 ± 3.3	383.7 ± 154.9
RSTB	23.0 ± 2.6	450.7 ± 63.2	13.5 ± 2.2	90.0 ± 103.5	18.4 ± 2.9	187.9 ± 39.3	18.2 ± 3.3	579.4 ± 154.9

Table C.5: VSL Assessement: Relative error of u velocity for each turbulence model and validation case with 95% confidence indicator at the second HFS location.

	M1		F1		M2		F2	
Model	Average (%)	Maximum (%)	Average (%)	Maximum (%)	Average (%)	Maximum (%)	Average (%)	Maximum (%)
R2L	23.8 ± 9.9	32.7 ± 19.8	7.7 ± 6.2	13.8 ± 11.8	30.8 ± 10.4	34.1 ± 25.0	4.7 ± 9.0	13.4 ± 19.2
S2L	27.1 ± 9.9	36.4 ± 19.8	12.7 ± 6.2	18.9 ± 11.8	34.8 ± 10.4	38.3 ± 25.0	5.3 ± 9.0	14.1 ± 19.2
SLR	1.7 ± 9.9	2.9 ± 19.8	22.5 ± 6.2	35.5 ± 11.8	4.2 ± 10.4	6.6 ± 5.5	10.9 ± 9.0	13.7 ± 13.6
V2F	7.7 ± 9.9	14.2 ± 19.8	12.2 ± 6.2	20.5 ± 11.8	12.4 ± 10.4	14.2 ± 5.5	1.5 ± 9.0	7.2 ± 19.2
$k-\omega$	14.5 ± 9.9	20.3 ± 19.8	7.1 ± 6.2	15.3 ± 11.8	23.5 ± 10.4	24.5 ± 6.9	7.4 ± 9.0	13.9 ± 19.2
SST	3.5 ± 9.9	8.9 ± 19.8	15.7 ± 6.2	25.3 ± 11.8	8.7 ± 10.4	11.5 ± 5.5	1.8 ± 9.0	5.1 ± 19.2
RST	12.1 ± 9.9	22.8 ± 19.8	15.1 ± 6.2	20.4 ± 11.8	16.4 ± 10.4	22.5 ± 25.0	4.6 ± 9.0	5.6 ± 4.2
SA	23.5 ± 9.9	29.7 ± 19.8	1.6 ± 6.2	8.0 ± 11.8	36.9 ± 10.4	37.6 ± 25.0	22.0 ± 9.0	32.2 ± 19.2
R2LB	53.5 ± 9.9	99.1 ± 19.8	7.0 ± 6.2	11.0 ± 3.2	64.0 ± 10.4	109.3 ± 25.0	12.9 ± 9.0	47.1 ± 19.2
S2LB	37.4 ± 9.9	77.0 ± 19.8	23.2 ± 6.2	25.7 ± 3.2	49.7 ± 10.4	89.6 ± 25.0	13.2 ± 9.0	22.5 ± 19.2
RSTB	49.7 ± 9.9	103.0 ± 19.8	12.2 ± 6.2	18.3 ± 3.2	61.7 ± 10.4	117.6 ± 25.0	14.4 ± 9.0	48.0 ± 19.2

Table C.6: Heat flux results for each turbulence model and validation case with relative error ($\tilde{E}/\bar{y}_e$) and uncertainty at the second HFS location.

	M1			F1		
Model	y_m (W/m^2)	$\bar{y}_e$ (W/m^2)	$\tilde{E}/\bar{y}_e$ (%)	y_m (W/m^2)	$\bar{y}_e$ (W/m^2)	$\tilde{E}/\bar{y}_e$ (%)
R2L	966.7	583.8	65.6	1456.5	1220.9	19.3
S2L	1005.8		72.3	1356.7		11.1
SLR	676.9		16.0	1040.2		-14.8
V2F	756.4		29.6	1320.9		8.2
$k-\omega$	833.9		42.8	1391.6		14.0
SST	716.9		22.8	1228.5		0.6
RST	948.3		62.4	1457.4		20.8
SA	292.0		59.1	1521.3		24.6
R2LB	1920.4		229.0	2724.1		123.1
S2LB	1556.2		166.6	1953.0		60.0
RSTB	1953.5		234.6	2844.0		132.9
Uncertainty		± 12.2	± 2.1		± 27.6	± 2.3

Appendix D

GCI Results: HFS 2 & 3

Table D.1: M1 GCI method results for grid refinement of the heat flux at the first HFS.

Parameter	R2L	S2L	SLR	V2F	$k-\omega$	SST	RST	SA	R2LB	S2LB	RSTB
ϕ_1 (W/m^2)	1457.4	1408.1	1314.5	1652.8	1408.7	1492.3	1568.6	1440.6	2920.7	2399.0	3037.7
ϕ_2 (W/m^2)	1456.0	1420.8	1332.1	1652.9	1408.8	1489.3	1566.4	1440.2	2917.4	2491.9	3034.4
ϕ_3 (W/m^2)	1456.9	1427.7	1344.9	1656.3	1411.1	1486.9	1565.3	1438.5	2921.0	2559.9	3029.9
p	0.70	0.92	0.47	5.63	8.00	0.31	1.25	2.17	0.12	0.46	0.54
ϕ_{ext}^{21}	1460.1	1391.4	1261.9	1652.8	1408.7	1506.3	1570.6	1440.8	2965.2	2114.7	3046.1
e_a^{21}	0.10%	0.90%	1.34%	0.01%	0.00%	0.20%	0.14%	0.03%	0.12%	3.87%	0.11%
e_{ext}^{21}	0.18%	1.20%	4.17%	0.00%	0.00%	0.93%	0.13%	0.01%	1.50%	13.44%	0.28%
GCI_{fine}^{21}	0.23%	1.48%	5.00%	0.00%	0.00%	1.17%	0.16%	0.01%	1.90%	14.81%	0.35%
Convergence*	O	M	M	M	M	M	M	M	O	M	M

* Note: M and O denote monotonic and oscillatory convergence, respectively.

Table D.2: F1 GCI method results for grid refinement of the heat flux at the first HFS.

Parameter	R2L	S2L	SLR	V2F	$k-\omega$	SST	RST	SA	R2LB	S2LB	RSTB
ϕ_1 (W/m^2)	2064.1	1972.8	1683.8	2272.7	1960.3	1955.4	2152.2	2033.1	4088.8	3431.8	4164.2
ϕ_2 (W/m^2)	2062.9	1998.4	1716.7	2268.5	1961.6	1955.7	2147.9	2037.6	4080.5	3564.9	4159.3
ϕ_3 (W/m^2)	2061.3	2007.4	1747.1	2278.2	1965.0	1959.2	2150.7	2043.0	4073.5	3649.3	4165.9
p	0.50	1.64	0.10	1.38	1.62	4.42	0.69	0.35	0.26	0.71	0.49
ϕ_{ext}^{21}	2067.6	1958.3	1152.8	2275.8	1959.5	1955.4	2160.5	2014.7	4136.1	3187.7	4177.8
e_a^{21}	0.06%	1.29%	1.95%	0.19%	0.07%	0.01%	0.20%	0.22%	0.20%	3.88%	0.12%
e_{ext}^{21}	0.17%	0.74%	46.06%	0.14%	0.04%	0.00%	0.38%	0.91%	1.14%	7.66%	0.33%
GCI_{fine}^{21}	0.21%	0.92%	39.42%	0.17%	0.05%	0.00%	0.48%	1.13%	1.45%	8.89%	0.41%
Convergence*	M	M	M	O	M	M	O	M	M	M	O

* Note: M and O denote monotonic and oscillatory convergence, respectively.

Table D.3: M2 GCI method results for grid refinement of the heat flux at the first HFS.

Parameter	R2L	S2L	SLR	V2F	$k-\omega$	SST	RST	SA	R2LB	S2LB	RSTB
ϕ_1 (W/m^2)	1561.1	1555.9	1392.9	1610.9	1505.8	1504.7	1602.8	1518.0	3138.4	2642.8	3156.7
ϕ_2 (W/m^2)	1559.6	1574.2	1411.8	1613.5	1502.4	1502.2	1602.5	1518.9	3135.1	2738.5	3152.1
ϕ_3 (W/m^2)	1558.1	1582.4	1429.2	1617.6	1503.7	1503.7	1603.8	1527.2	3127.3	2848.4	3152.1
p	0.0027	1.24	0.09	0.86	1.59	1.29	2.24	3.64	1.44	0.28	13.22
ϕ_{ext}^{21}	2483.6	1540.0	1073.7	1607.3	1507.9	1506.7	1602.9	1517.8	3140.8	2133.8	3156.7
e_a^{21}	0.10%	1.18%	1.36%	0.16%	0.23%	0.17%	0.02%	0.06%	0.11%	3.62%	0.15%
e_{ext}^{21}	37.14%	1.03%	29.72%	0.22%	0.14%	0.14%	0.01%	0.01%	0.07%	23.86%	0.00%
GCI_{fine}^{21}	73.86%	1.27%	28.64%	0.28%	0.17%	0.17%	0.01%	0.01%	0.09%	24.08%	0.00%
Convergence*	M	M	M	M	O	O	O	M	M	M	O

* Note: M and O denote monotonic and oscillatory convergence, respectively.

Table D.4: F2 GCI method results for grid refinement of the heat flux at the first HFS.

Parameter	R2L	S2L	SLR	V2F	$k-\omega$	SST	RST	SA	R2LB	S2LB	RSTB
ϕ_1 (W/m^2)	2309.9	2351.9	1914.6	2516.7	2249.5	2285.4	2402.1	2412.6	4497.5	4444.6	4584.4
ϕ_2 (W/m^2)	2300.7	2346.8	1916.4	2512.5	2241.9	2273.2	2396.0	2409.7	4479.2	4447.6	4578.9
ϕ_3 (W/m^2)	2295.6	2339.5	1930.4	2518.1	2239.1	2264.9	2401.3	2408.3	4466.9	4421.8	4588.4
p	0.92	0.61	3.37	0.46	1.56	0.58	0.23	1.09	0.58	3.55	0.89
ϕ_{ext}^{21}	2321.9	2363.1	1914.3	2529.3	2254.1	2313.7	2441.5	2415.6	4539.4	4444.3	4591.7
e_a^{21}	0.40%	0.22%	0.09%	0.17%	0.34%	0.54%	0.25%	0.12%	0.41%	0.07%	0.12%
e_{ext}^{21}	0.52%	0.47%	0.01%	0.50%	0.21%	1.22%	1.62%	0.12%	0.92%	0.01%	0.16%
GCI_{fine}^{21}	0.65%	0.59%	0.02%	0.63%	0.26%	1.55%	2.05%	0.15%	1.16%	0.01%	0.20%
Convergence*	M	M	M	O	M	M	O	M	M	O	O

* Note: M and O denote monotonic and oscillatory convergence, respectively.

Table D.5: Global GCI method results for grid refinement of the u velocity profile at the first HFS.

Case	Parameter	R2L	S2L	SLR	V2F	$k-\omega$	SST	RST	SA	R2LB	S2LB	RSTB
M1	p_{local} (Min -Max)	0.0 -8.0	0.0 -7.4	0.0 -6.5	0.0 -10.2	0.0 -6.6	0.0 -7.0	0.0 -9.4	0.0 -8.2	0.0 -7.2	0.0 -8.4	0.0 -8.4
	p_{avg}	3.14	2.87	2.92	2.98	2.94	3.05	3.43	2.72	3.06	3.10	3.21
	Max GCI_{fine} (%)	0.08	0.38	0.46	0.09	0.09	0.08	0.05	0.12	0.06	0.83	0.03
	Osc. Convergence (%)	79.86	78.86	78.29	79.29	78.14	79.57	57.71	61.71	80.71	71.14	51.71
F1	p_{local} (Min -Max)	0.0 -7.4	0.0 -9.6	0.0 -7.9	0.0 -8.0	0.0 -8.3	0.0 -7.7	0.0 -11.7	0.0 -7.7	0.0 -6.5	0.0 -7.9	0.0 -8.6
	p_{avg}	2.19	1.60	1.47	2.16	1.88	2.03	1.94	2.48	2.10	1.23	1.97
	Max GCI_{fine} (%)	0.13	1.62	2.48	0.11	0.29	0.25	0.12	0.23	0.06	4.71	0.09
	Osc. Convergence (%)	46.43	21.29	16.71	45.57	35.43	39	42	51.71	44.86	14.57	44
M2	p_{local} (Min -Max)	0.0 -8.9	0.0 -8.8	0.0 -4.3	0.0 -11.1	0.0 -6.2	0.0 -6.8	0.0 -6.9	0.0 -6.7	0.0 -6.9	0.0 -7.2	0.0 -7.9
	p_{avg}	1.14	1.58	0.98	1.70	1.62	1.60	1.48	1.77	1.40	0.38	1.55
	Max GCI_{fine} (%)	23.72	13.95	30.72	12.08	15.06	14.63	14.91	12.77	8.74	37.63	5.43
	Osc. Convergence (%)	7.86	10.71	1.43	31	25.86	24.29	26.43	23.14	10.43	1.29	26.29
F2	p_{local} (Min -Max)	0.0 -8.0	0.0 -5.3	0.0 -5.5	0.0 -7.7	0.0 -7.5	0.0 -6.9	0.0 -6.4	0.0 -8.1	0.0 -7.9	0.0 -6.5	0.0 -5.3
	p_{avg}	1.66	0.86	0.86	2.25	1.77	1.80	0.89	1.22	1.88	0.88	1.00
	Max GCI_{fine} (%)	0.37	1.04	1.23	0.17	0.31	0.39	0.46	0.29	0.46	0.46	0.23
	Osc. Convergence (%)	12.71	7.71	8.29	34.57	29.71	32	9.71	13	18.86	8	12.29

Table D.6: M1 GCI method results for grid refinement of the heat flux at the second HFS.

Parameter	R2L	S2L	SLR	V2F	$k-\omega$	SST	RST	SA	R2LB	S2LB	RSTB
ϕ_1 (W/m^2)	966.7	1005.8	676.9	756.4	833.9	716.9	948.3	929.0	1920.4	1556.2	1953.5
ϕ_2 (W/m^2)	964.0	1005.8	677.2	757.7	833.4	718.8	946.9	928.1	1917.0	1744.4	1953.5
ϕ_3 (W/m^2)	962.0	1005.5	681.7	759.9	835.4	715.2	944.0	927.2	1914.7	1957.6	1954.9
p	0.36	2.63	4.97	1.03	2.29	1.10	1.23	0.03	0.61	0.24	8.14
ϕ_{ext}^{21}	977.3	1005.9	676.9	755.0	834.1	715.0	949.5	974.6	1928.0	392.8	1953.5
e_a^{21}	0.27%	0.01%	0.03%	0.16%	0.06%	0.26%	0.15%	0.10%	0.18%	12.10%	0.00%
e_{ext}^{21}	1.09%	0.00%	0.00%	0.19%	0.02%	0.27%	0.13%	4.68%	0.39%	296.15%	0.00%
GCI_{fine}^{21}	1.38%	0.00%	0.00%	0.23%	0.03%	0.34%	0.16%	6.14%	0.49%	93.45%	0.00%
Convergence*	M	M	M	M	O	O	M	M	M	M	M

* Note: M and O denote monotonic and oscillatory convergence, respectively.

Table D.7: F1 GCI method results for grid refinement of the heat flux at the second HFS.

Parameter	R2L	S2L	SLR	V2F	$k-\omega$	SST	RST	SA	R2LB	S2LB	RSTB
ϕ_1 (W/m^2)	1456.5	1356.7	1040.2	1320.9	1391.6	1228.5	1475.4	1521.3	2724.1	1953.0	2844.0
ϕ_2 (W/m^2)	1452.4	1477.4	1096.4	1321.0	1392.1	1213.8	1476.3	1542.4	2721.4	2169.2	2848.5
ϕ_3 (W/m^2)	1447.0	1536.7	1101.4	1324.5	1391.9	1240.2	1477.3	1545.8	2717.8	2485.0	2849.9
p	0.51	1.12	3.84	5.33	1.21	0.95	0.37	2.93	0.48	0.65	1.92
ϕ_{ext}^{21}	1467.3	1235.0	1034.4	1320.9	1391.2	1247.0	1472.0	1517.1	2731.9	1511.9	2842.0
e_a^{21}	0.28%	8.90%	5.40%	0.01%	0.04%	1.20%	0.06%	1.39%	0.10%	11.07%	0.16%
e_{ext}^{21}	0.74%	9.85%	0.56%	0.00%	0.03%	1.48%	0.23%	0.27%	0.29%	29.18%	0.07%
GCI_{fine}^{21}	0.93%	11.21%	0.70%	0.00%	0.04%	1.87%	0.29%	0.34%	0.36%	28.23%	0.09%
Convergence*	M	M	M	M	O	O	M	M	M	M	M

* Note: M and O denote monotonic and oscillatory convergence, respectively.

Table D.8: Global GCI method results for grid refinement of the u velocity profile at the second HFS.

Case	Parameter	R2L	S2L	SLR	V2F	$k-\omega$	SST	RST	SA	R2LB	S2LB	RSTB
M1	p_{local} (Min -Max)	0.0 -8.2	0.0 -6.9	0.0 -6.9	0.0 -6.6	0.0 -6.0	0.0 -7.6	0.0 -10.2	0.0 -6.8	0.1 -6.9	0.0 -6.8	0.2 -7.5
	p_{avg}	3.19	2.59	2.51	2.54	2.82	3.10	3.76	3.15	3.24	1.01	3.54
	Max GCI_{fine} (%)	0.08	0.11	0.09	0.10	0.08	0.09	0.03	0.07	0.05	11.03	0.02
	Osc. Convergence (%)	86.71	54.14	58.43	59.57	78.86	81.43	86.86	77.43	90	11.71	92.86
F1	p_{local} (Min -Max)	0.0 -7.0	0.0 -8.4	0.0 -10.9	0.0 -6.1	0.0 -7.5	0.0 -7.6	0.0 -8.0	0.0 -7.4	0.0 -6.9	0.1 -8.4	0.0 -6.9
	p_{avg}	2.12	1.86	2.04	2.86	2.67	2.65	1.62	2.82	2.44	0.95	1.73
	Max GCI_{fine} (%)	0.13	4.75	2.62	0.08	0.12	0.31	0.28	0.43	0.04	15.71	0.19
	Osc. Convergence (%)	47.71	35.57	36.57	71.86	57.14	58.57	18.29	49.14	64	8	25.29
M2	p_{local} (Min -Max)	0.0 -7.8	0.0 -6.4	0.0 -6.0	0.0 -6.3	0.0 -6.7	0.0 -7.1	0.0 -7.5	0.0 -7.5	0.0 -7.7	0.0 -8.8	0.0 -8.4
	p_{avg}	1.83	2.12	2.23	2.10	2.33	2.79	2.55	2.07	3.18	1.25	2.76
	Max GCI_{fine} (%)	0.23	0.15	0.17	0.13	0.13	0.10	0.06	0.35	0.05	8.37	0.03
	Osc. Convergence (%)	18.86	33.43	47.86	44.14	43.71	60	37.86	48	71.29	16	41.57
F2	p_{local} (Min -Max)	0.0 -9.5	0.0 -9.2	0.0 -9.0	0.0 -7.4	0.0 -8.5	0.0 -6.5	0.0 -7.4	0.0 -6.9	0.0 -4.8	0.0 -6.8	0.0 -7.4
	p_{avg}	2.55	0.87	0.53	2.00	2.04	1.98	1.70	1.55	1.85	0.93	1.93
	Max GCI_{fine} (%)	0.15	5.0	3.30	0.13	0.11	0.57	0.13	0.29	0.10	22.77	0.04
	Osc. Convergence (%)	41.71	3.86	9.29	45.57	37.71	37.57	31.43	25.71	41.43	7.29	27.86

Appendix E

Examples of Converged Residuals

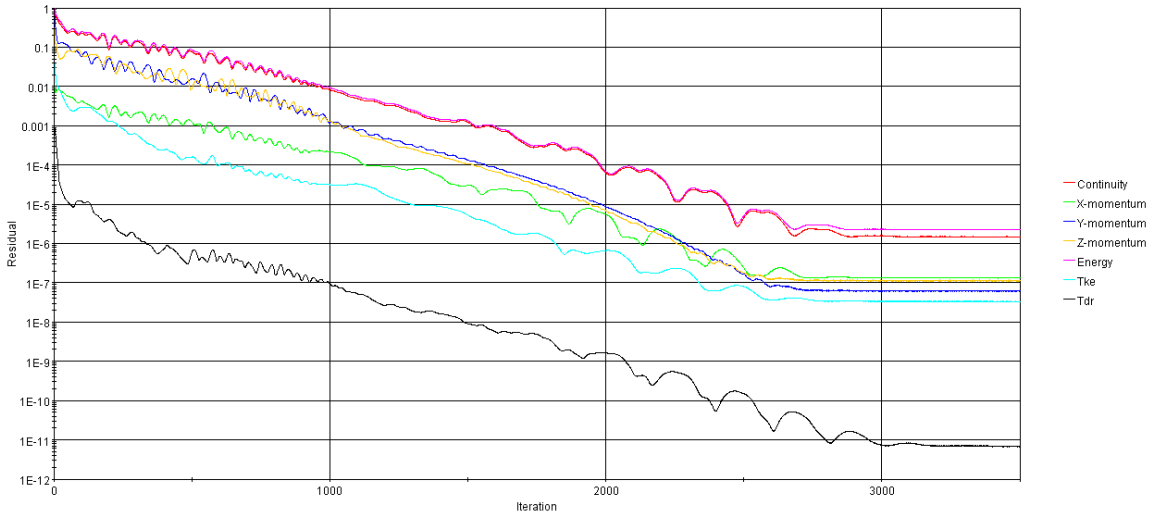

Fig. E.1: Converged residuals of the R2L simulation.

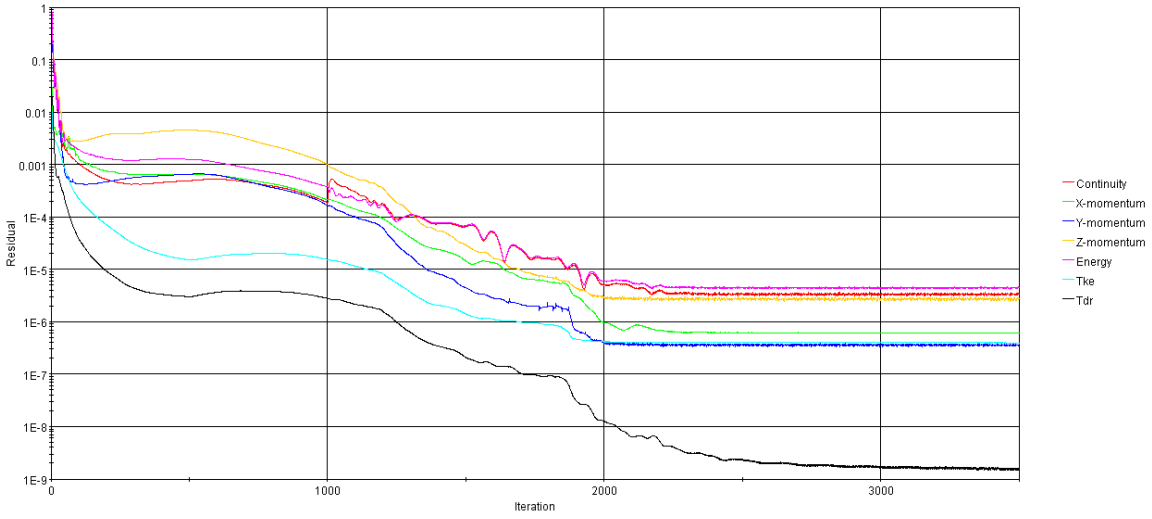

Fig. E.2: Converged residuals of the S2L simulation.

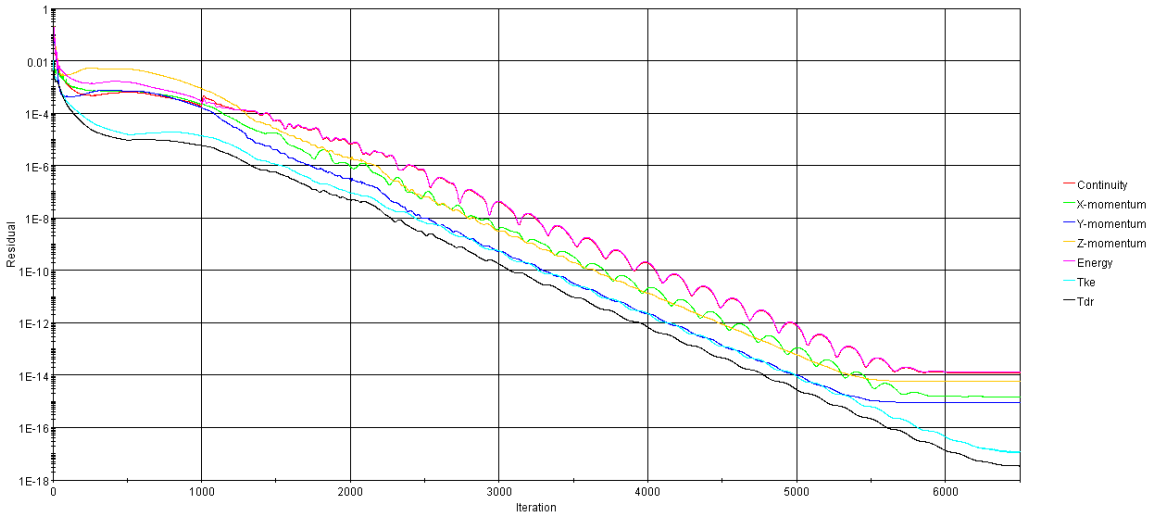

Fig. E.3: Converged residuals of the SLR simulation.

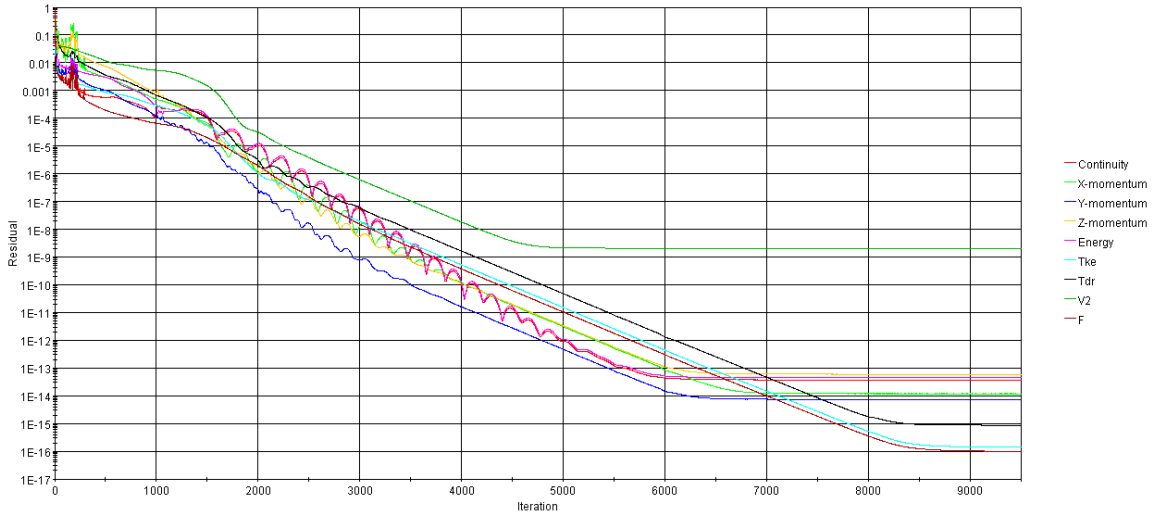

Fig. E.4: Converged residuals of the V2F simulation.

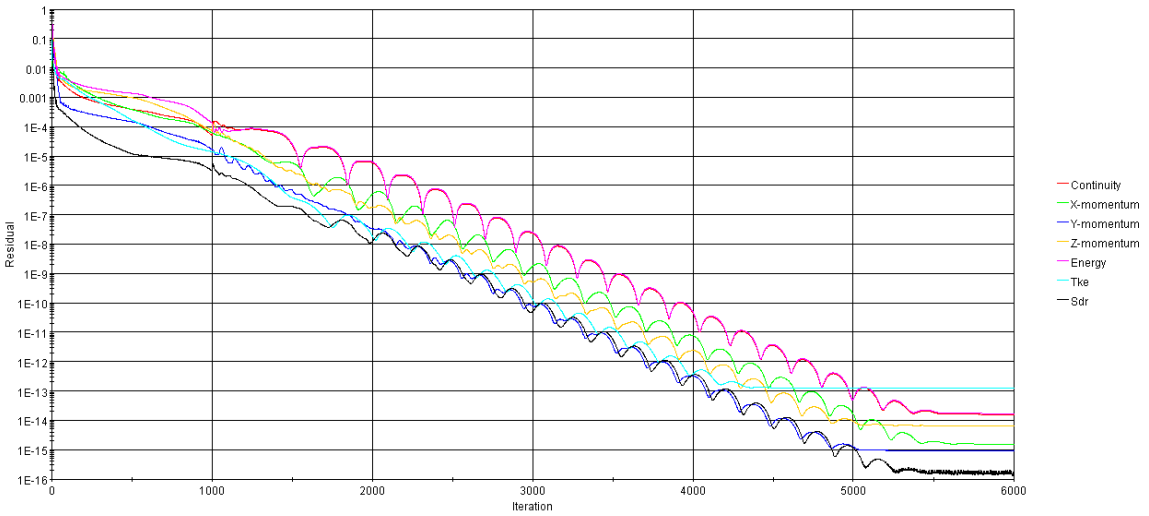

Fig. E.5: Converged residuals of the $k-\omega$ simulation.

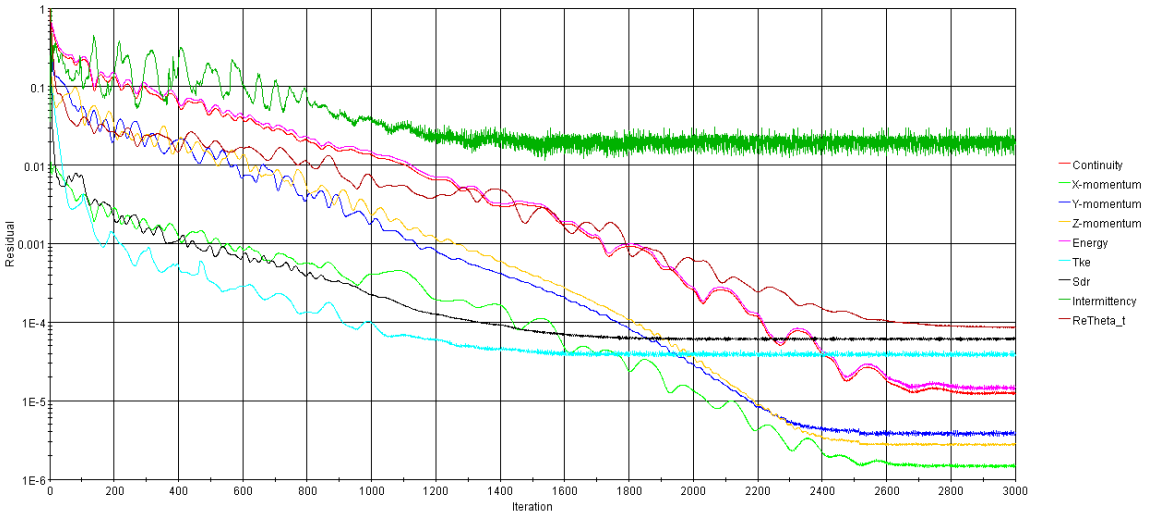

Fig. E.6: Converged residuals of the SST simulation.

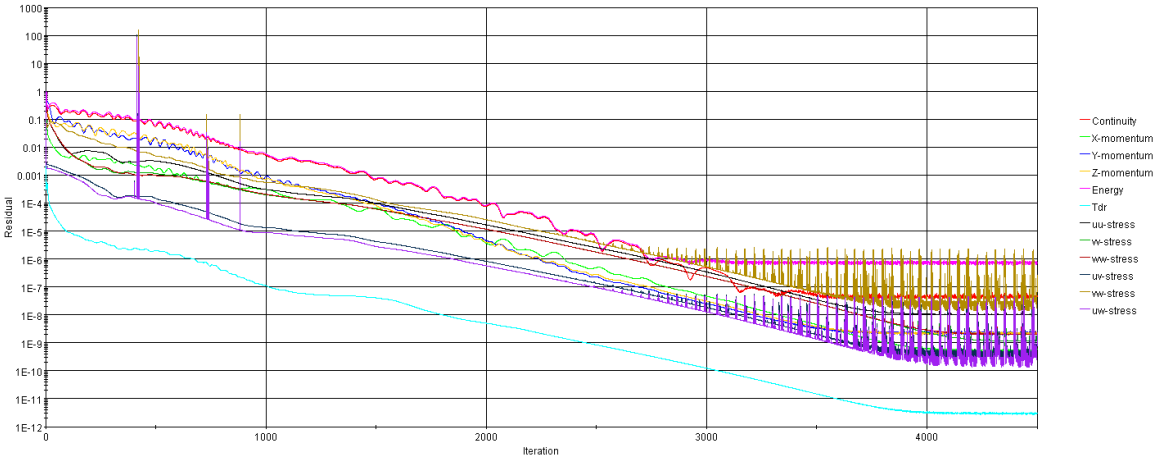

Fig. E.7: Converged residuals of the RST simulation.

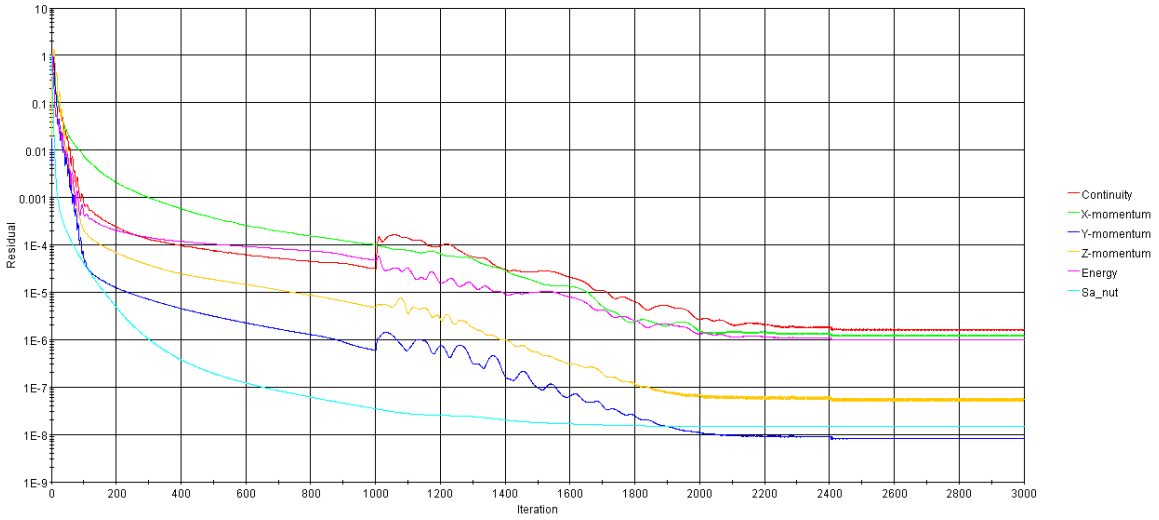

Fig. E.8: Converged residuals of the SA simulation.

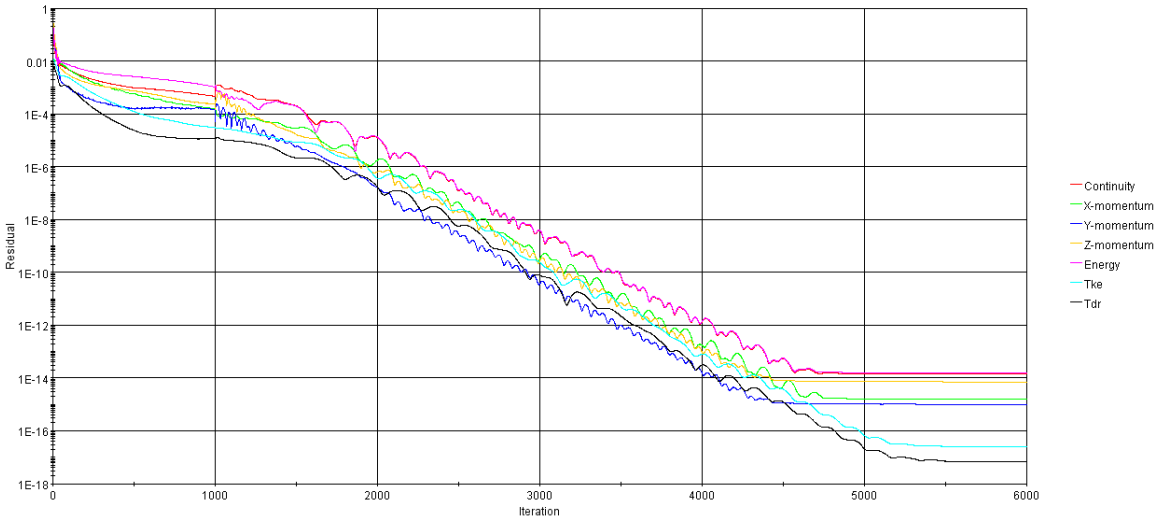

Fig. E.9: Converged residuals of the R2LB simulation.

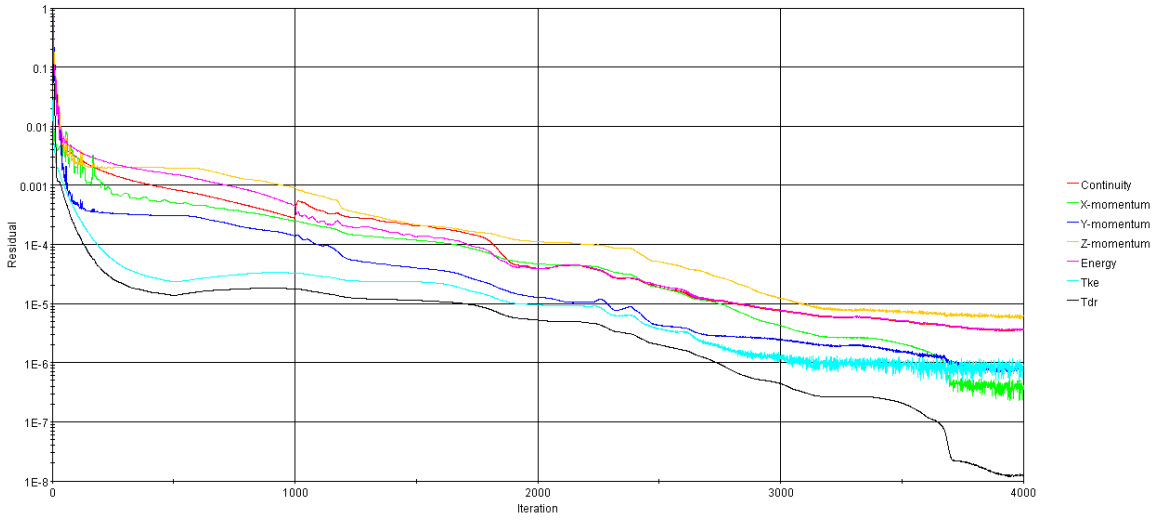

Fig. E.10: Converged residuals of the S2LB simulation.

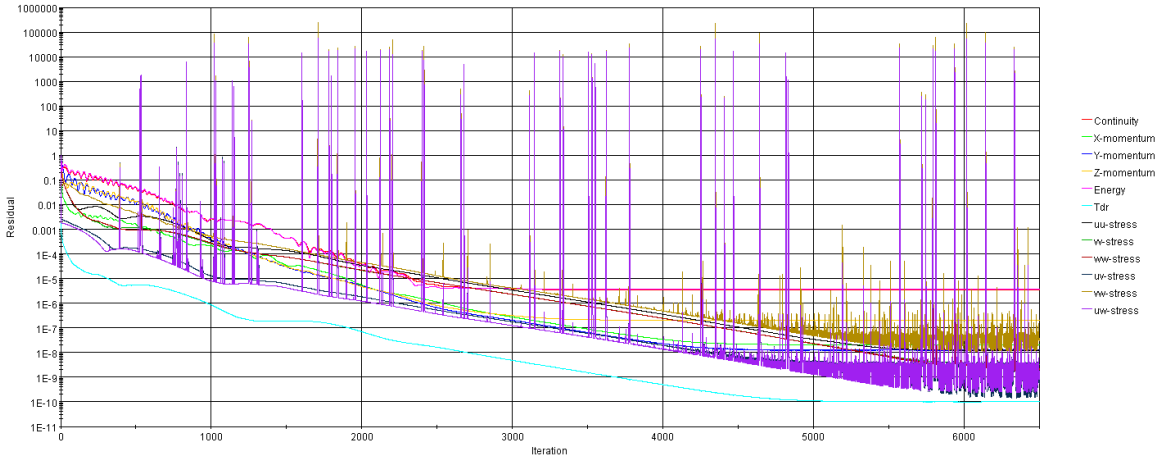

Fig. E.11: Converged residuals of the RSTB simulation.

Appendix F

Experimental Heat Flux Readings & Statistics

The heat flux sensor readings that where taken during the RoBuT experiments for each validation case are presented in the following sections along with the respective uncertainty calculations. Note that multiple readings where only recorded for the M1 and F1 validation cases. For the M2 and F2 cases, only a single reading was taken; thus only the bias uncertainty was used in the modeling error confidence intervals.

F.1 M1

For the M1 case, the heat flux sensor measurements were recorded from each of the nine profile measurements for the inlet velocity as well as the from the three HFS location measurements, for a total of twelve measurements.

For twelve degrees of freedom, $\nu + 1$ and 95% confidence for a two-tailed distribution, $\alpha/2 = 0.25$, the Students t-Distribution gives a probability of $t_{\alpha/2,\,\nu} = 2.201$ [46]. The resulting uncertainties for the M1 case are shown in Table F.1 with the specific readings and statistical values shown in Table F.2.

Table F.1: Uncertainty calculations for M1 validation case.

	HFS 1	HFS 2	HFS 3
Bias (B)	22.262	11.675	13.753
$P = t_{\alpha/2,\,\nu} \cdot \frac{\sigma}{\sqrt{12}}$	4.733	3.442	3.670
$U = \sqrt{B^2 + P^2}$	22.760	12.172	14.234
Relative Error (U/μ)	2.045	2.085	2.070

Table F.2: Heat flux measurements and bias uncertainty for M1 validation case.

	HFS 1		HFS 2		HFS 3	
Reading Location	Measurement	2% Bias	Measurement	2% Bias	Measurement	2% Bias
HFS 1	1118.928	22.379	591.448	11.829	698.982	13.980
HFS 2	1121.246	22.425	574.747	11.495	690.108	13.802
HFS 3	1121.750	22.435	589.888	11.798	692.897	13.858
Inlet 1	1109.725	22.195	586.447	11.729	686.937	13.739
Inlet 2	1101.085	22.022	577.420	11.548	684.838	13.697
Inlet 3	1100.198	22.004	576.917	11.538	676.368	13.527
Inlet 4	1106.499	22.130	279.262	11.585	680.528	13.611
Inlet 5	1119.884	22.398	588.179	11.764	689.655	13.793
Inlet 6	1113.044	22.261	585.645	11.713	690.538	13.811
Inlet 7	1117.920	23.358	585.541	11.711	688.452	13.769
Inlet 8	1113.631	22.273	585.801	11.716	685.331	13.707
Inlet 9	1113.256	22.265	583.772	11.675	687.266	13.745
μ^*	1113.097	22.262	583.756	11.675	687.658	13.753
s	7.450	0.149	5.417	0.108	5.776	0.116

F.2 F1

For the F1 case, the heat flux sensor measurements was recorded once during the inlet velocity measurements as well as at the three HFS location measurements, for a total of four measurements.

For four degrees of freedom, $\nu + 1$ and 95% confidence for a two-tailed distribution, $\alpha/2 = 0.25$, the Students t-Distribution gives a probability of $t_{\alpha/2,\,\nu} = 3.182$ [46]. The resulting uncertainties for the F1 case are shown in Table F.3 with the specific readings and statistical values shown in Table F.4.

Table F.3: Uncertainty calculations for F1 validation case.

	HFS 1	HFS 2	HFS 3
Bias (B)	35.191	24.418	26.859
$P = t_{\alpha/2,\,\nu} \cdot \frac{\sigma}{\sqrt{12}}$	3.096	12.961	6.198
$U = \sqrt{B^2 + P^2}$	35.327	27.644	27.565
Relative Error (U/μ)	2.008	2.264	2.053

Table F.4: Heat flux measurements and bias uncertainty for F1 validation case.

	HFS 1		HFS 2		HFS 3	
Reading Location	Measurement	2% Bias	Measurement	2% Bias	Measurement	2% Bias
HFS 1	1759.223	35.184	1222.187	24.444	1339.146	26.783
HFS 2	1762.222	35.244	1209.993	24.200	1341.975	26.840
HFS 3	1757.568	35.151	1229.728	24.595	1348.396	26.968
Inlet	1759.116	35.182	1221.631	24.433	1342.283	26.846
μ^*	1759.532	35.191	1220.885	24.418	1342.950	26.859
s	1.946	0.039	8.146	0.163	3.896	0.078

F.3 M2

For the M2 case, the heat flux was only measured a single time, thus precision uncertainty is neglected. Table F.5 contains the measured heat flux values and the bias uncertainties. Note that no heat flux measurement was taken at the second HFS due to the failed heater in the plate.

Table F.5: Heat flux measurements and bias uncertainty for M2 validation case.

	HFS 1	HFS 3
Measurement	1149.270	723.934
2% Bias	22.985	14.479

F.4 F2

For the F2 case, the heat flux was only measured a single time, thus precision uncertainty is neglected. Table F.6 contains the measured heat flux values and the bias uncertainties. Note that no heat flux measurement was taken at the second HFS due to the failed heater in the plate.

Table F.6: Heat flux measurements and bias uncertainty for F2 validation case.

	HFS 1	HFS 3
Measurement	2020.670	1389.570
2% Bias	40.413	27.791

Appendix G

Mesh Generation Code

The format required for the as-built dimension file read into the code is presented along with the two files used in this study, after which the full FORTRAN code is shown.

G.1 Input File Format

In the example file format below, N is the number of intervals (number of measurements planes - 1), Plane_k are the coordinates in X of each measurement plane and the remaining values in the table are the corresponding as-built measurements from each plane; from left to right they are: bottom width, middle width, top width, left height, center height and right height. Reference Fig. 2.3.

N					
Plane_1	Plane_2	$\cdots$			Plane_k
B_1	M_1	T_1	L_1	C_1	R_1
B_2	M_2	T_2	L_2	C_2	R_2
	$\cdots$				
$\vdots$					
B_k	M_k	T_k	L_k	C_k	R_k

G.2 Input Files

Table G.1: As-built measurements as of April 5, 2013.

6						
0	13.235	24.585	38.085	48.725	65.475	75.76
11.9413	12.0231	12.0095	12.0141	12.0114	12.0373	
12.0194	12.0522	12.0702	12.042	12.0494	12.043	
12.0524	12.0772	12.074	12.0458	12.0638	12.056	
12.0394	12.1008	12.1044	12.0155	12.0489	12.0334	
12.0698	12.0964	12.0716	12.0678	12.0746	12.0608	
12.073	12.0978	12.0446	12.0604	12.0686	12.055	
12.0804	12.071	12.0365	11.9556	12.0241	12.0154	

Table G.2: As-built measurements as of June 12, 2013.

6						
0	13.285	24.635	38.135	48.775	65.525	75.81
12.005	12.00067	11.996	11.98167	11.99467	11.99067	
12.003	12.00733	12.023	12.02017	12.01917	12.02	
12.01283	12.027	12.01783	12.02883	12.01717	12.02283	
11.996	12.03533	12.03533	12.00317	12.023	12.02767	
12.018	12.042	12.03633	12.04033	12.041	12.03367	
12.001	12.038	12.0135	12.0435	12.046	12.02533	
11.99233	12.0245	12.00467	12.00233	12.01833	12.01917	

Note that all of the measurements are in inches.

G.3 FORTRAN Code

```
Program TMCWT_Mesher

! Description: This program computes the xyz components of the
! grid point node locations throughout a generic rectangular
! domain.  This domain is similar in size to the Rotatable
! Bouyancy Wind Tunnel test section being used for the
! forced and mixed convection validation study.

! The Coordinate System is positioned so that the x axis is
! the axial component that runs down the center of one wall

Implicit None

!Integer, Parameter :: IM = 400
!Integer, Parameter :: JM = 154
!Integer, Parameter :: KM = 154
Integer :: i, j, k
Integer :: IM, JM, KM, CCount, AC, MGM, n
Integer :: Quit
Real :: LConv, Tol
Real :: Lx, Ly, Lz
Real :: dxi, deta, dzeta
Real :: xi, eta, zeta
Real :: a, Bx, ByB, ByT, Bz
Real :: xT, yT, zT
Real :: MCS, SGR, HPT, SWT, TWT, IPT
Real, Dimension(:,:,:), Allocatable :: X, Y, Z
Real, Dimension(:), Allocatable :: xPlane
Real, Dimension(:,:), Allocatable :: fPlane
Real, Dimension(:,:,:), Allocatable :: ACoeff
Real, Dimension(3,2,3) :: PCoeff
Real, Dimension(2,7) :: PCoord
Character (30) :: TSFilename

Tol = 1.0E-15
LConv = 12./0.3048     ! Length conversion in/m

!! Set default values
TSFilename = 'TestSection_6.12.2013.csv'
Quit = 0
IM = 150
JM = 60
KM = 60
CCount = 0
AC = 1
MGM = 1
MCS = 0.01*LConv
SGR = 1.05
HPT = (2.0E-4)*LConv
SWT = (1.25E-4)*LConv
TWT = (1.25E-4)*LConv
IPT = (2.5E-3)*LConv
a = 0.5          ! The planes will always have two sided clustering
Bx = 1.1
ByB = 1.1; ByT = 1.1;
Bz = 1.1

Call TestSection_UserInput()
Call TestSection_FileInput()
Call AxialSpline(n,xPlane,fPlane)

Write(*,'(/,A)')       '  Computing the mesh parameters ...'
Call MeshParam()

Allocate ( X(IM,JM,KM) )
Allocate ( Y(IM,JM,KM) )
Allocate ( Z(IM,JM,KM) )

If (AC == 1) Then
  Lx = xPlane(n+1)-IPT  ! Inches
Else
  Lx = xPlane(n+1)     ! Inches
End If
dxi = 1./Real(IM-1)      ! i delta
deta = 1./Real(JM-1)     ! j delta
dzeta = 1./Real(KM-1)    ! k delta

! Notice to user
Write(*,'(/,A)')       '  The delta values are:'
Write(*,'(A,F12.8)') '    dxi   = ',dxi
Write(*,'(A,F12.8)') '    deta  = ',deta
Write(*,'(A,F12.8)') '    dzeta = ',dzeta
Write(*,'(/,A,/)')     '  Meshing ...'

! Generate the Mesh
Do i = 1,IM
```

```
  Write(*,'(A,I3)') '  Meshing Plane: ', i
  If (i == 1) Then
    xi = 0.
    xT = 0.
  ElseIf (i == IM) Then
    xi = 1.
    xT = xPlane(n+1)
  Else
    If (AC == 1) Then
      xi = Real(i-2)/Real(IM-2)
      xT = Lx*(((Bx+1.)-(Bx-1.)*(((Bx+1.)/(Bx-1.))**(1.-xi)))/ &
        & (1.+((Bx+1.)/(Bx-1.))**(1-xi)))+IPT
      xi = xT/xPlane(n+1)
    Else
      xi = Real(i-1)*dxi
      xT = Lx*xi
    End If
  End If

  Call PlaneSpline(xi,xPlane,ACoeff,PCoeff,PCoord)
  Do k = 1, KM
    zeta = dzeta*Real(k-1)
    If (k == KM) zeta = 1.
    Ly = LengthY(zeta,PCoeff,PCoord)-HPT-TWT
    Do j = 1, JM
      eta = deta*Real(j-1)
      If (j == JM) eta = 1.
      Lz = LengthZ(eta,PCoeff,PCoord)-2.0*SWT

      If (j == 1) Then
        yT = 0.
      ElseIf (j == JM) Then
        yT = Ly+HPT+TWT
      Else
        eta = Real(j-2)/Real(JM-3)
        If (eta .le. 0.5) Then
          yT = Ly*(((2.*a+ByB)*((ByB+1.)/(ByB-1.))**((eta-a)/(1.-a))+2.*a-ByB)/ &
            & ((2.*a+1.)*(1.+((ByB+1.)/(ByB-1.))**((eta-a)/(1.-a))))) + HPT
        Else
          yT = Ly*(((2.*a+ByT)*((ByT+1.)/(ByT-1.))**((eta-a)/(1.-a))+2.*a-ByT)/ &
            & ((2.*a+1.)*(1.+((ByT+1.)/(ByT-1.))**((eta-a)/(1.-a))))) + HPT
        End If
      End If

      If (k == 1) Then
        zT = -0.5*(Lz+2.0*SWT)
      ElseIf (k == KM) Then
        zT = 0.5*(Lz+2.0*SWT)
      Else
        zeta = Real(k-2)/Real(KM-3)
        zT = Lz*(((2.*a+Bz)*((Bz+1.)/(Bz-1.))**((zeta-a)/(1.-a))+2.*a-Bz)/ &
          & ((2.*a+1.)*(1.+((Bz+1.)/(Bz-1.))**((zeta-a)/(1.-a))))) - 0.5*Lz
      End If

      ! Store the (x,y,z) components
      X(i,j,k) = xT/LConv
      Y(i,j,k) = yT/LConv
      Z(i,j,k) = zT/LConv
    End Do
  End Do
End Do

CCount = IM*JM*KM
Write(*,'(/,A)')      '  Mesh Parameters:'
Write(*,'(A)')        '  -----------------'
Write(*,'(A,I10)')    '      Cells in X:',IM
Write(*,'(A,I10)')    '      Cells in Y:',JM
Write(*,'(A,I10)')    '      Cells in Z:',KM
Write(*,'(/,A,I10)') '      Total Cell Count:',CCount

!! Output the mesh to file
Write(*,'(/,A)') '  Outputing the mesh file ...'
!Open(100, File = "Mesh.p3d", Action = 'Write',Form = 'Unformated')
Write(100) IM, JM, KM
!Do i = 1, IM
  Write(100) (((X(i,j,k), i = 1,IM), j = 1,JM), k = 1,KM), &
        & (((Y(i,j,k), i= 1,IM), j = 1,JM), k = 1,KM), &
        & (((Z(i,j,k), i = 1,IM), j = 1,JM), k = 1,KM)
!End Do
Close(100)

!! Finished
Write(*,'(/,A)') '  Mesh Complete'

Contains

Subroutine MeshParam()
  !! This subroutine uses the modified secant method to solve for the beta meshing
```

```
!! parameters required in the mesh.
Integer :: c, j, k, jDim, kDim
Integer :: yFlag, zFlag
Real :: Perc
Real :: x, yO, yN, zO, zN, dy, dz
  Real :: xD, Del, BxD
Real :: xi, eta, zeta
Real :: Lx, Ly, Lz
Real :: BLMT, TLMT, SLMT
Real :: BLMTD, TLMTD, SLMTD
Real :: yCM, zCM

Del = 0.00001

!! Axial Mesh Parameter Calculations
Write(*,'(/,A)') '      Axial Parameters'
Write(*,'(A)')   '      ---------------'
Do
  If (AC == 1) Then
    Lx = xPlane(n+1)-IPT
    Do
              xi = 1./Real(IM-2)
              Bx = 1.000001
              Do c = 1,1000
                   x = Lx*(((Bx+1.)-(Bx-1.)*(((Bx+1.)/(Bx-1.))**(1.-xi)))/ &
                      & (1.+((Bx+1.)/(Bx-1.))**(1.-xi)))-SGR*IPT
                   BxD = Bx*(1.0+Del)
       xD = Lx*(((BxD+1.)-(BxD-1.)*(((BxD+1.)/(BxD-1.))**(1.-xi)))/ &
                      & (1.+((BxD+1.)/(BxD-1.))**(1.-xi)))-SGR*IPT

                   ! Write(*,*) Bx, xN/LConv, (xN-SGR*IPT)/LConv
                   If (Abs(x/LConv) .le. Tol) Exit

                   Bx = Bx-Del*Bx*x/(xD-x)
      End Do

      If (MGM == 1) Then
        xi = Real(IM-3)/Real(IM-2)
        x = Lx*(((Bx+1.)-(Bx-1.)*(((Bx+1.)/(Bx-1.))**(1.-xi)))/ &
          & (1.+((Bx+1.)/(Bx-1.))**(1.-xi)))+IPT
        If (xPlane(n+1)-x .gt. MCS) Then
          IM = IM + 1
        Else If (xPlane(n+1)-x .lt. 0.9*MCS) Then
          Perc = -0.01+(xPlane(n+1)-x)/MCS
          IM = Floor(Real(IM)*Perc)
        Else
          Exit
        End If
      Else
        Exit
      End If
    End Do
  End If

  If ((AC == 2) .And. (MGM == 1)) Then
    If(xPlane(n+1)/Real(IM) .gt. MCS) Then
      IM = IM + 1
    Else If (xPlane(n+1)/Real(IM) .lt. 0.9*MCS) Then
      Perc = -0.01+xPlane(n+1)/Real(IM)/MCS
      IM = Floor(Real(IM)*Perc)
    Else
      Exit
    End If
  Else
    Exit
  End If
End Do

Write(*,'(A,I10)')   '      IM =', IM
Write(*,'(A,F8.5)')  '      Bx = ', Bx

!! Plane Mesh Parameter Calculations
Write(*,'(/,A)') '      Plane Parameters'
Write(*,'(A)')   '      ----------------'
Do
  ByB = 1.000001
  ByT = 1.000001
  Bz = 1.000001
  Do
    Call Plane_MeshParam(ByB*(1.+DEL),ByT*(1.0+Del),Bz*(1.0+Del),BLMTD,TLMTD,SLMTD,yCM,zCM)
    BLMTD = BLMTD-SGR*HPT
    TLMTD = TLMTD-SGR*TWT
    SLMTD = SLMTD-SGR*SWT
    Call Plane_MeshParam(ByB,ByT,Bz,BLMT,TLMT,SLMT,yCM,zCM)
    BLMT = BLMT-SGR*HPT
    TLMT = TLMT-SGR*TWT
    SLMT = SLMT-SGR*SWT
```

```
      !! Beta Calculation
      If ((Abs(BLMT/LConv) .le. Tol) &
        & .And. (Abs(TLMT/LConv) .le. Tol) &
        & .And. (Abs(SLMT/LConv) .le. Tol)) Exit

      ByB = ByB - Del*ByB*BLMT/(BLMTD-BLMT)
      ByT = ByT - Del*ByT*TLMT/(TLMTD-TLMT)
      Bz = Bz - Del*Bz*SLMT/(SLMTD-SLMT)
    End Do

    !! Number of cells (Y,Z) dependent on max cell size
    If (MGM == 1) Then
      ! Y Direction
      If (yCM .gt. MCS) Then
        JM = JM + 1
        yFlag = 0
      Else If (zCM .lt. 0.9*MCS) Then
        JM = JM - 1
        yFlag = 0
      Else
        yFlag = 1
      End If

      ! Z Direction
      If (zCM .gt. MCS) Then
        KM = KM + 1
        zFlag = 0
      Else If (zCM .lt. 0.9*MCS) Then
        KM = KM - 1
        zFlag = 0
      Else
        zFlag = 1
      End If

      ! Exit Clause
      If (yFlag + zFlag == 2) Exit
    Else
      Exit
    End If
  End Do

  Write(*,'(A,I10)')   '      JM =', JM
  Write(*,'(A,I10)')   '      KM =', KM
  Write(*,'(A,F8.5,A,F8.5)')   '      ByB =', ByB, '   ByT =', ByT
  Write(*,'(A,F8.5)')      '      Bz  =', Bz
End Subroutine MeshParam

Subroutine Plane_MeshParam(ByB,ByT,Bz,BLMT,TLMT,SLMT,yCM,zCM)
  Real, Intent(In    ) :: ByB, ByT, Bz
  Real, Intent(  Out) :: BLMT, TLMT, SLMT, yCM, zCM

  Integer :: j, k
  Real :: eta, zeta
  Real :: Ly, Lz
  Real :: dy, dz
  Real, Dimension(JM) :: y
  Real, Dimension(2,JM) :: z

  y = 0.0; z = 0.0;
  yCM = 0.0; zCM = 0.0;

  Call PlaneSpline(0.0,xPlane,ACoeff,PCoeff,PCoord)

  BLMT = 0.0; TLMT = 0.0; SLMT = 0.0;
  Do k = 1,KM
    z(1,:) = z(2,:)
    zeta = Real(k-1)/Real(KM-1)
    If (k == KM) zeta = 1.0
    Ly = Lengthy(zeta,Pcoeff,PCoord)-HPT-TWT
    Do j = 1,JM
      eta = Real(j-1)/Real(JM-1)
      If (j == JM) eta = 1.0
      Lz = LengthZ(eta,PCoeff,PCoord)-2.0*SWT

      If (j == 1) Then
        y(1) = 0.
      ElseIf (j == JM) Then
        y(JM) = Ly+HPT+TWT
      Else
        If (eta .le. 0.5) Then
          eta = Real(j-2)/Real(JM-3)
          y(j) = Ly*(((2.*a+ByB)*((ByB+1.)/(ByB-1.))**((eta-a)/(1.-a))+2.*a-ByB)/ &
            & ((2.*a+1.)*(1.+((ByB+1.)/(ByB-1.))**((eta-a)/(1.-a))))) + HPT
        Else
          eta = Real(j-2)/Real(JM-3)
          y(j) = Ly*(((2.*a+ByT)*((ByT+1.)/(ByT-1.))**((eta-a)/(1.-a))+2.*a-ByT)/ &
            & ((2.*a+1.)*(1.+((ByT+1.)/(ByT-1.))**((eta-a)/(1.-a))))) + HPT
        End If
```

```
      End If

      If (k == 1) Then
        z(2,1) = -0.5*(Lz+2.0*SWT)
      ElseIf (k == KM) Then
        z(2,JM) = 0.5*(Lz+2.0*SWT)
      Else
        zeta = Real(k-2)/Real(KM-3)
        z(2,j) = Lz*(((2.*a+Bz)*((Bz+1.)/(Bz-1.))**((zeta-a)/(1.-a))+2.*a-Bz)/ &
          & ((2.*a+1.)*(1.+((Bz+1.)/(Bz-1.))**((zeta-a)/(1.-a))))) - 0.5*Lz
      End If

      !! Calculate the change in Y and Z
      If (k == 1) z(1,j) = z(2,j)

      If (j == 1) Then
        dy = 0.0
      Else
        dy = y(j) - y(j-1)
      End If
      If (k == 1) Then
        dz = 0.0
      Else
        dz = z(2,j) - z(1,j)
      End If

      !! Find max thickness of second layer off the wall
      ! Y Direction
      If (j == 3) Then
        If (dy .gt. BLMT) BLMT = dy
      End If
      If (j == JM-1) Then
        If (dy .gt. TLMT) TLMT = dy
      End If

      ! Z Direction
      If (k == 3) Then
        If (dz .gt. SLMT) SLMT = dz
      End If
      If (k == KM-1) Then
        If (dz .gt. SLMT) SLMT = dz
      End If

      !! Keep track of the max cell size
      If (j .ge. 2) Then
        If (dy .gt. yCM) yCM = dy
      End If
      If (k .ge. 2) Then
        If (dz .gt. zCM) zCM = dz
      End If
    End Do
  End Do
End Subroutine Plane_MeshParam

Subroutine TestSection_UserInput()
    Character (30) :: Rec
  Real :: Temp

  Write(*,'(/,A)') 'Welcome to the TMCWT Test Section Mesher'
  Write(*,'(A)')   '***************************************'

  Write(*,'(/,A,A,A)') 'Specify the test section As-Built dimension filename:  (Default: ',Trim(
     TSFilename),')'
    Write(*,'(A)')   '-------------------------------------------------------'
  Read(*,'(A30)') Rec
    If (Rec .ne. ' ') Then
        TSFilename = Rec
    EndIf

  !! Create mesh based on # of cells or max cell size
  Write(*,'(/,A,I2,A)') 'Specify the mesh generation method:  (Default: ',MGM,')'
  Write(*,'(A)')   '-----------------------------------'
  Write(*,'(A)')   '  1) Specify the maximum cell size'
  Write(*,'(A)')   '  2) Specify the number of cells in each direction (x,y,z)'
  Read(*,'(A30)') Rec
  If (Rec .ne. ' ') Then
    Read(Rec,*) MGM
  End If
  If (MGM .ne. 1) Then
    Read(Rec,*) MGM
    !! Number of cells in each coordinate direction of the mesh
    Write(*,'(/,A,I4,A)') '  Input the # of cells desired in the x direction:  (',IM,')'
    Read(*,'(A30)') Rec
    If (Rec .ne. ' ') Then
      Read(Rec,*) IM
    End If
    Write(*,'(/,A,I4,A)') '  Input the # of cells desired in the y direction:  (',JM,')'
    Read(*,'(A30)') Rec
```

```
    If (Rec .ne. ' ') Then
      Read(Rec,*) JM
    End If
    Write(*,'(/,A,I4,A)') '  Input the # of cells desired in the z direction:  (',KM,')'
    Read(*,'(A30)') Rec
    If (Rec .ne. ' ') Then
      Read(Rec,*) KM
    End If
  Else
    !! Max cell size
    Write(*,'(/,A,F5.3,A)') 'Input the max cell size:  (',MCS/LConv,' m)'
    Read(*,'(A30)') Rec
    If (Rec .ne. ' ') Then
      Read(Rec,*) Temp
      MCS = Temp*LConv
    End If
  End If

  !! Cluster in the Axial Direction
  Write(*,'(/,A,I2,A)') 'Specify axial mesh clustering method:  (Default: ',AC,')'
  Write(*,'(A)')    '-------------------------------------'
  Write(*,'(A)')    '  1) One-sided clustering at inlet'
  Write(*,'(A)')    '  2) No clustering'
  Read(*,'(A30)') Rec
  If (Rec .ne. ' ') Then
    Read(Rec,*) AC
  End If

  !! Mesh Parameters
  Write(*,'(/,A)') 'Specify Mesh Parameters'
  Write(*,'(A)')    '----------------------'
  !! Surface mesh growth rate
  Write(*,'(/,A,F5.3,A)') 'Input the surface growth rate:  (',SGR,')'
  Read(*,'(A30)') Rec
  If (Rec .ne. ' ') Then
    Read(Rec,*) SGR
  End If

  !! Thickness of near wall cell layer
  Write(*,'(/,A)') 'Thicknesses of the near wall cell layers:'
  Write(*,'(A)')    '---------------------------------------'
  Write(*,'(/,A,ES9.2,A)') '  Heated plate wall:  (',HPT/LConv,' m)'
  Read(*,'(A30)') Rec
  If (Rec .ne. ' ') Then
    Read(Rec,*) Temp
    HPT = Temp*LConv
  End If
  Write(*,'(/,A,ES9.2,A)') '  Side walls:  (',SWT/LConv,' m)'
  Read(*,'(A30)') Rec
  If (Rec .ne. ' ') Then
    Read(Rec,*) Temp
    SWT = Temp*LConv
  End If
  Write(*,'(/,A,ES9.2,A)') '  Top wall:  (',TWT/LConv,' m)'
  Read(*,'(A30)') Rec
  If (Rec .ne. ' ') Then
    Read(Rec,*) Temp
    TWT = Temp*LConv
  End If
  If (AC == 1) Then
    Write(*,'(/,A,ES9.2,A)') '  Inlet plane:  (',IPT/LConv,' m)'
    Read(*,'(A30)') Rec
    If (Rec .ne. ' ') Then
      Read(Rec,*) Temp
      IPT = Temp*LConv
    End If
  End If
End Subroutine TestSection_UserInput

Subroutine TestSection_FileInput()
  Integer :: i
    Real :: A90
    Real, Dimension(:), Allocatable :: dTest
  Real, Dimension(:,:), Allocatable :: SDim

  Open(100,File = TSFileName,Action = 'Read')
  Read(100,'(I3)') n

  Allocate ( SDim(6,n+1) )
  Allocate ( xPlane(n+1) )
  Allocate ( fPlane(n+1,9) )
    Allocate ( dTest(n+1) )

  ! Notice to user
  Write(*,'(/,A)') '  Setting up the plane data ...'

  ! Read in the axial location of the planes where the dimensions are known
    Read(100,*) xPlane(:)
```

```
  ! Read in the known dimensions on each plane
  ! Assumes that 6 dimensions are known on the plane
  ! Width  - Bottom
  !       - Middle
  !       - Top
  ! Height - Left
  !       - Center
  !       - Right
  Do i = 1,n+1
    Read(100,*) SDim(:,i)
  End Do
  Close(100)

  !~    Write(*,*) '----------------------'
  !~    Do i = 1,n+1
  !~    Write(*,'(7F8.4)') xPlane(i), SDim(1:6,i)
  !~    End Do
  !~    Write(*,*) '----------------------'

  Do i = 1,n+1
    Write(*,'(A)') ' -------------------------'
    Write(*,'(A,I4)') '  Plane: ', i

        Call Secant(A90,SDim(:,i))
    fPlane(i,1) = -0.5*SDim(1,i)
    fPlane(i,2) = -0.5*SDim(2,i)
    fPlane(i,3) = fPlane(i,1) - SDim(4,i)*sin(A90)
        fPlane(i,4) = SDim(4,i)*cos(A90)
        fPlane(i,5) = SDim(5,i)
        fPlane(i,6) = SDim(6,i)*cos(A90)
        fPlane(i,8) = 0.5*SDim(2,i)
        fPlane(i,9) = 0.5*SDim(1,i)
        fPlane(i,7) = fPlane(i,9) + SDim(6,i)*sin(A90)
        dTest(i) = sqrt((fPlane(i,7)-fPlane(i,3))**2 &
                        & + (fPlane(i,6)-fPlane(i,4))**2)
    End Do

  ! Notice to the user
  Write(*,'(/,A)') '  Descrepancy in top width measurement:'
    Do i = 1,n+1
        Write(*,'(A,I3,3X,F12.8,3X,ES16.8)') '       Plane:',i, dTest(i), dTest(i)-SDim(3,i)
    End Do

  Deallocate(SDim)
  Deallocate(dTest)

End Subroutine TestSection_FileInput

Subroutine PlaneSpline(xi,xDim,ACoeff,PCoeff,PC)
  Real, Intent(In    ) :: xi
  Real, Intent(In    ), Dimension(n+1) :: xDim
  Real, Intent(In    ), Dimension(4,n,9) :: ACoeff
    Real, Intent(  Out), Dimension(3,2,3) :: PCoeff
  Real, Intent(  Out), Dimension(2,7) :: PC

    Real :: f2, dx, xP
    Integer :: a, b, c, x, y
    Integer :: i

  xP = xi*xDim(n+1)

  Call PlaneCoordinates(PC,xP,xDim,ACoeff)

    !! Calculate Spline Coefficent for the plane curves
    Do i = 1,3
        Select Case (i)
            Case (1)
                a = 1; b = 2; c = 3; x = 1; y = 2;
            Case (2)
                a = 3; b = 4; c = 5; x = 2; y = 1;
            Case (3)
                a = 7; b = 6; c = 5; x = 1; y = 2;
        End Select

        f2 = (3./PC(x,c)-PC(x,a)) &
                & *((PC(y,c)-PC(y,b))/(PC(x,c)-PC(x,b)) &
                & +(PC(y,a)-PC(y,b))/(PC(x,b)-PC(x,a)))
        dx = PC(x,b)-PC(x,a)
        PCoeff(1,1,i) = f2/(6.*dx)
        PCoeff(2,1,i) = PC(y,a)/dx
        PCoeff(3,1,i) = PC(y,b)/dx-f2*dx/6.
        dx = PC(x,c)-PC(x,b)
        PCoeff(1,2,i) = f2/(6.*dx)
        PCoeff(2,2,i) = PC(y,b)/dx-f2*dx/6.
        PCoeff(3,2,i) = PC(y,c)/dx
    End Do
End Subroutine PlaneSpline
```

```
Function LengthZ(eta,PCoeff,PC)
  Real, Intent(In    ) :: eta
  Real, Intent(In    ), Dimension(3,2,3) :: PCoeff
  Real, Intent(In    ), Dimension(2,7) :: PC

  Real :: LengthZ
  Real :: zL, zR, yL, yR

  !! Cubic Spline Calculation
! If (eta .le. 0.5) Then
!   y = eta*PC(1,4)
!   zL = PCoeff(1,1,1)*(y-PC(1,1))**3 &
!     & + PCoeff(2,1,1)*(PC(1,2)-y) &
!     & + PCoeff(3,1,1)*(y-PC(1,1))
!   zR = PCoeff(1,1,3)*(y-PC(1,7))**3 &
!     & + PCoeff(2,1,3)*(PC(1,6)-y) &
!     & + PCoeff(3,1,3)*(y-PC(1,7))
!   LengthZ = zR-zL
! Else
!   yL = eta*PC(1,3)
!   zL = PCoeff(1,2,1)*(PC(1,3)-yL)**3 &
!     & + PCoeff(2,2,1)*(PC(1,3)-yL) &
!     & + PCoeff(3,2,1)*(yL-PC(1,2))
!
!   yR = eta*PC(1,5)
!   zR = PCoeff(1,2,3)*(PC(1,5)-yR)**3 &
!     & + PCoeff(2,2,3)*(PC(1,5)-yR) &
!     & + PCoeff(3,2,3)*(yR-PC(1,6))
!   LengthZ = sqrt((zR-zL)**2+(yR-yL)**2)
! End If

  !! Lagrange Interpolating Poly Calculation
  If (eta .le. 0.5) Then
    yL = eta*PC(1,4)
    yR = yL
  Else
    yL = eta*PC(1,3)
    yR = eta*PC(1,5)
  End If

  zL = PC(2,1)*(yL-PC(1,2))*(yL-PC(1,3)) &
      & /((PC(1,1)-PC(1,2))*(PC(1,1)-PC(1,3))) &
    & + PC(2,2)*(yL-PC(1,1))*(yL-PC(1,3)) &
      & /((PC(1,2)-PC(1,1))*(PC(1,2)-PC(1,3))) &
    & + PC(2,3)*(yL-PC(1,1))*(yL-PC(1,2)) &
      & /((PC(1,3)-PC(1,1))*(PC(1,3)-PC(1,2)))

  zR = PC(2,7)*(yR-PC(1,6))*(yR-PC(1,5)) &
      & /((PC(1,7)-PC(1,6))*(PC(1,7)-PC(1,5))) &
    & + PC(2,6)*(yR-PC(1,7))*(yR-PC(1,5)) &
      & /((PC(1,6)-PC(1,7))*(PC(1,6)-PC(1,5))) &
    & + PC(2,5)*(yR-PC(1,7))*(yR-PC(1,6)) &
      & /((PC(1,5)-PC(1,7))*(PC(1,5)-PC(1,6)))

  LengthZ = sqrt((zR-zL)**2+(yR-yL)**2)
End Function LengthZ

Function LengthY(zeta,PCoeff,PC)
  Real, Intent(In    ) :: zeta
  Real, Intent(In    ), Dimension(3,2,3) :: PCoeff
  Real, Intent(In    ), Dimension(2,7) :: PC

  Real :: LengthY
  Real :: zB, zT, yT

  !! Cubic Spline Calculation
! If (zeta .le. 0.5) Then
!   zB = PC(2,1)*abs((zeta-0.5)/0.5)
!   zT = PC(2,3)*abs((zeta-0.5)/0.5)
!   yT = PCoeff(1,1,2)*(zT-PC(2,3))**3 &
!     & + PCoeff(2,1,2)*(PC(2,4)-zT) &
!     & + PCoeff(3,1,2)*(zT-PC(2,3))
!   LengthY = sqrt((zT-zB)**2+yT**2)
! Else
!   zB = PC(2,7)*(zeta-0.5)/0.5
!   zT = PC(2,5)*(zeta-0.5)/0.5
!   yT = PCoeff(1,2,2)*(PC(2,5)-zT)**3 &
!     & + PCoeff(2,2,2)*(PC(2,5)-zT) &
!     & + PCoeff(3,2,2)*(zT-PC(2,4))
!   LengthY = sqrt((zT-zB)**2+yT**2)
! End If

  !! Lagrange Interpolating Poly Calculation
  If (zeta .le. 0.5) Then
    zB = PC(2,1)*abs((zeta-0.5)/0.5)
    zT = PC(2,3)*abs((zeta-0.5)/0.5)
  Else
```

```
    zB = PC(2,7)*(zeta-0.5)/0.5
    zT = PC(2,5)*(zeta-0.5)/0.5
  End If

  yT = PC(1,3)*(zT-PC(2,4))*(zT-PC(2,5)) &
     & /((PC(2,3)-PC(2,4))*(PC(2,3)-PC(2,5))) &
    & + PC(1,4)*(zT-PC(2,3))*(zT-PC(2,5)) &
     & /((PC(2,4)-PC(2,3))*(PC(2,4)-PC(2,5))) &
    & + PC(1,5)*(zT-PC(2,3))*(zT-PC(2,4)) &
     & /((PC(2,5)-PC(2,3))*(PC(2,5)-PC(2,4)))

  LengthY = sqrt((zT-zB)**2+yT**2)
End Function LengthY

Subroutine PlaneCoordinates(Coord,xP,x,ACoeff)
  Real, Intent(In    ) :: xP
  Real, Intent(In    ), Dimension(n+1) :: x
  Real, Intent(In    ), Dimension(4,n,9) :: ACoeff
  Real, Intent(  Out), Dimension(2,7) :: Coord  ! Coord = (Y,Z) of 7 points on L, T, and R sides
    of plane

  Integer :: i, s, k, flag
  Real, Dimension(9) :: f

  Do i = 1,9
    s = 1
    flag = 0
    Do
      k = s+1
      If( (xP .ge. x(s)) .AND. (xP .le. x(s+1)) ) Then
        f(i) = ACoeff(1,s,i)*(x(k)-xP)**3 &
           & + ACoeff(2,s,i)*(xP-x(k-1))**3 &
             & + ACoeff(3,s,i)*(x(k)-xP) &
             & + ACoeff(4,s,i)*(xP-x(k-1))
        flag = 1
      Else
        s = s+1
      EndIf
      If ((s == n+1) .or. (flag == 1)) Exit
    End Do
  End Do

  ! Calculate the (Y,Z) Coordinates of the 7 points - Coord(2,7) = (y:z,Point)
  Coord(1,1) = 0.
  Coord(2,1) = f(1)
  Coord(1,2) = 0.5*f(5)
  Coord(2,2) = f(2)
  Coord(1,3) = f(4)
  Coord(2,3) = f(3)
  Coord(1,4) = f(5)
  Coord(2,4) = 0.
  Coord(1,5) = f(6)
  Coord(2,5) = f(7)
  Coord(1,6) = 0.5*f(5)
  Coord(2,6) = f(8)
  Coord(1,7) = 0.
  Coord(2,7) = f(9)
End Subroutine PlaneCoordinates

Subroutine AxialSpline(n,x,fx)
  Integer, Intent(In    ) :: n           ! n (number of sections) must be >= 2
  Real, Intent(In    ), Dimension(n+1) :: x    ! Axial position of the planes
  Real, Intent(In    ), Dimension(n+1,9) :: fx   ! 9 - assumes 9 curves around left, top,
                                                 !       and right sides for the geometry
  Integer :: i, k, s
  Real, Dimension(n-1) :: e, f, g, r
  Real, Dimension(n+1) :: f2

    Allocate(ACoeff(4,n,9))

  Write(*,'(/,A)') '  Computing axial spline coefficients ...'
  ! Solve for coefficients of cubic splines along the axial direction
  ! Implimenting the Thomas Algorithm as defined by Chapra and Canale
  Do i = 1,9
    Write(*,'(A,I4)') '       Spline: ',i
    f2 = 0.0
    Call TriDiag(x(:),fx(:,i),n,e,f,g,r)
    ! Decomposition: Thomas Algorithm LU
    Do k = 2, n-1
      e(k) = e(k)/f(k-1)
      f(k) = f(k) - e(k)*g(k-1)
    End Do
    ! Forward Substitution
    Do k = 2, n-1
      r(k) = r(k) - e(k)*r(k-1)
    End Do
    ! Back Substitution
    f2(n) = r(n-1)/f(n-1)
```

```
    Do k = n-2,1,-1
      f2(k+1) = (r(k)-g(k)*f2(k+2))/f(k)  ! Note shift in f2 array for switch of bounds
    End Do

    ! Calculate the curve coefficients
    Do s = 1, n
      k = s+1
      ACoeff(1,s,i) = f2(k-1)/(6.0*(x(k)-x(k-1)))
      ACoeff(2,s,i) = f2(k)/(6.0*(x(k)-x(k-1)))
      ACoeff(3,s,i) = fx(k-1,i)/(x(k)-x(k-1)) &
              & -f2(k-1)*(x(k)-x(k-1))/6.0
      ACoeff(4,s,i) = fx(k,i)/(x(k)-x(k-1)) &
              & -f2(k)*(x(k)-x(k-1))/6.0
    End Do
  End Do

End Subroutine AxialSpline

Subroutine TriDiag(x,y,n,e,f,g,r)
  Integer, Intent(In   ) :: n
  Real, Intent(In   ), Dimension(n) :: x, y
  Real, Intent(  Out), Dimension(n-1) :: e, f, g, r
  Integer :: i, j

  e = 0.0; f = 0.0; g = 0.0; r = 0.0;

  f(1) = 2*(x(3)-x(1))
  g(1) = x(3) - x(2)
  r(1) = (6./(x(3)-x(2)))*(y(3)-y(2)) &
     & + (6./(x(2)-x(1)))*(y(1)-y(2))
  Do i = 2,n-2
    j = i+1
    e(i) = x(j)-x(j-1)
    f(i) = 2.0*(x(j+1)-x(j-1))
    g(i) = x(j+1)-x(j)
    r(i) = (6./(x(j+1)-x(j)))*(y(j+1)-y(j)) &
        & + (6./(x(j)-x(j-1)))*(y(j-1)-y(j))
  End Do
  e(n-1) = x(6)-x(5)
  f(n-1) = 2.0*(x(7)-x(5))
  r(n-1) = (6./(x(7)-x(6)))*(y(7)-y(6)) &
       & + (6./(x(6)-x(5)))*(y(5)-y(6))
End Subroutine TriDiag

Subroutine Secant(Alpha, PDim)
  Real, Intent(In   ), Dimension(6) :: PDim
  Real, Intent(  Out) :: Alpha
  Real :: Aconv, Pi, Tol
    Real :: aO, aN, fO, fN
  Integer :: i

  Pi = 4.0*atan(1.0)
  AConv = Pi/180.0
    Tol = 10.**(-14)

    !! Initial Guess
    aO = 92.*AConv
    aN = 91.*AConv

    !! Fist Evaluation
    fO = FEval(aO,PDim)

    Write(*,'(A)') ' ------------------------'
  Do i = 1, 10000000
        fN = FEval(aN,PDim)
        Write(*,'(I6,3X,F12.8,3X,ES16.8)') i, aN/AConv, fN
        If ((abs(fN) .le. Tol) .Or. (abs(aN-aO) .le. Tol)) Exit
        Alpha = aN-((fN*(aO-aN))/(fO-fN))

        fO = fN
        aO = aN
        aN = Alpha
  End Do
    Write(*,'(A)') ' ------------------------'

  Alpha = Alpha - 0.5*Pi  ! Subtract 90 Deg for use in calculating the top corner coord
End Subroutine Secant

Function FEval(Alp,PDim)
  Real, Intent(In   ) :: Alp
    Real, Intent(In   ), Dimension(6) :: PDim
  Real :: FEval
    Real :: B, R, L, T, D, Rho, Tau

    B = PDim(1)
    R = PDim(6)
    L = PDim(4)
    T = PDim(3)
```

```
    D = sqrt(B*B+R*R-2.*B*R*cos(Alp))      ! Calculate length of cross section diagonal
                                           !   based on the corner angle (alpha)
    Rho = asin(sin(Alp)*R/D)               ! Calculate the portion of the bottom left vertex
                                           !   angle that is within the lower right triangle
    Tau = acos((L*L+D*D-T*T)/(2.*L*D))     ! Calculate the portion of the bottom left vertex
                                           !   angle that is within the upper left triangle
    FEval = Alp - Rho - Tau                ! Calculate the difference between the supposed lower
                                           !   left vertex angle and the calculate portions
End Function FEval

End Program TMCWT_Mesher
```

Appendix H

Copyright Permission from ELD for Fig. 2.2

From email correspondence:

Hello Barton and Jared,

You may use the drawings that we furnished with the wind tunnel in your papers.

Indicate that the images are "Used with permission" and credit Engineering Laboratory Design, Inc.

Thanks for requesting permission.

Regards,

Sig Anderson

Sigurd W. Anderson, President Engineering Laboratory Design, Inc. 2021 South Highway 61 PO Box 278 Lake City, MN 55041 USA mariner@eldinc.com 651-345-4515 800-795-8536 FAX 651-345-5095 www.eldinc.com

Appendix I

Copyright Permission from Elsevier for Fig. 5.1

ELSEVIER LICENSE
TERMS AND CONDITIONS

Oct 21, 2013

147

This is a License Agreement between Jared M Iverson ("You") and Elsevier ("Elsevier") provided by Copyright Clearance Center ("CCC"). The license consists of your order details, the terms and conditions provided by Elsevier, and the payment terms and conditions.

All payments must be made in full to CCC. For payment instructions, please see information listed at the bottom of this form.

Supplier	Elsevier Limited The Boulevard,Langford Lane Kidlington,Oxford,OX5 1GB,UK
Registered Company Number	1982084
Customer name	Jared M Iverson
Customer address	184 East 200 North LOGAN, UT 84321
License number	3253660905821
License date	Oct 21, 2013
Licensed content publisher	Elsevier
Licensed content publication	International Journal of Heat and Mass Transfer
Licensed content title	Assessment by comparison with DNS data of turbulence models used in simulations of mixed convection
Licensed content author	W.S. Kim,S. He,J.D. Jackson
Licensed content date	March 2008
Licensed content volume number	51
Licensed content issue number	5–6
Number of pages	20
Start Page	1293
End Page	1312
Type of Use	reuse in a thesis/dissertation
Portion	figures/tables/illustrations
Number of figures/tables/illustrations	1
Format	both print and electronic
Are you the author of this Elsevier article?	No

Will you be translating?	No	
Order reference number		
Title of your thesis/dissertation	Computational Fluid Dynamics Validation of Buoyant Turbulent Flow Heat Transfer	148
Expected completion date	Jan 2014	
Estimated size (number of pages)	165	
Elsevier VAT number	GB 494 6272 12	
Permissions price	0.00 USD	
VAT/Local Sales Tax	0.0 USD / 0.0 GBP	
Total	0.00 USD	
Terms and Conditions		

INTRODUCTION

1. The publisher for this copyrighted material is Elsevier. By clicking "accept" in connection with completing this licensing transaction, you agree that the following terms and conditions apply to this transaction (along with the Billing and Payment terms and conditions established by Copyright Clearance Center, Inc. ("CCC"), at the time that you opened your Rightslink account and that are available at any time at http://myaccount.copyright.com).

GENERAL TERMS

2. Elsevier hereby grants you permission to reproduce the aforementioned material subject to the terms and conditions indicated.

3. Acknowledgement: If any part of the material to be used (for example, figures) has appeared in our publication with credit or acknowledgement to another source, permission must also be sought from that source. If such permission is not obtained then that material may not be included in your publication/copies. Suitable acknowledgement to the source must be made, either as a footnote or in a reference list at the end of your publication, as follows:

"Reprinted from Publication title, Vol /edition number, Author(s), Title of article / title of chapter, Pages No., Copyright (Year), with permission from Elsevier [OR APPLICABLE SOCIETY COPYRIGHT OWNER]." Also Lancet special credit - "Reprinted from The Lancet, Vol. number, Author(s), Title of article, Pages No., Copyright (Year), with permission from Elsevier."

4. Reproduction of this material is confined to the purpose and/or media for which permission is hereby given.

5. Altering/Modifying Material: Not Permitted. However figures and illustrations may be altered/adapted minimally to serve your work. Any other abbreviations, additions, deletions and/or any other alterations shall be made only with prior written authorization of Elsevier Ltd. (Please contact Elsevier at permissions@elsevier.com)

6. If the permission fee for the requested use of our material is waived in this instance, please be advised that your future requests for Elsevier materials may attract a fee.

7. Reservation of Rights: Publisher reserves all rights not specifically granted in the combination of (i) the license details provided by you and accepted in the course of this licensing transaction, (ii) these terms and conditions and (iii) CCC's Billing and Payment terms and conditions.

149

8. License Contingent Upon Payment: While you may exercise the rights licensed immediately upon issuance of the license at the end of the licensing process for the transaction, provided that you have disclosed complete and accurate details of your proposed use, no license is finally effective unless and until full payment is received from you (either by publisher or by CCC) as provided in CCC's Billing and Payment terms and conditions. If full payment is not received on a timely basis, then any license preliminarily granted shall be deemed automatically revoked and shall be void as if never granted. Further, in the event that you breach any of these terms and conditions or any of CCC's Billing and Payment terms and conditions, the license is automatically revoked and shall be void as if never granted. Use of materials as described in a revoked license, as well as any use of the materials beyond the scope of an unrevoked license, may constitute copyright infringement and publisher reserves the right to take any and all action to protect its copyright in the materials.

9. Warranties: Publisher makes no representations or warranties with respect to the licensed material.

10. Indemnity: You hereby indemnify and agree to hold harmless publisher and CCC, and their respective officers, directors, employees and agents, from and against any and all claims arising out of your use of the licensed material other than as specifically authorized pursuant to this license.

11. No Transfer of License: This license is personal to you and may not be sublicensed, assigned, or transferred by you to any other person without publisher's written permission.

12. No Amendment Except in Writing: This license may not be amended except in a writing signed by both parties (or, in the case of publisher, by CCC on publisher's behalf).

13. Objection to Contrary Terms: Publisher hereby objects to any terms contained in any purchase order, acknowledgment, check endorsement or other writing prepared by you, which terms are inconsistent with these terms and conditions or CCC's Billing and Payment terms and conditions. These terms and conditions, together with CCC's Billing and Payment terms and conditions (which are incorporated herein), comprise the entire agreement between you and publisher (and CCC) concerning this licensing transaction. In the event of any conflict between your obligations established by these terms and conditions and those established by CCC's Billing and Payment terms and conditions, these terms and conditions shall control.

14. Revocation: Elsevier or Copyright Clearance Center may deny the permissions described in this License at their sole discretion, for any reason or no reason, with a full refund payable to you. Notice of such denial will be made using the contact information provided by you. Failure to receive such notice will not alter or invalidate the denial. In no event will Elsevier or Copyright Clearance Center be responsible or liable for any costs, expenses or damage incurred by you as a result of a denial of your permission request, other than a refund of the amount(s) paid by you to Elsevier and/or Copyright Clearance Center for denied permissions.

LIMITED LICENSE

The following terms and conditions apply only to specific license types:

15. **Translation**: This permission is granted for non-exclusive world **English** rights only unless your license was granted for translation rights. If you licensed translation rights you may only translate this content into the languages you requested. A professional translator must perform all translations and reproduce the content word for word preserving the integrity of the article. If this license is to re-use 1 or 2 figures then permission is granted for non-exclusive world rights in all languages. 150

16. **Website**: The following terms and conditions apply to electronic reserve and author websites:
Electronic reserve: If licensed material is to be posted to website, the web site is to be password-protected and made available only to bona fide students registered on a relevant course if:
This license was made in connection with a course,
This permission is granted for 1 year only. You may obtain a license for future website posting,
All content posted to the web site must maintain the copyright information line on the bottom of each image,
A hyper-text must be included to the Homepage of the journal from which you are licensing at http://www.sciencedirect.com/science/journal/xxxxx or the Elsevier homepage for books at http://www.elsevier.com , and
Central Storage: This license does not include permission for a scanned version of the material to be stored in a central repository such as that provided by Heron/XanEdu.

17. **Author website** for journals with the following additional clauses:

All content posted to the web site must maintain the copyright information line on the bottom of each image, and the permission granted is limited to the personal version of your paper. You are not allowed to download and post the published electronic version of your article (whether PDF or HTML, proof or final version), nor may you scan the printed edition to create an electronic version.
A hyper-text must be included to the Homepage of the journal from which you are licensing at http://www.sciencedirect.com/science/journal/xxxxx . As part of our normal production process, you will receive an e-mail notice when your article appears on Elsevier's online service ScienceDirect (www.sciencedirect.com). That e-mail will include the article's Digital Object Identifier (DOI). This number provides the electronic link to the published article and should be included in the posting of your personal version. We ask that you wait until you receive this e-mail and have the DOI to do any posting.

Central Storage: This license does not include permission for a scanned version of the material to be stored in a central repository such as that provided by Heron/XanEdu.

18. **Author website** for books with the following additional clauses:
Authors are permitted to place a brief summary of their work online only.
A hyper-text must be included to the Elsevier homepage at http://www.elsevier.com . All content posted to the web site must maintain the copyright information line on the bottom of each image.
You are not allowed to download and post the published electronic version of your chapter, nor may you scan the printed edition to create an electronic version.

Central Storage: This license does not include permission for a scanned version of the material to be stored in a central repository such as that provided by Heron/XanEdu.

19. **Website** (regular and for author): A hyper-text must be included to the Homepage of the journal from which you are licensing at http://www.sciencedirect.com/science/journal/xxxxx. or for books to the Elsevier homepage at http://www.elsevier.com

151

20. **Thesis/Dissertation**: If your license is for use in a thesis/dissertation your thesis may be submitted to your institution in either print or electronic form. Should your thesis be published commercially, please reapply for permission. These requirements include permission for the Library and Archives of Canada to supply single copies, on demand, of the complete thesis and include permission for UMI to supply single copies, on demand, of the complete thesis. Should your thesis be published commercially, please reapply for permission.

21. **Other Conditions**:

v1.6

If you would like to pay for this license now, please remit this license along with your payment made payable to "COPYRIGHT CLEARANCE CENTER" otherwise you will be invoiced within 48 hours of the license date. Payment should be in the form of a check or money order referencing your account number and this invoice number RLNK501139992. Once you receive your invoice for this order, you may pay your invoice by credit card. Please follow instructions provided at that time.

Make Payment To:
Copyright Clearance Center
Dept 001
P.O. Box 843006
Boston, MA 02284-3006

For suggestions or comments regarding this order, contact RightsLink Customer Support: customercare@copyright.com or +1-877-622-5543 (toll free in the US) or +1-978-646-2777.

Gratis licenses (referencing $0 in the Total field) are free. Please retain this printable license for your reference. No payment is required.